

A distributed and efficient population code of mixed selectivity neurons for flexible navigation decisions

Shinichiro Kira¹, Houman Safaai^{1,2}, Ari S. Morcos¹, Stefano Panzeri^{2,3}, Christopher D. Harvey^{1,*}

¹Department of Neurobiology, Harvard Medical School, Boston, MA, USA

²Neural Computation Laboratory, Istituto Italiano di Tecnologia, Rovereto, Italy

³Department of Excellence for Neural Information Processing, Center for Molecular Neurobiology (ZMNH), University Medical Center Hamburg-Eppendorf (UKE), Hamburg, Germany

*Correspondence: harvey@hms.harvard.edu

Abstract

Decision-making requires flexibility to rapidly switch sensorimotor associations depending on behavioral goals stored in memory. We identified cortical areas and neural activity patterns that mediate this flexibility during virtual-navigation, where mice switched navigation toward or away from a visual cue depending on its match to a remembered cue. An optogenetics screen identified V1, posterior parietal cortex (PPC), and retrosplenial cortex (RSC) as necessary for accurate decisions. Calcium imaging revealed neurons that can mediate rapid sensorimotor switching by encoding a conjunction of a current and remembered visual cue that predicted the mouse's navigational choice from trial-to-trial. Their activity formed efficient population codes before correct, but not incorrect, choices. These neurons were distributed across posterior cortex, even V1, but were densest in RSC and sparsest in PPC. We propose the flexibility of navigation decisions arises from neurons that mix visual and memory information within a visual-parietal-retrosplenial network, centered in RSC.

Introduction

As animals navigate for survival, they combine sensory information with internally stored behavioral goals to select a desirable route and rapidly switch routes as their behavioral goals change. Such navigation arises from a rich repertoire of sensorimotor associations that has expanded through evolution¹. In reflexive behaviors, a given sensory input always leads to a stereotyped action. Animals have acquired the ability to rapidly switch sensorimotor associations by responding to the same stimulus with distinct actions depending on their current behavioral goal. We refer to this ability as the flexibility of decision-making. In many laboratory decision-making paradigms, however, animals are trained to make one action in response to a given sensory cue and to make the opposite action in response to an alternate cue, which involves fixed sensorimotor associations but not flexible decisions. In contrast, in flexible decision-making, animals switch their associations between a given sensory cue and a desirable action from moment to moment, such as responding to the same sensory cue with one action at one moment and with the opposite action at the next moment as their behavioral goal changes. In general, this flexible action selection can be achieved

28 by combining external sensory information with internal information about one's behavioral goal, which
29 often manifests as short-term memory. A critical feature of this flexibility is its rapidity to switch actions
30 when behavioral goals or sensory cues change from one moment to the next. This rapidity sets flexible
31 decision-making apart from the learning or re-learning of different sensorimotor associations over longer
32 timescales. Together, these characteristics imply that specific neural mechanisms exist for rapid flexibility
33 over times as short as seconds, which are too brief for substantial neural circuit plasticity. Here, we aimed
34 to reveal the cortical areas and neural activity patterns that are central to flexible decisions during spatial
35 navigation by understanding how behavioral goals stored in short-term memory influence navigational
36 action selection in response to sensory cues.
37

38 The flexibility of decision-making has been investigated in experimental paradigms that do not involve
39 spatial navigation. Across studies using different tasks, diverse areas have been found to mix memory
40 and sensory information for flexible decisions, including higher sensory cortices, association cortices,
41 and premotor cortices²⁻¹¹. Other studies have assessed slow changes in sensorimotor associations over
42 many behavioral trials or sessions, which might rely on mechanisms distinct from those underlying rapid,
43 moment-to-moment flexibility¹²⁻¹⁵. Recently, several studies have identified cortical and subcortical areas
44 that have a causal role in flexible decisions^{3,4,11,14,15}. However, in many cases, a limitation has been that
45 studies have focused on one or two areas of interest without systematic screening across multiple areas to
46 compare their causal involvement and neural coding properties. Thus, these studies have not distinguished
47 whether flexible decisions involve different areas depending on the specific features of the task or are
48 mediated by a widely distributed network. Furthermore, it is unclear whether these areas are involved in
49 flexible decisions during navigation.
50

51 In contrast, many studies of navigation have focused on the encoding of current spatial variables,
52 such as location and heading in place cells, grid cells, and head direction cells¹⁶. Beyond well-established
53 spatial coding in hippocampus and entorhinal cortex, retrosplenial cortex (RSC) and posterior parietal
54 cortex (PPC) represent heading direction, running velocity, and navigational routes with world-centered
55 (allocentric) and self-centered (egocentric) reference frames¹⁷⁻³⁰. In addition, spatial signals have been
56 found even in primary and secondary visual cortices^{31,32}. Typically, however, these studies of navigation
57 have not investigated the mechanisms of decision-making in which animals must choose a navigational
58 path among alternatives.
59

60 Recent approaches have been developed to bridge navigation and decision-making. These approaches
61 have revealed that sequences of neural activity in PPC correlate with upcoming choices³³ and short-term
62 memories of previous cues, including during evidence accumulation³⁴⁻³⁷. Similar choice-related sequential
63 activity is also observed in RSC^{37,38}. These approaches have used behavioral tasks with a fixed sensorimotor
64 association needed for reward. For example, they employed a task in which cue A instructs turn left and
65 cue B instructs turn right^{33-35,38-40}. Thus, these studies have not investigated the flexibility of decision-making
66 during navigation in which animals switch sensorimotor associations depending on information stored in
67 short-term memory.
68

69 Therefore, it remains unclear which areas may be most critical for the flexibility of decision-making
70 during navigation. A leading candidate is PPC because of its established role in navigation decision
71 tasks^{33-35,41}. Another candidate is RSC due to its function in spatial memory and coding of navigation and
72 decision-related variables^{17,24,25,38,42-44}. Alternatively, flexible navigation decisions may arise from frontal
73 regions of cortex that have been shown to be necessary for flexibility in tasks not involving navigation^{3,14}. In
74 addition, at the level of neural computation, it is an open question how memory signals are incorporated
75 into the circuits important for navigation to mediate rapid switches in sensorimotor associations.
76

77 Here, we studied the flexibility of decision-making during navigation by designing a delayed
78 match-to-sample task in virtual reality and systematically screening the contributions of a wide range of
79 cortical areas using optogenetics and cellular-resolution calcium imaging. We demonstrate that neural
80 activity in posterior cortex is necessary for flexible navigation decisions, whereas frontal parts of cortex are
81 surprisingly less critical. We discovered neurons that mix short-term memory and visual information, and
82 these neurons were present in most parts of posterior cortex, even in V1. Surprisingly, RSC had the highest
83 density of these neurons, whereas these cells were sparsest in PPC, with a near absence in anterior PPC.
84 These neurons formed an efficient population code, which appeared to be critical for accurate decisions
85 because their activity was more informative when the mouse made correct decisions compared to errors.
86 Our results suggest a mechanism contributing to flexible navigation decisions based on mixed visual and
87 memory representations within a distributed visual-parietal-retrosplenial network, centered in RSC.
88

89 Results

90 A task that requires combining short-term memory and sensory information to make flexible navigation 91 decisions

92 We developed a delayed match-to-sample task for mice, based on navigation in a virtual reality T-maze
93 (Fig. 1a). A black (B) or white (W) sample cue was presented on the walls at the start of the T-stem, followed
94 by a delay segment in which the identity of the sample cue had to be stored in memory for a short period
95 (1.21 ± 0.65 s, mean \pm s.d., n = 17 mice). The delay segment duration was similar to or longer than delays
96 used in other delayed match-to-sample tasks, including for human and non-human primates^{5,6,8,45,46}. Next,
97 when the mouse reached a defined spatial position, a test cue appeared instantaneously in one of two
98 configurations: black walls on the left and white walls on the right (BW) or vice versa (WB). To receive a
99 reward, the mouse turned toward the T-arm with the wall color that matched the sample cue (Fig. 1b).
100 The two sample cues and two test cues defined four trial types (Fig. 1a-b, the example maze shows a B/
101 WB trial). Importantly, in the test segment, the mouse combined its memory of the sample cue with
102 the sensory information of the test cue to choose an appropriate action (left or right turn). This process
103 involves flexible navigation decisions in the sense that the mouse made different choices (left or right
104 turns) for the identical test cue depending on the short-term memory of the sample cue. This task is thus
105 different from tasks with fixed sensorimotor associations in which mice select the same behavioral action
106 for a given sensory cue. Furthermore, the flexibility in this task was rapid and required mice to combine
107 their short-term memory of the sample cue with the visual signals from the test cue differently from trial
108 to trial. The mice performed the task with high accuracy after 2–4 months of training ($90.5 \pm 5.5\%$ correct,
109 mean \pm s.d., n = 17 mice, Supplementary Fig. 1).

110

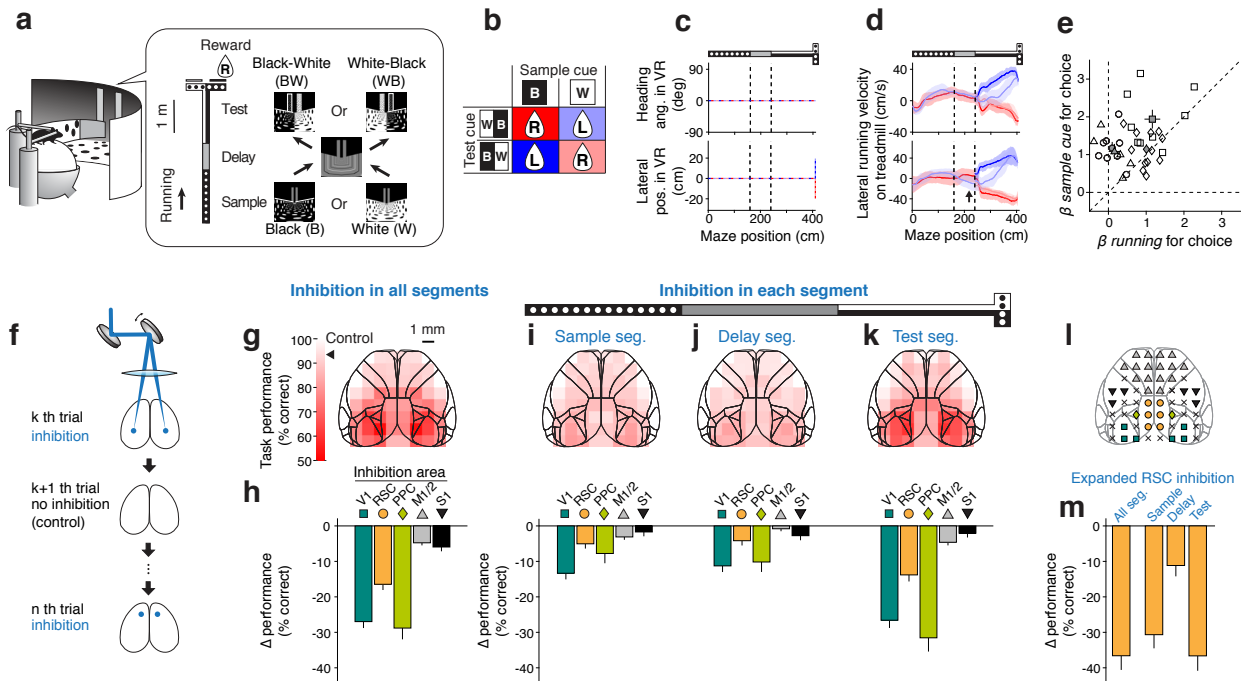


Fig. 1 | Optogenetics screen for cortical areas involved in a flexible navigation task

- (a) Schematic of experimental setup and delayed match-to-sample task.
- (b) Reward direction on each of the four trial types defined by a combination of the sample cue and test cue.
- (c) Heading angle (top) and lateral position (bottom) of a mouse in VR for four trial types shown as dashed lines and colored as in panel (b).
- (d) Lateral running velocity of a mouse on the treadmill in two example sessions for four trial types colored as in panel (b). Shading indicates mean \pm s.d. for correct trials. Prior to the test cue onset, trials with the black or white sample cue are colored by dark red and light blue, respectively. Arrow in the bottom panel indicates a position in the delay segment where the velocity differed between trials with the black and white sample cue.
- (e) Logistic regression to explain the mouse's choice based on the sample cue identity vs. running patterns. Beta coefficients from a single session are shown as an open symbol, with different shapes indicating sessions from different mice. Filled symbols with error bars indicate mean \pm s.e.m. for each mouse. $n = 35$ sessions from 4 mice. The data only include sessions in which calcium imaging data were acquired from posterior brain areas (V1, RSC, MM, A).
- (f) Schematic of optogenetic inhibition experiments. Bilateral light was delivered randomly to one of 28 pairs of target sites and interleaved with control trials (no laser).
- (g) Task performance (% correct) with inhibition throughout the trial for each cortical location (bilateral inhibition). The location of inhibition sites are overlaid on the cortical areal map based on the Allen Mouse CCF. The average performance in control trials ($93.5 \pm 2.8\%$, mean \pm s.d.) is indicated by an arrowhead on the color bar. $n = 212 \pm 10$ trials/site, 265 sessions, and 7 mice.
- (h) Change in task performance with inhibition in all segments (throughout the trial) relative to control trials. The change was computed from the data in panel (g) and averaged across sites in each brain area, as marked in panel (l). Error bars indicate mean \pm s.e.m. The performance significantly decreased with the inhibition in all areas ($p < 10^{-4}$; bootstrap, compared to zero). The effect of inhibition in V1, RSC, and PPC were larger than those for M1/M2 or S1 ($p < 10^{-4}$, bootstrap). The significance threshold was adjusted by Bonferroni correction with $\alpha = 0.05$ to account for 5 area-wise comparisons for panels (h-k) and 10 between-area comparisons.
- (i) Similar to panels (g-h), except with inhibition during the sample segment. $n = 141 \pm 8$ trials/site, 253 sessions, and 4 mice in panels (i-k). The performance significantly decreased with the inhibition in V1 ($p < 10^{-4}$), RSC ($p < 10^{-4}$), PPC ($p = 0.002$), M1/M2 ($p < 10^{-4}$), but not in S1 ($p = 0.16$) (bootstrap, compared to zero).
- (j) Similar to panels (g-h), except with inhibition during the delay segment. The performance significantly decreased with the inhibition in V1 ($p < 10^{-4}$), RSC ($p = 0.0009$), PPC ($p < 10^{-4}$), but not in M1/M2 ($p = 0.25$), and S1 ($p = 0.026$) (bootstrap, compared to zero).
- (k) Similar to panels (g-h), except with inhibition during the test segment. The performance significantly decreased with the inhibition in V1, RSC, PPC, and M1/M2 ($p < 10^{-4}$), but not in S1: $p = 0.083$ (bootstrap, compared to zero).
- (l) Colored symbols indicate grouping of inhibition sites based on cortical areas.
- (m) Similar to panels (h-k), except with expanded inhibition of RSC by six sites marked as orange circles in panel (l) in all or specific segments. The performance significantly decreased with the inhibition in all segments ($p < 10^{-4}$, $n = 154$ trials, 38 sessions, 4 mice), sample segment ($p < 10^{-4}$, $n = 148$ trials, 37 sessions, 3 mice), delay segment ($p < 10^{-4}$, $n = 153$ trials, 37 sessions, 3 mice), and test segment: ($p < 10^{-4}$, $n = 139$ trials, 35 sessions, 3 mice) (bootstrap, compared to zero).

112 Along the T-stem during trials with the same cues, the mouse observed the identical visual scene on
113 every trial. This was enforced by fixing the heading angle and lateral position of the mouse in the virtual
114 T-stem (Fig. 1c). Thus, the mouse only moved forward and backward in the virtual maze and followed
115 identical trajectories in the T-stem across trials. Specifically, throughout the T-stem of the maze, our virtual
116 reality software did not translate the mouse's lateral running velocity on the treadmill into movement in
117 the virtual maze, and only did so at the T-intersection and T-arms.
118

119 The running velocities of mice on the treadmill indicated their running patterns for right and left
120 choices diverged soon after the onset of the test cue (Supplementary Fig. 1i). Based on decoding of choice
121 direction from these running patterns, we estimated that the relevant decision-making process that
122 combined visual and memory signals to inform choices happened within the first one second of the test
123 segment (Supplementary Fig. 1i-j). Also, it appeared that the mouse used short-term memory to remember
124 the sample cue, instead of using only a behavioral mnemonic, for several reasons. First, the mouse was
125 unable to use heading angle and lateral position to remember the sample cue because these parameters
126 were fixed and identical across all trials during the delay segment, as mentioned above (Fig. 1c). Second,
127 although in some sessions mice had distinct running patterns on the treadmill for different sample cues
128 during the delay segment (arrow in Fig. 1d bottom), these running patterns were variable across trials, and
129 the mouse's choice on a trial was better explained by the presented sample cue than the running patterns
130 during the delay (Fig. 1e). Third, the running patterns in the delay segment did not strongly correlate with
131 task performance in individual mice, and sample cue-related running in the delay segment was absent
132 in some sessions with high performance (Supplementary Fig. 1k). Together, the running patterns suggest
133 that the mice made decisions at the beginning of the test segment using both short-term memory of the
134 sample cue and visual information of the test cue.
135

136 This task involves multiple neural processes, including for flexible decision-making, short-term
137 memory, and sensory perception, and each part of the task is critical for accurate behavioral performance.
138 We thus analyzed all parts of the task, but because our goal is to study flexible decision-making during
139 navigation, we focused mostly on the test segment in which decision-making occurred as mice combined
140 a memory of the sample cue with the sensory information of the test cue.
141

142 An optogenetics screen for cortical areas involved in a flexible navigation decision task

143 We screened for cortical locations with activity necessary for successful performance of the task. In
144 VGAT-ChR2 mice, blue laser light was delivered transcranially to activate inhibitory interneurons and silence
145 neighboring excitatory neurons (up to ~1 mm radius with 2-5 mW per site, Supplementary Fig. 2a-i)^{47,48}. On
146 a given trial, bilateral inhibition sites were chosen randomly from a grid of locations with 1 mm spacing.
147 Inhibition trials were interleaved with control trials (Fig. 1f). With inhibition in all segments throughout
148 a trial, the strongest impairment of task performance occurred when the inhibition site was chosen in
149 primary and secondary visual areas, PPC, and RSC (Fig. 1g-h). In contrast, the effects on task performance
150 were markedly smaller when the inhibition site was chosen in dorsal-anterior cortex, including motor and
151 premotor areas, and somatosensory areas (Fig. 1g-h). Statistics and p-values for these and subsequent
152 results are reported in the figure legends. Our inhibition results indicate that the posterior parts of cortex
153 are prominently involved in performing the task, compared to the anterior parts of the dorsal cortex.

154
155 To understand the aspects of the task that required each area's activity, we restricted inhibition to
156 either the sample segment, delay segment, or test segment on each trial. For V1, RSC, and PPC, the largest
157 effects on performance occurred with inhibition during the test segment (Fig. 1i-k, $p < 0.01$, bootstrap test).
158 In contrast, modest effects on performance occurred with inhibition of these areas during the sample and
159 delay segments. Because none of the silenced areas appeared especially critical during the delay segment,
160 the short-term memory might be maintained in a distributed cortical network, in uninhibited parts of the
161 brain, including ventral cortex or subcortical areas, or in a format other than neural spiking⁴⁹⁻⁵¹. Instead,
162 the prominent involvement of these areas in the test segment suggests they are candidates for combining
163 memory and visual signals to inform choice directions during flexible navigation decisions.
164

165 Because our approach inhibited only relatively small cortical volumes, the effects may have been
166 less pronounced in large areas, such as RSC^{52,53}. We therefore expanded our inhibition in RSC to three
167 bilateral pairs of inhibition sites (orange circles in Fig. 1l). This expanded inhibition decreased the mouse's
168 performance to near chance levels when RSC was inhibited throughout the trial ($55.8 \pm 4.0\%$ correct;
169 mean \pm s.e.m.) and resulted in a more substantial decrease in performance compared to the smaller
170 inhibition sites (Fig. 1m). While the expanded RSC inhibition had the largest effect in the test segment,
171 performance was also substantially decreased by inhibition in the sample segment, implying a possible
172 role of RSC in encoding the sample cue identity on each trial. These pronounced inhibition effects with the
173 expanded RSC inhibition suggest that RSC is essential for accurate performance in the flexible navigation
174 decision task.
175

176 The inhibition of cortical sites did not induce apparent motor deficits in mice. Compared to control
177 trials, the average running speed of mice varied only modestly across inhibition conditions ($3.1 \pm 11.0\%$
178 increase; mean \pm s.d.; Supplementary Fig. 2j-o). Therefore, the decrease in performance is unlikely the
179 result of running difficulty or memory loss due to a prolonged delay with reduced running speed. Together,
180 our results reveal that a visual-parietal-retrosplenial network is critical for the task and highlight V1, PPC,
181 and RSC as candidates for mixing memory and visual information for flexible decisions.
182

183 Neural activity represents essential task variables in a visual-parietal-retrosplenial network

184 To understand the functional roles of these areas in the task, we used two-photon calcium imaging
185 to monitor layer 2/3 neurons in V1, RSC (dysgranular region), and PPC (Fig. 2a). We divided PPC into a
186 medial region (area MM: mediomedial) and an anterior region (area A: anterior) because our previous
187 work and anatomical studies suggest divisions may exist in this part of posterior cortex⁵⁴⁻⁵⁷. Each imaged
188 area had activity throughout the full trial with transient peaks associated with the onset of the sample cue
189 and test cue, except for area A, which had a peak as the mouse turned into a T-arm (Fig. 2c). Individual
190 neurons in each area had transient activity, and different cells were active at different time points, forming
191 a sequence of activity that spanned the full trial (Fig. 2d). Many cells therefore contained activity selective
192 for particular maze positions, and thus at any time point, only a small fraction of the population was active.
193

194 To gain initial insights into how cells could contribute to flexible decision-making, we looked for neural
195 activity that nonlinearly combines the memory of the sample cue and the visual information of the test
196 cue. This nonlinear combination indicates the reward direction on a given trial and can be interpreted as
197 the logical exclusive OR (XOR) operation on the sample cue and test cue identities (Fig. 2b, top). The XOR
198 takes on two values: one for the trial types B/BW and W/WB for which the reward is on the left, and a
199 second value for the trial types B/WB and W/BW for which the reward is on the right. The reward direction
200 and mouse's choice were identical on correct trials and opposite on errors trials (Fig. 2b).

201
202 We performed an initial inspection of the activity in individual cells using deconvolved calcium
203 fluorescence timeseries and found cells that appeared to encode key task variables. Some cells were active
204 on the two trial types with the same sample cue (Fig. 2e), and others were active on the two trial types with
205 the same test cue (Fig. 2f), suggesting selectivity for the sample cue and test cue, respectively. However,
206 these cells did not directly represent the XOR of the two cues to inform the reward direction. Other cells
207 appeared to be choice selective with activity only when the mouse turned to a specific direction (left
208 or right) regardless of the trial type (Fig. 2g). Notably, the choice selective cells tended to appear in the
209 later part of the test segment (see the next section for analyses), whereas the mouse's choice-dependent
210 running appeared at the initial part of the test segment (Fig. 1d, Supplementary Fig. 1i), implying that
211 these cells did not causally guide the choices.

212
213 Surprisingly, we also found cells that were active mostly on only one of the four trial types defined by a
214 specific combination of a sample cue and a test cue. This type of activity is illustrated by an example neuron
215 in Figure 2h that was active mostly on B/WB trials. Neurons of this type have selectivity for the sample cue
216 (B vs. W trials), test cue (BW vs. WB trials), and reward direction (XOR; B/BW and W/WB trials vs. B/WB
217 and W/BW trials). Such activity is an effective way to encode many task variables in single neurons and
218 leads to separate representations of all four trial types across the population of cells. Importantly, these
219 cells became active for a single trial type in the initial part of the test segment, which was early enough
220 to influence upcoming choices. Interestingly, some single-trial-type selective cells responded differently
221 on correct and error trials. Some cells were less active on error trials (Fig. 2i), and others were active for
222 a different trial type on error trials (Fig. 2j), suggesting that the activity of these cells may be crucial for
223 making accurate choices. Cells with each type of selectivity were found in multiple cortical areas, as will
224 be shown in the next section.

225
226 We evaluated the selectivity of individual cells in a more systematic manner using a generalized linear
227 model (GLM)^{35,58}. The GLM included each task variable (sample cue, test cue, choice) and their interactions
228 (including interactions between sample cue and test cue to allow for XOR selectivity) as predictors of a
229 neuron's activity (Fig. 2k, Methods). Because cells tended to be transiently active, we modeled each predictor
230 as having selectivity conjunctive with maze position. Such position-specific selectivity is consistent with
231 cortical activity useful for navigation^{19,22,24,33}. In addition, because movements can substantially correlate
232 with neural activity in posterior cortex^{18,54,59,60}, the GLM also included predictors for the mouse's running
233 velocity, measured as rotations of the treadmill around three axes. We quantified the model's explanatory
234 power as the fraction of deviance explained (FDE), computed on test data left out from fitting (Fig. 2l-m,
235 Supplementary Fig. 3).

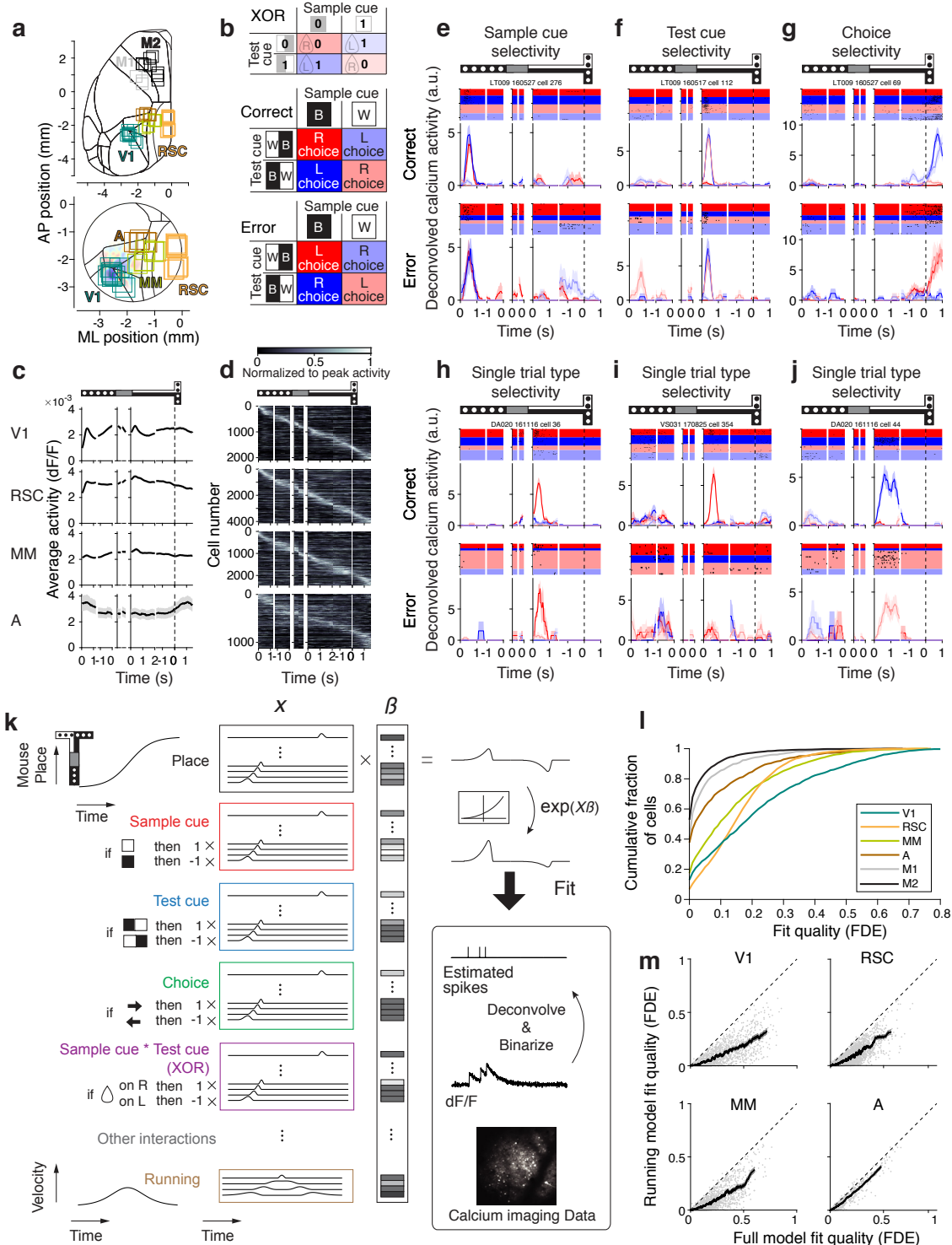


Fig. 2 | Calcium imaging and related analysis of neural activity

- Imaged cortical locations shown as individual fields-of-view. Bottom: same except superimposed on the field sign map for retinotopy. The circular outline shows the typical location of the cranial window.
- Reward direction on the four trial types determined by XOR combination of the sample cue and test cue (top). Choices follows XOR on correct trials (middle) or its opposite on error trials (bottom).
- Average activity across neurons, aligned to the start and end of the sample segment, start and end of the delay segment, start of the test segment, and T-intersection (vertical dashed line). V1: n = 2084 cells, RSC: n = 4103 cells, MM: n = 2439 cells, A: n = 1120 cells. Shading indicates mean \pm s.e.m.

- (d) Average activity normalized to its peak for each neuron (rows) sorted by time of peak average activity. The sequence of activity was cross-validated by plotting activity on even-numbered trials sorted by peak time on odd-numbered trials.
- (e) Example cell with sample cue selectivity in MM. Top row, correct trials; bottom row, error trials. Rasters of deconvolved and binarized calcium activity are shown for individual trials along with average activity (smoothed by running mean of 350 ms). Shading indicates mean \pm s.e.m. Colors are the same as in panel (b). For error trials, the average activity is not shown for some trial types if they had less than three error trials per trial type.
- (f) Similar to panel (e), an example cell in V1 with test cue selectivity.
- (g) Similar to panel (e), an example cell in MM with choice selectivity.
- (h) Similar to panel (e), an example cell in V1 with single-trial-type selectivity.
- (i) Similar to panel (e), an example cell in RSC with single-trial-type selectivity.
- (j) Similar to panel (e), an example cell in V1 with single-trial-type selectivity.
- (k) Schematic of the GLM fitted to the deconvolved and binarized calcium activity of each neuron. Predictors were divided into groups for task variables and movement. Task variables were basis expanded with position along the maze to reflect the sequential activity observed in panel (d). See Methods for full details.
- (l) GLM fit quality, measured as the fraction of deviance explained (FDE) on test data. Cells with converging fits for the full GLM were included. Mean \pm s.e.m. of FDE across cells in each area is V1: 0.212 ± 0.005 ($n = 1744$ cells; 84% of detected cells), RSC: 0.155 ± 0.002 ($n = 3865$ cells; 94%), MM: 0.139 ± 0.003 ($n = 2310$ cells; 95%), A: 0.081 ± 0.004 ($n = 1106$ cells; 99%), M1: 0.045 ± 0.003 ($n = 883$ cells; 100%), M2: 0.027 ± 0.001 ($n = 3243$ cells; 100%). The mean FDE was significantly different across areas ($p < 10^{-4}$).
- (m) Comparison of model fits for the full model (task and movement variables) and the movement-only model (no task variables). Dots indicate individual cells that had converging fits for both models. Black traces show the running mean across cells (window size, 50 cells). Shading indicates mean \pm s.e.m. V1: $n = 1744$ cells (84% of detected cells), RSC: $n = 3865$ cells (94%), MM: $n = 2310$ cells (95%), A: $n = 1081$ cells (97%).

236
237 Cells in V1 were best explained by the GLM across the imaged areas, followed by cells in RSC and MM
238 (Fig. 2l). The large majority of cells in these areas were better explained by the full GLM that included task
239 variables and running variables than by a reduced GLM that only included running variables (Fig. 2m).
240 The task variables thus contributed significantly to neural activity in V1, RSC, and MM. In contrast, most
241 cells in area A were well explained by the GLM with running variables alone, indicating that A had activity
242 predominantly related to the movements of the mouse. We also imaged cells in M1 and M2, even though
243 these areas did not appear to be strongly involved in task performance based on the optogenetics screen
244 (Fig. 1g-k). The GLM poorly predicted neural activity in M1 and M2 (Fig. 2l) although the mice showed
245 similar performance during imaging sessions for each area (Supplementary Fig. 4a-b), suggesting these
246 areas may be less informative for solving the task compared to posterior cortical areas.
247

248 We evaluated the information in each neuron about each task variable by using the GLM framework to
249 compute the likelihoods of neural activity conditioned on task and movement variables³⁵ (Methods). At each
250 time point in each trial, we estimated how likely one identity of a given variable was relative to the other
251 (e.g., black vs. white sample cue) by computing a log likelihood ratio (logLR), a well-established measure of
252 single-trial neural information^{61,62}. Although logLR is a signed value that indicates the preferred identity of
253 the variable, we adjusted the sign so that logLR was positive (or negative) for neural activity representing
254 the correct (or incorrect) identity of the task variable in a trial. The magnitude of logLR was larger for more
255 informative neural representations of the task variable. We used logLR to quantify information about task
256 variables in the subsequent analyses. Potential confounds concerning locomotion-related neural activity
257 were removed by using the GLM that included all task and movement variables in a single model and by
258 conditioning on the movement variables when computing information metrics, which together helped
259 isolate the neural coding for a task variable of interest.
260

261 **Widespread but distinct encoding distributions across cortical areas**

262 We first tried to identify an area critical for mixing sample cue and test cue information by looking at
263 major encoding patterns in individual cells. We therefore focused on the early part of the test segment
264 and analyzed the encoding of the sample cue, test cue, and the mixture of the two that indicates the
265 reward direction (XOR) for solving the task. At first, we used only correct trials to avoid analyzing complex
266 modulations between correct and error trials (e.g., Fig. 2i-j). We note that XOR information and choice
267 information are identical when considering only correct trials because the reward direction and the
268 mouse's choice perfectly match on correct trials.

269

270 In V1, the dominant information at any time point was related to the cue that was currently visible.
271 V1 had high sample cue information in the sample segment that decayed during the delay segment and
272 high test cue information in the test segment (Fig. 3a,d,e). Despite the predominance of information about
273 the current visual cue, V1 also contained substantial XOR information about the reward direction (Fig.
274 3b,c,f). To understand the mixing of sample cue information and test cue information in single cells in the
275 decision-making period (i.e., the beginning of the test segment; gray shading in Fig. 3a-c), for each cell, we
276 plotted its sample cue information in the test segment versus its test cue information in the test segment
277 (Fig. 3g). We used the polar angle as a measure for how much a cell encoded one cue relative to the other.
278 Cells residing close to 0° (horizontal-axis) or 90° (vertical-axis) corresponded to those encoding mostly
279 sample cue or test cue information, respectively. In contrast, cells located around the diagonal (45°) had
280 mixed representations of both cues. In the test segment, many V1 neurons had high information about
281 the test cue and much less information about the sample cue (Fig. 3g-i). V1 thus prominently represented
282 the current visual stimulus and had a skewed distribution of information that strongly favored the test cue
283 in the test segment.

284

285 The distribution of information in RSC was strikingly different. RSC had approximately equal levels
286 of sample cue and test cue information in the test segment, and thus its activity was less dominated
287 by the current visual cue (Fig. 3a,d,e). Importantly, RSC had significantly larger XOR information than V1
288 (Fig. 3b,c,f). This XOR information rose from the onset of the test segment and peaked as mice began to
289 report their choice in the form of a turn direction (Fig. 3b-c, Supplementary Fig. 1i-j). XOR information thus
290 appeared early enough to influence the decision-making process. The most striking feature of RSC activity
291 was the extent to which sample cue information and test cue information were mixed at the level of single
292 cells (Fig. 3g-h). Many cells had approximately equal sample cue information and test cue information in the
293 test segment (Fig. 3g-h). The distribution of information in RSC cells in the test segment was approximately
294 uniform between sample cue selective, mixed selective, and test cue selective cells, which was markedly
295 different from the distribution in V1 (Fig. 3i). As a result, RSC contained a larger fraction of cells that
296 equally mixed the memory information of the sample cue and visual information of the test cue than V1.
297 Interestingly, RSC's sample cue information was maintained by the sequential activation of cells during the
298 delay segment until it was mixed with the test cue information (Fig. 3a, Supplementary Fig. 4c-e). Together,
299 the results show that RSC has approximately equal mixing of information, the largest fraction of cells with
300 mixed information, and the highest XOR information, indicating that RSC could be a central area for mixing
301 memory information and visual information.

302

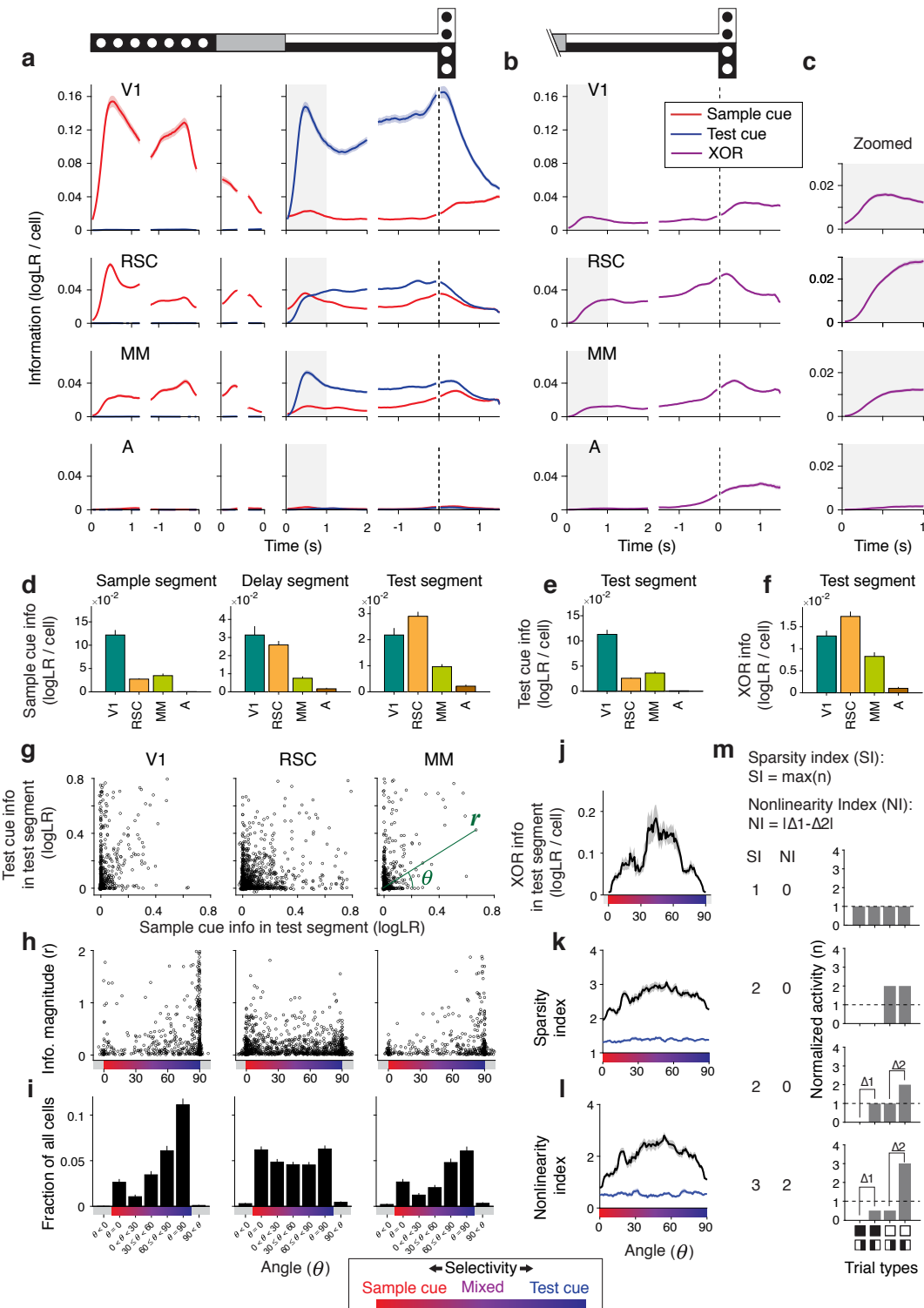


Fig. 3 | Task-related information and its mixing in posterior cortical areas.

- (a) Sample cue and test cue information quantified as $\log LR$ in individual cells, averaged across correct trials and then across cells with a converging fit for the full GLM. Shading indicates mean \pm s.e.m. Gray regions indicate the period (first one second) analyzed for the test segment in panels (d-l). V1: n = 1962 cells (94% of detected cells), RSC: n = 4052 cells (99%), MM: n = 2409 cells (99%), A: n = 1096 cells (98%).
- (b) Similar to panel (a), except for XOR information.
- (c) Zoomed view of XOR information from panel (b) for the first one second of the test segment.

- (d) Average sample cue information per cell in the sample, delay, and test segments. The information was averaged over the last 1 s for the sample segment, last 0.35 s for the delay segment, and first 1 s for the test segment. Error bars indicate mean \pm s.e.m. The information was significantly different between areas ($p < 10^{-4}$), except for between RSC and MM in the sample segment ($p = 0.11$) and between V1 and RSC in the delay ($p = 0.31$) and test segments ($p = 0.03$). All p values were calculated by bootstrap. The significance threshold was adjusted by Bonferroni correction with $\alpha = 0.05$ to account for 6 between-area comparisons for panels (d-f).
- (e) Similar to panel (d) except for test cue information in the test segment. The information was significantly different between areas ($p \leq 0.0080$).
- (f) Similar to panel (d) except for XOR information in the test segment. The information was significantly different between areas ($p \leq 0.0074$).
- (g) For each cell (circles), the sample cue information in the test segment and the test cue information in the test segment on correct trials.
- (h) Data from panel (g) replotted in polar coordinates as the magnitude (r) and angle (θ). Cells closer to 0 degrees have more sample cue information, and cells closer to 90 degrees have more test cue information. Skewness of the distribution (mean \pm s.e.m.); V1: -1.20 ± 0.10 , RSC: -0.06 ± 0.05 , MM: -0.67 ± 0.11 . Skewness was computed without cells with extreme angles (the highest and lowest 1% of cells) or noise-level information (magnitude $r < 0.01$). The distribution was significantly skewed for V1 and MM ($p < 10^{-4}$), but not for RSC ($p = 0.88$). The skewness was significantly different between V1, RSC, and MM ($p < 0.01$). All p values were calculated by bootstrap.
- (i) Distribution of cells from panel (h) in discrete angle bins. Bins for $\theta = 0^\circ$ and $\theta = 90^\circ$ included cells on the axes and those with chance-level deviation from the axes (Methods). Error bars indicate s.e.m. The fraction of cells with equal mixing ($30 \leq \theta < 60$) was significantly greater in RSC than in V1 or MM ($p < 10^{-4}$). The fractions of cells with noise-level information (magnitude $r < 0.01$) are not shown.
- (j) XOR information for cells across angles (running average, window of 50 cells). Cells from V1, RSC, and MM were combined because of their similarities (Supplementary Fig. 4f). Shading indicates mean \pm s.e.m. Cells with noise-level information (magnitude $r < 0.01$) were excluded. V1: $n = 510$ cells, RSC: $n = 1114$ cells, MM: $n = 423$ cells were included in panels (j-l).
- (k) Sparsity index for cells across angles (running average, window of 50 cells). See panel (m) for schematic of sparsity index. Cells from V1, RSC, and MM were combined because of their similarities (Supplementary Fig. 4g). Shading indicates mean \pm s.e.m. Blue lines show chance sparsity index value computed with shuffled trial identities.
- (l) Similar to panel (k), except for the nonlinearity index. Cells from V1, RSC, and MM were combined because of their similarities (Supplementary Fig. 4h).
- (m) Sparsity index and nonlinearity index in schematized activity distributions across the four trial types. The schematized examples range from non-selective (top) to single-trial-type selective (bottom). The activities across trial types were normalized to add up to 4. Sparsity index was defined as the max normalized activity (highest bar). Nonlinearity index was the activity difference between trial types with different test cues ($\Delta 1$ and $\Delta 2$) and followed by the absolute value of their difference ($|\Delta 1 - \Delta 2|$).

303 The information profile in MM was intermediate between V1 and RSC. MM also contained information
304 about the sample cue, test cue, and XOR (Fig. 3a-f), with a profile of information in the test segment biased
305 toward the test cue (Fig. 3i). This intermediate profile is consistent with MM residing at the interface of
306 two spatial encoding gradients centered at V1 and RSC⁵⁴. In contrast to the other areas, area A lacked
307 information about the sample cue and test cue throughout the trial and had XOR information only when
308 the mouse started turning at the T-intersection (Fig. 3a-f). The lack of prominent encoding of task variables
309 in area A was consistent with its activity being mostly explained by the locomotion of the mouse (Fig.
310 2m). When considering MM and A together, PPC surprisingly had the smallest fraction of cells with mixed
311 information, and thus, at least in its anterior portion, PPC may not be a key area for mixing memory and
312 visual information.

313
314 Notably, the cells with mixed sample cue information and test cue information contained XOR
315 information about the reward direction (Fig. 3j, Supplementary Fig. 4f). These mixed selectivity cells tended
316 to be the cells active preferentially on single trial types. We quantified this observation using a sparsity
317 index ranging from 1 (equal activity across all trial types) to 4 (activity exclusively on a single trial type)
318 and found that mixed selectivity cells had a sparsity index around 3 on average (Fig. 3k,m, Supplementary

319 Fig. 4g). Therefore, the cells with mixed representations tended to mix a specific combination of a sample
320 cue and a test cue, resulting in activity that was present mostly on single trial types. Furthermore, we
321 quantified the degree of nonlinearity in the neural responses mixing the sample cue and test cue using a
322 nonlinearity index (Fig. 3l-m, Supplementary Fig. 4h, Methods), ranging from 0 (linear mixing) to 4 (most
323 nonlinear mixing). Mixed selectivity cells showed nonlinear mixing as indicated by an average index above
324 2. This nonlinear mixing can be advantageous for linear decoding by a downstream area^{63,64}.

325
326 Surprisingly, we observed very few cells that encoded only the reward direction (or choice direction).
327 On correct trials, these cells would be active on two of the four trial types and have XOR information but
328 not sample cue or test cue information. When considering all the cells with appreciable XOR information
329 ($\log LR > 0.01$) in the early part of the test segment, approximately 90% of these cells also had sample cue
330 and/or test cue information (Supplementary Fig. 4i-j). Furthermore, of all the cells with XOR information,
331 roughly two-thirds contained sample cue information prior to the test cue onset (Supplementary Fig. 4k-l).
332 Therefore, the dominant carriers of XOR information for the reward direction were the cells that encoded
333 multiple task variables in the form of single-trial-type selectivity.
334

335 Together, these results reveal widespread representations in posterior cortex, with a bias toward
336 visual encoding in V1, locomotion-related activity in A, and mixing of memory and visual information in
337 RSC. Further, they indicate that multiple areas of posterior cortex, including V1 and most prominently
338 RSC, appear to be strong candidates for mixing memory with visual signals to guide choices. This mixing
339 manifested as single-trial-type selectivity, which appears to be an effective way to encode many relevant
340 task variables in single neurons.
341

342 **Mixed representations predict choices in RSC, MM, and V1**

343 If the mixed representations of sample cue information and test cue information are important for
344 task performance, then we expect the XOR information to influence the mouse's choice. We therefore
345 compared trials of the same trial type, except with the opposite choice (e.g., turning left vs. right on B/
346 BW trials). That is, we compared correct and error trials. For trials with identical sensory cues, if cells
347 have higher information about the reward direction (XOR) on correct trials than on error trials, then such
348 an observation would support the notion that the information in those cells was used to guide accurate
349 choices^{65,66}.
350

351 Strikingly, XOR information in RSC was markedly different between correct and error trials (Fig. 4b-c,
352 f-g). XOR information in RSC was 86% lower on error trials than on correct trials and was thus nearly absent
353 when mice made errors (Fig. 4f). Importantly, mice appeared engaged in error trials because error trials
354 were interspersed with correct trials and were completed by mice with similar timing compared to correct
355 trials (Supplementary Fig. 1a-f). These findings suggest that the absence of XOR information in RSC on a
356 given trial could have caused uncertainty and led to an inaccurate choice. A similar effect was also present
357 in MM and V1, suggesting that their XOR information could also be behaviorally relevant, but at a lesser
358 magnitude than in RSC (Fig. 4g). These results therefore suggest XOR information in RSC, MM, and V1 was
359 used to guide the mouse's choice.
360

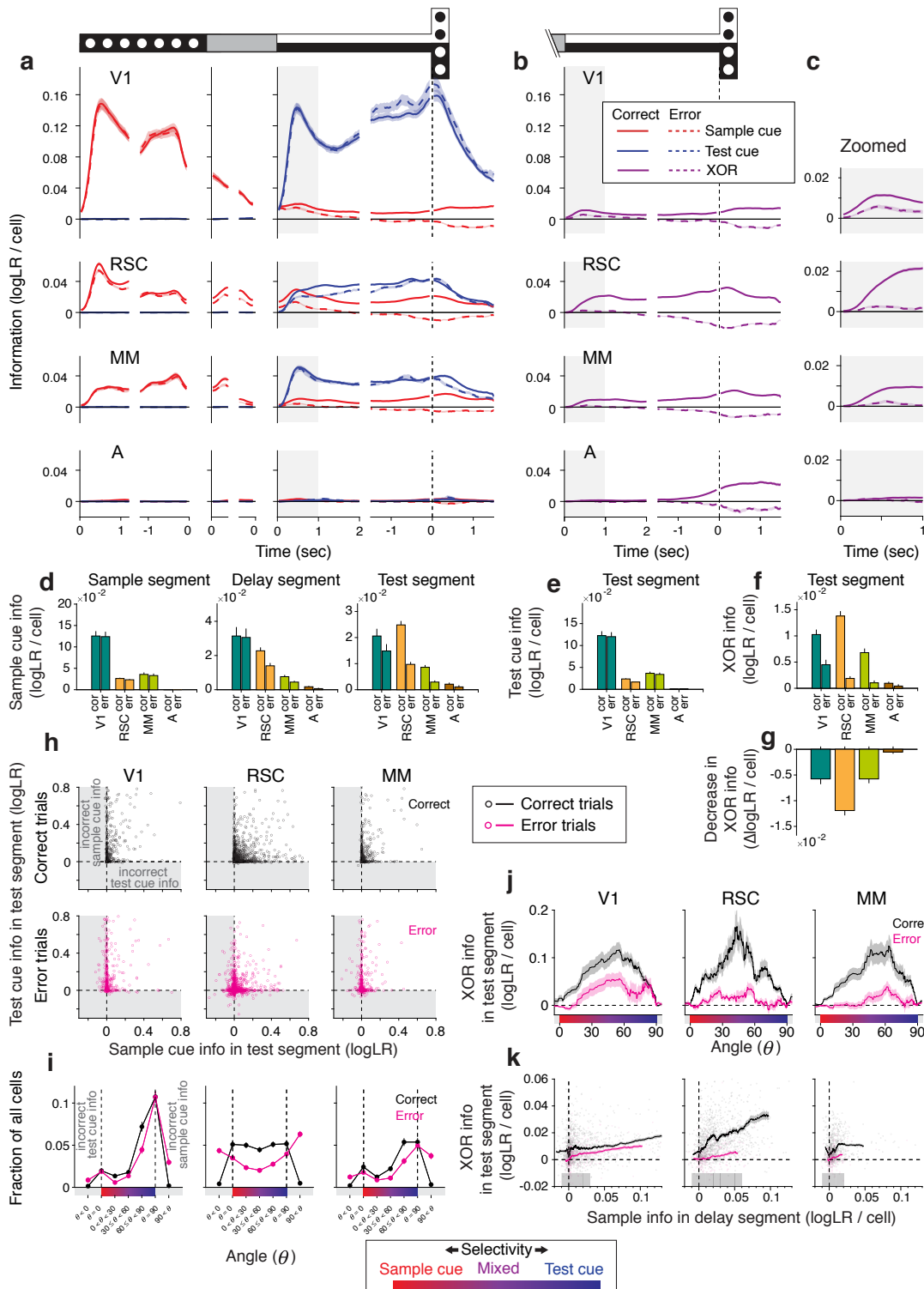


Fig. 4 | Comparing correct and error trials to identify activity patterns important for accurate decision-making

- (a) Sample cue and test cue information quantified as logLR in individual cells, averaged across trials and then across cells with converging fits for the full GLM for correct (solid) and error (dashed) trials. Shading indicates mean \pm s.e.m. Gray regions indicate the period (first one second) analyzed for the test segment in panels (d-k). V1: n = 1744 cells (84% of detected cells), RSC: n = 3865 cells (90%), MM: n = 2310 cells (95%), A: n = 1105 cells (99%).
- (b) Similar to panel (a), except for XOR information.
- (c) Zoomed view of XOR information from panel (b) for the first one second of the test segment.

- (d) Average sample cue information per cell in the sample, delay, and test segments for correct and error trials (specifically in the gray regions indicated in panels (b-c)). Error bars indicate mean \pm s.e.m. The difference between correct and error trials in the sample segment was significant in RSC ($p = 0.004$), but not for V1 ($p = 0.55$), MM ($p = 0.03$), and A ($p = 0.03$). The difference in the delay segment was significant for RSC and MM ($p < 10^{-4}$), but not for V1 ($p = 0.47$) and A ($p = 0.03$). The difference in the test segment was significant for V1, RSC, and MM ($p < 10^{-4}$), but not for A ($p = 0.04$). All p values were calculated by bootstrap for panels (d-g). The significance threshold was adjusted by Bonferroni correction with $\alpha = 0.05$ to account for 4 area-wise comparisons for panels (d-h), and 6 between-area comparisons for panel (g).
- (e) Similar to panel (d) except for test cue information in the test segment. The difference was significant in RSC ($p < 10^{-4}$), but not for V1 ($p = 0.50$), MM ($p = 0.10$), and A ($p = 0.08$).
- (f) Similar to panel (d) except for XOR information in the test segment. The difference was significant in V1, RSC, and MM ($p < 10^{-4}$), but not for A ($p = 0.08$).
- (g) Difference in XOR information between correct and error trials in the test segment, calculated per cell and averaged across cells. Error bars indicate mean \pm s.e.m. The decrease was significantly different from zero for V1, RSC, and MM ($p < 10^{-4}$), but not for A ($p = 0.08$). The amount of decrease was significantly different between areas ($p < 10^{-4}$), except for between V1 and MM ($p = 0.98$).
- (h) For each cell (circles), the sample cue information in the test segment and the test cue information in the test segment on correct trials (top/black) and error trials (bottom/magenta). Cells plotted in the top right quadrant correctly encoded the identity of the cues, and those plotted in other quadrants incorrectly encoded the identity of the sample cue, test cue, or both (gray shading).
- (i) Distribution of cells from panel (h) in discrete polar angle bins for correct (black) and error (magenta) trials. Bins for $\theta < 0^\circ$ and $90^\circ < \theta$ show the fraction of cells that incorrectly encoded the cue identity (gray shading). The fractions of cells with noise-level information (magnitude $r < 0.01$) are not shown. The fraction of cells was significantly different between correct and error trials in the following bins; V1: $\theta < 0^\circ$, $60^\circ \leq \theta < 90^\circ$, $90^\circ < \theta$; RSC: all bins except for $\theta = 90^\circ$; MM: $\theta < 0^\circ$, $30^\circ \leq \theta < 60^\circ$, $60^\circ \leq \theta < 90^\circ$, $90^\circ < \theta$ ($p < 0.002$). The significance threshold was adjusted by Bonferroni correction with $\alpha = 0.05$ to account for 7 bin-wise comparisons. Error bars indicate s.e.m and are smaller than the data marker for some bins.
- (j) XOR information for cells across angles (running average, window of 50 cells) for correct (black) and error (magenta) trials. The angle was defined on correct trials in panel (h). Shading indicates mean \pm s.e.m. Cells with noise-level information (magnitude $r < 0.01$) were excluded. V1: $n = 487 / 475$ cells, RSC: $n = 1055 / 1035$ cells, MM: $n = 418 / 409$ cells were included for the analysis of correct / error trials.
- (k) Comparison of XOR information on correct (black) and error (magenta) trials, controlling for the sample cue information immediately before making decisions (at the end of the delay segment). Dots indicate individual trials, with XOR information averaged across simultaneously imaged cells in that trial. The running mean (window of 100 trials) is shown with shading indicating mean \pm s.e.m. Gray bar at the bottom indicates bins of sample cue information for which XOR information was higher in correct trials ($p < 0.05$, bootstrap). The correct-error trial difference was significantly larger in RSC compared to V1 for 0.01-0.05 logLR (4 bins) of the sample cue information, and compared to MM for 0-0.02 logLR (2bins) of the sample cue information ($p < 0.05$, bootstrap). V1: $n = 1476$ correct / 307 error trials, RSC: $n = 1420$ correct / 265 error trials, MM: $n = 1009$ correct / 221 error trials.

361 Remarkably, the fraction of cells with mixed selectivity was markedly lower on error trials in RSC (Fig.
362 4h-i). Whereas correct trials had approximately equal numbers of sample cue, mixed, and test cue selective
363 cells, error trials had notably fewer mixed selectivity cells. These differences in the fraction of neurons with
364 mixed selectivity were most prominent in RSC and also present in MM and V1 (Fig. 4i). Relatedly, XOR
365 information in mixed selectivity cells in all areas was greatly reduced on error trials (Fig. 4j). Because mixed
366 selectivity cells were generally active on single trial types (Fig. 3k), the differences in XOR information
367 between correct and error trials were due in large part to encoding changes in single-trial-type selectivity
368 cells. As shown earlier in example cells, some single-trial-type selective cells were less active on error trials
369 (Fig. 2i) and thus had less XOR information when mice made incorrect choices (Fig. 5h, magenta points
370 near the origin). Other cells were active on different trial types on correct versus error trials (Fig. 2j) and
371 encoded the incorrect identity of the sample cue or test cue on error trials (Fig. 4h, magenta points in
372 gray shading) and thus incorrect (negative) XOR information (Fig. 4i, gray shading ranges). Together, these
373 observations support the idea that aberrant activity of mixed selectivity cells across a distributed set of
374 areas, and most strongly in RSC, contributes to incorrect choices.

375

376 The lower XOR information on error trials appeared to arise in multiple ways. One possibility is a failure
377 to receive sufficient sample cue information, such as due to fading memory during the delay segment.
378 Indeed, sample cue information was lower in RSC and MM in the delay segment on error trials (Fig. 4a,d).
379 Moreover, in the test segment, sample cue information was more reduced on error trials compared to test
380 cue information (Fig. 4d-e). Another possibility is a failure to mix sample cue and test cue information in
381 the test segment to generate XOR information despite the presence of sufficient sample cue information.
382 To test this possibility, on each trial, we computed the population-average information for the sample
383 cue immediately prior to information mixing (i.e., the end of the delay) and for XOR in the test segment
384 (Fig. 4k). For a given level of sample cue information, XOR information in RSC cells in the test segment
385 was much reduced on error trials (compare black and magenta along a vertical slice of Fig. 4k). This result
386 implies that mixing to produce XOR information was less effective on error trials. This difference was more
387 prominent in RSC than in V1 and MM (Fig. 4k). These results suggest that incorrect choices in this task
388 arose from the fading of memory signals as well as a failure to mix memory signals with current sensory
389 signals, particularly in RSC.

390
391 **Efficient reward direction encoding in populations of mixed selectivity cells**
392 Given the importance of mixed selectivity at the level of single cells, we further investigated if the
393 mixed selectivity cells play a privileged role at the level of populations of neurons. In many cases, it is
394 assumed that the downstream readout operates as a linear decoder. Given that the reward direction is
395 determined by the nonlinear XOR combination of the sample cue and test cue, a linear decoder cannot
396 read out the reward direction from a population of pure selectivity cells, which consists of cells with only
397 sample cue information and cells with only test cue information⁶³. In contrast, a linear decoder can read out
398 the reward direction from cells that contain XOR information, which in our case are the mixed selectivity
399 cells. Thus, the mixed selectivity cells appear particularly critical under common assumptions about linear
400 decoding mechanisms in the brain.

401
402 However, the brain possesses mechanisms that could enable nonlinear decoding^{67,68}. With a
403 nonlinear decoder, a downstream network could read out the XOR identity by combining cells with pure
404 selectivity, that is by nonlinearly combining cells with pure sample cue selectivity and cells with pure test
405 cue selectivity (Fig. 5a). With the assumption of a nonlinear readout mechanism, we assessed whether
406 populations of mixed selectivity cells were still more informative about the reward direction (XOR identity)
407 than populations of pure selectivity cells, by comparing simultaneously imaged populations from a given
408 imaging field-of-view (~0.5 mm² area). To evaluate the accuracy of the population code, we nonlinearly
409 decoded XOR identity from the population and quantified the mutual information between the true and
410 decoded XOR identity⁶⁹. In RSC, MM, and V1, the mixed selectivity population represented XOR identity
411 more accurately (higher mutual information) than the population of neighboring pure selectivity cells (Fig.
412 5b). Populations of neurons in area A contained little XOR information due to the lack of mixed selectivity
413 cells as well as pure selectivity cells for the sample and test cues (Fig. 5b-c).

414

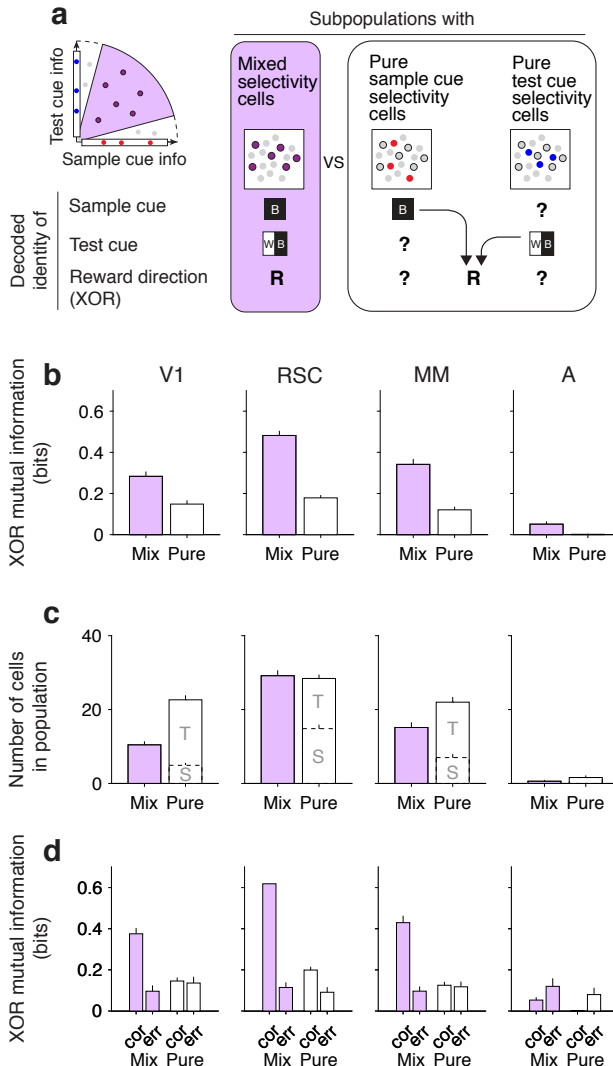


Fig. 5 | Population code for XOR in populations of mixed selectivity or pure selectivity cells

- (a) Mixed selectivity cells encode the identity of the sample cue, test cue, and reward direction (XOR) (purple rectangle). Neither pure sample cue selective cells nor pure test cue selective cells encode XOR by themselves, but XOR can be non-linearly decoded by combining the two types of pure selectivity cells (white rectangle).
- (b) Mutual information between the true and decoded XOR in populations of mixed selectivity cells ($15^\circ < \theta < 75^\circ$ in Fig. 4h, correct trials) and pure selectivity cells ($\theta = 0^\circ$ and $\theta = 90^\circ$ from Fig. 4i, correct trials). Error bars indicate mean \pm s.e.m. V1: n = 11 sessions (1783 trials), RSC: n = 12 sessions (1685 trials), MM: n = 7 sessions (1230 trials), A: n = 5 sessions (822 trials). Mutual information in mixed selectivity cells was significantly greater than that in pure selectivity cells in V1 ($p=0.0008$), RSC ($p < 10^{-4}$), MM ($p < 10^{-4}$), and A ($p = 0.046$). All p values were calculated by bootstrap and the significance threshold was not adjusted for multiple comparisons for panels (b-d).
- (c) Number of cells classified as mixed selective or pure selective (T = test cue selective; S = sample cue selective) per session. Error bars indicate mean \pm s.e.m. V1: n = 11 sessions, RSC: n = 12 sessions, MM: n = 7 sessions, A: n = 5 sessions. The number of cells was significantly larger for pure selective cells than for mixed selective cells in V1 ($p < 10^{-4}$) and MM ($p = 0.002$), but not in RSC ($p = 0.83$) and MM ($p = 0.09$).
- (d) Mutual information between the true and decoded XOR, computed separately on correct and error trials. Error bars indicate mean \pm s.e.m. V1: n = 1476 correct / 307 error trials, RSC: n = 1420 correct / 265 error trials, MM: n = 1009 correct / 221 error trials, A: n = 753 correct / 69 error trials. For mixed selectivity cells, the difference between correct and error was significantly different from zero in V1 ($p < 10^{-4}$), RSC ($p < 10^{-4}$), MM ($p < 10^{-4}$), and A ($p = 0.030$). For pure selectivity cells, the difference between correct and error was significantly different from zero in A ($p = 0.013$), but not in V1 ($p = 0.92$), RSC ($p = 0.12$), and MM ($p = 0.83$). The difference between correct and error in mixed selective cells was significantly larger than that for pure selective cells in V1, RSC, and MM ($p < 10^{-4}$) but not in A ($p = 0.88$). The difference between correct and error in mixed selective cells was significantly larger in RSC than in V1 ($p = 0.0001$) or MM ($p = 0.0063$).

415 We wanted to understand what contributes to the difference in the accuracy of the population code
416 between the mixed selectivity and pure selectivity populations. One possibility is that there is a significant
417 difference in the number of cells that fall into these groups. However, there were fewer, or at most equal,
418 mixed selectivity cells relative to pure selectivity cells (Fig. 5c), indicating efficient XOR encoding of the
419 mixed selectivity populations by containing more XOR information in a given number of cells. Second,
420 it is possible that correlations in the activity between neurons in the population differed, such as noise
421 correlations that create redundancy between neurons. However, in both the mixed selectivity and pure
422 selectivity populations, the magnitude of noise correlations was similar (Supplementary Fig. 6a-c). Also,
423 the difference in XOR information between these populations largely remained even after disrupting noise
424 correlations by shuffling trial labels independently for each neuron within a given trial type (Supplementary
425 Fig. 6d). Together, these results indicate that the higher accuracy in the mixed selectivity population was not
426 due to major differences in the population size or activity correlations, implying that the mixed selectivity
427 itself is the key feature for an efficient code, which represents the reward direction more accurately in a
428 smaller number of neurons.

429
430 We tested if this efficiency was a general property of mixed selectivity populations. Many properties
431 of a neural population can potentially contribute to a population code, including the number of cells,
432 noise correlations, and signal-to-noise ratio of encoding. Because it is difficult to control for and vary
433 these properties in real data, we simulated neural activity and compared the decoding accuracy from
434 either a mixed or pure selectivity population, while equalizing the properties between the two except for
435 their selectivity (Supplementary Fig. 7a). Interestingly, across all conditions, a mixed selectivity population
436 showed efficient XOR representation, in the sense that a mixed selectivity population encoded XOR more
437 accurately than the same size of a pure selectivity population, although it was less informative about either
438 the sample cue or the test cue (Supplementary Fig. 7b-e). Furthermore, a simulated mixed selectivity
439 population was also energetically efficient for encoding XOR in our task because it conveyed more XOR
440 information per spike compared to a pure selectivity population (Supplementary Fig. 7f-g). Together, mixed
441 selectivity appears to account for the higher efficiency of the population code.

442
443 This efficiency can be intuitively explained by the number of decisions required to decode XOR
444 (Supplementary Fig. 8a). In a pure selectivity population, both the sample cue and test cue need to be
445 encoded correctly in order for XOR to be decoded correctly from the population (Supplementary Fig.
446 8c). In contrast, XOR can be directly decoded from a mixed selectivity population, requiring only a single
447 variable to be encoded correctly (Supplementary Fig. 8b). Thus, a mixed selectivity population enables
448 more accurate decoding of XOR for a given condition even with a nonlinear decoding mechanism.

449
450 Finally, in imaged populations, XOR information was higher on correct trials than on error trials in
451 mixed selectivity populations, supporting the notion that when mixing is reduced, the mouse could not
452 make accurate choices (Fig. 5d). In contrast, the XOR information decoded from the populations of pure
453 selectivity cells showed smaller differences between correct and error trials. Thus, the mixed selectivity
454 populations may be used to guide the choice toward the reward direction, whereas the pure selectivity
455 populations appear to be less critical. Notably, all the properties of mixed selectivity populations were
456 present in RSC, V1, and MM (Fig. 5d), indicating that a distributed network of mixed selectivity cells could be

457 important for flexible decisions. However, whereas V1 and MM had a lower proportion of mixed selectivity
458 cells than pure selectivity cells, RSC had similar proportions of each type (Fig. 3i, Fig. 5b), resulting in the
459 largest number of mixed selectivity cells in RSC (Fig. 5c). This difference in proportions of cells, together
460 with the loss of XOR information in mixed selectivity cells on error trials (Fig. 4j), explains why RSC has the
461 largest change in XOR information between correct and error trials when averaged across individual cells
462 (Fig. 4f-g) or when quantified in its mixed selectivity population (Fig. 5d). For these analyses, similar results
463 were present for a fixed neural population size (Supplementary Fig. 5). Together, these results suggest that
464 a distributed network of mixed selectivity cells could be critical for flexible navigation decisions. These
465 cells were surprisingly sparse in anterior PPC (area A) and densest in RSC, endowing RSC with the highest
466 capacity to represent XOR information that could be read out to guide choices.
467
468

469 Discussion

470 Our work demonstrates a visual-parietal-retrosplenial network plays a central role in the flexibility
471 of decision-making during navigation. We first performed an optogenetics screen to find cortical areas
472 necessary for the task and then used calcium imaging in these areas to screen for the activity patterns
473 related to accurate decision-making. This relatively unbiased approach allowed us to discover three key
474 findings. First, activity in the visual-parietal-retrosplenial network was necessary for accurate performance
475 on the task, in particular during the test segment when the memory information must be combined with
476 the visual information to make a left-right decision. Second, within this network, we identified neurons
477 that nonlinearly mix short-term memory with visual information in the form of single-trial-type selectivity.
478 This mixed selectivity appeared useful for guiding navigation choices because it formed an efficient code
479 that accurately represented the reward direction (XOR) in a relatively small number of cells and could be
480 read out easily with a linear decoder. Third, these mixed selectivity cells had high XOR information when
481 the mouse made correct choices but low XOR information when the mouse made errors, suggesting that
482 their activity could be used to guide the mouse's choices. Together, these findings lead to the intriguing
483 proposal that the mixed selectivity cells have a causal link to the flexibility of navigation decisions.
484

485 The mixed selectivity cells for memory and visual information were distributed across many areas of
486 posterior cortex and had similar features across the areas. However, relative to other posterior cortical
487 areas, RSC showed an enrichment of these cells, the most equal mixing of memory and visual information,
488 the highest XOR information, and the largest differences in encoding of reward direction between correct
489 and error trials. The discovery of RSC's central involvement in flexible navigation decisions was surprising to
490 us because studies of decision-making have often highlighted the importance of other cortical areas, such
491 as frontal and parietal cortices^{3,33-35,47,62,70-75}. In contrast, RSC is widely viewed as important for encoding
492 current navigational variables^{23-25,27,29,30,76-78}. RSC can also represent a wide range of internal signals, including
493 spatial memory⁴²⁻⁴⁴, time^{79,80}, and value^{81,82}. Although recent studies have indicated a role for RSC for fixed
494 sensorimotor associations in decision-making tasks^{37,38,40}, our work extends further by showing how
495 memory and sensory signals in RSC can be combined to mediate flexibility of sensorimotor associations
496 during decision-making. We propose that a general function of RSC is to combine internal signals with
497 current sensory signals by forming a mixed representation that can flexibly guide navigation actions. Thus,
498 the mixed selectivity observed in our study could be a specific case of a more general function of RSC, and
499 our results highlight RSC as a candidate area to investigate flexibility of decision-making during navigation.

500
501 While we found an enrichment of mixed representations in RSC, further investigation will be required
502 to understand mechanisms that generate these representations. It is possible that RSC receives inputs that
503 separately contain visual and memory information, as is consistent with the dense axonal projections it
504 receives from visual cortices and the hippocampal formation⁸³⁻⁸⁶. Indeed, the hippocampus contains cells
505 that encode the identity of a landmark even behind the animal (i.e., landmark vector cells)⁸⁷. These cells
506 might maintain the short-term memory of the sample cue identity in our task and provide the memory
507 information to RSC. In this case, RSC neurons might play an active role in mixing these streams of information.
508 Alternatively, the mixed representations might arise through computations in a distributed network
509 spanning multiple areas, which is consistent with the presence of mixed selectivity neurons throughout
510 posterior cortex in our experiments. Future studies aimed at characterizing and manipulating the inputs to
511 RSC will help to clarify whether RSC plays a causal role in mixing memory and visual information.
512

513 An appreciable fraction of V1 neurons also showed similar mixed selectivity. In the population of V1
514 neurons, the current visual cue was more strongly encoded than the memory, which contrasted with the
515 RSC population that had equal mixing of the two. Although the delay length in our task was comparable to
516 the typical delay length used in delayed match tasks in monkeys^{5,6,8,45} and humans⁴⁶, some of the “memory”
517 in V1 (and possibly other areas) during the delay segment might have resulted from decaying visual signals
518 or short-term synaptic plasticity⁴⁹⁻⁵¹, which could result in nonlinear interactions of sequential visual
519 signals from the sample and test cues (e.g., visual adaptation). Regardless, the reward direction (XOR) was
520 encoded in V1 by mixed selectivity cells, which had similar properties to those in RSC. This finding adds to
521 a growing list of functions for V1 during navigation, including representing running velocity⁸⁸, head angular
522 velocity⁸⁹, spatial position³¹, and reward-related activity⁹⁰.
523

524 Surprisingly, PPC had the lowest density of mixed selectivity cells in the population. The activity in
525 area A was mostly related to the locomotion of the mouse. This locomotor-related activity is unlikely to
526 be essential for driving motor outputs because when we inhibited PPC, including A, in our optogenetics
527 experiments, the mouse completed trials without obvious motor deficits (Supplementary Fig. 2j-o).
528 Consistently, in previous work that inhibited cortical locations near A, the mouse was able to perform
529 simple locomotor tasks and only showed deficits in decision-making tasks^{33,39}. Area MM had an activity
530 profile intermediate between RSC and V1. Even when considering this part of PPC, the magnitude of XOR
531 information and the density of mixed selectivity cells were lower than in RSC. Much previous work has
532 connected PPC with decision-making during navigation. Our findings indicate that PPC’s role in navigation
533 decisions likely does not include the integration of memory and visual information. Instead, PPC may be
534 important for planning and guiding upcoming navigational actions with neighboring areas^{18,33}.
535

536 These differences across areas formed a gradient rather than sharp boundaries, consistent with a
537 representational principle that each area encodes all or most of the essential task variables but with
538 key distinctions in the magnitude of encoding of those variables in each area⁵⁴. Together, the neural
539 representation gradually shifted from mixed selectivity in RSC to locomotor selectivity in the anterior part
540 of PPC (area A). This spatial gradient appears to overlap with the spatial gradient going from allocentric
541 representations in RSC to egocentric representations in PPC²⁰. This overlap might reflect a relationship
542 between decision-making and navigation. Allocentric representations often rely on memory (e.g., past

543 landmarks) when the current sensory cues do not fully identify the animal's location. If we regard each trial
544 type as a different maze environment, the single-trial-type selectivity can be interpreted as an allocentric
545 representation to identify the mouse's location (maze environment) by using the current sensory cue (test
546 cue) and the memory of the past landmark (sample cue). By contrast, the locomotor-related activity can
547 be interpreted as an egocentric representation that encodes running with respect to the mouse's heading
548 direction. Therefore, along the spatial gradient from RSC to PPC, the conversion of the reference frames in
549 navigation might share the same mechanism that converts the mixture of memory and visual information
550 into locomotor selectivity during flexible navigation decisions.

551
552 Our findings highlight the importance of nonlinear mixed selectivity for flexible decision-making
553 during navigation. Our results support the theoretical idea that nonlinear mixed selectivity generates a
554 high dimensional neural representation, which increases the number of ways to flexibly associate inputs
555 to outputs by a linear decoder^{63,64}. Whereas some studies have found dense activity patterns across
556 conditions in individual neurons^{10,64,71}, we found mixed selectivity cells with sparse activity arising mostly
557 for a specific condition (trial type) defined by a combination of the sample cue and test cue. We were
558 surprised by the scarcity of mixed selectivity cells that represented only the reward direction, and by the
559 prominence of the mixed selectivity cells that instead encoded the reward direction along with other task
560 variables (i.e., the sample and test cue). This sparse form of mixed selectivity may be more interpretable
561 for the navigation system because it can represent a specific allocentric location (or maze environment).

562
563 Furthermore, we demonstrated that mixed selectivity cells efficiently formed a more accurate
564 representation of XOR than pure selectivity cells in real and simulated populations. In addition, the sparse
565 representation seems energetically efficient in the sense that it transmits more information per spike⁹¹.
566 While it is costly for the brain to maintain nonlinear mixed selectivity for numerous combinations of features
567 in the real world, it appears beneficial to create selective cells for familiar and important combinations of
568 features, such as the combinations of the sample cues and test cues that indicate the reward direction
569 in our experiments. Theoretically, in a population of pure selectivity cells, if the decoding accuracy for a
570 single stimulus feature is p , then the decoding accuracy for a combination of k independent features would
571 decay exponentially with the number of features as p^k . In contrast, decoding accuracy for mixed selectivity
572 cells would not suffer from such a decay. Thus, nonlinear mixed selectivity cells might have an advantage
573 to provide a compact and accurate representation for the recognition of complex stimuli, such as spatial
574 environments in our cases.

575
576 Although much work has highlighted the prevalence of mixed selectivity in the brain^{8,64,71,92,93}, its
577 importance has often been inferred from artificially created populations of non-simultaneously recorded
578 neurons. Instead, we demonstrated the importance of nonlinear mixing for accurate behavior in a
579 real, large-scale, simultaneously recorded population. Furthermore, we showed that mixed selectivity
580 is a distributed property across multiple parts of posterior cortex, including V1. The major differences
581 between correct and error trials in populations of mixed selectively cells, especially relative to other types
582 of selectivity, provide the suggestion that mixed selectivity has a causal role in flexible decisions. Now that
583 we have identified these putative decision-related signals, as experimental approaches become readily
584 available to manipulate the activity of specific cells based on their encoding properties⁹⁴⁻⁹⁹, it will be of
585 great interest to test directly the causal role of mixed selectivity cells for flexible navigation decisions.

586

587 **Data Availability**

588 Data are available upon request to the corresponding author.

589

590 **Code Availability**

591 Customized codes are available upon request to the corresponding author.

592

593 **Acknowledgments**

594 We thank members of the Harvey lab and Giuseppe Pica for helpful discussions and Leah Thomas,
595 David Allen, Vishal Sharoff, Theodore Lutkus, Joseph Deluisi, and Alec Nelson for assistance with behavioral
596 training of mice and experiments. This work was supported by grants from the NIH (R01 MH107620,
597 R01 NS089521, R01 NS108410, DP1 MH125776). SK was supported by an Alice and Joseph Brooks Fund
598 Fellowship, a Leonard and Isabelle Goldenson Postdoctoral Fellowship, an Uehara Foundation Research
599 Fellowship, a JSPS Overseas Research Fellowship, and a NARSAD Young Investigator Grant. SP received
600 support from the Fondation Bertarelli.

601

602 **Author Contributions**

603 SK and CDH conceived of the study. ASM and SK developed the behavioral task. SK performed all
604 experiments (optogenetics inhibition, two-photon calcium imaging, and electrophysiology). SK analyzed
605 the data with input from CDH, SP, and HS. SP contributed to the design of data analysis approaches. SK,
606 SP, and CDH interpreted the results. CDH supervised all aspects of the research. SK, SP, and CDH wrote the
607 paper with input from HS.

608

609 **Competing interests**

610 The authors declare no competing interests.

611

612 **Correspondence** and requests for materials should be addressed to CDH.

613 **Methods**

614

615 **Animals**

616

617 All experimental procedures were approved by the Harvard Medical School Institutional Animal Care and
618 Use Committee and were performed in compliance with the Guide for the Care and Use of Laboratory
619 Animals. Six male C57BL/6J mice (Jackson Laboratory, Stock No. 000664) were used for the calcium
620 imaging experiments, and twelve male VGAT-Chr2-EYFP mice (eleven mice from Jackson Laboratory,
621 Stock No. 014548; one mouse with VGAT-IRES-Cre/+; Ai32/+) were used for the optogenetics
622 experiments. Most of the mice were 8-16 weeks old at the start of behavioral training. Mice were housed
623 on a reverse 12 hour dark/light cycle and in pairs of littermates. Mouse health was evaluated daily.

624

625 **Surgical procedures**

626 *Calcium imaging surgery*

627

628 For calcium imaging experiments, prior to behavioral training, mice were implanted with a titanium
629 implant that was designed for imaging procedures. The headplate had an opening in the middle that
630 allowed subsequent placement of a cranial imaging window. The location of the headplate opening was
631 centered at 2.0 mm lateral and 2.5 mm posterior relative to bregma to allow imaging in V1, RSC, and PPC
632 and was centered at 1.2 mm lateral and 1.2 mm anterior relative to bregma for imaging in M1 and M2.
633 The headplate was affixed to the skull by dental cement (Radiopaque Metabond, Parkell) mixed with India
634 ink (5% vol/vol) to increase light shielding for imaging. To allow for an imaging plane parallel to the surface
635 of cortex, the headplate was tilted by 15° in roll relative to the mouse's body axis. In the initial surgery
636 prior to behavioral training, the planned center coordinates for the cranial window were marked by a drill
637 and ink on the skull and covered by transparent dental acrylic (Ortho-Jet, Lang Dental), so that the
638 coordinates could be recovered in a subsequent cranial window surgery.

639

640 A cranial window surgery was performed when the mouse had achieved high performance on the delayed
641 match-to-sample task (greater than 80% correct). The cranial window was made centered at the
642 coordinates marked during the initial implantation of the headplate (2.0 mm lateral and 2.5 mm posterior
643 to bregma for posterior imaging; 1.2 mm lateral and 1.2 mm anterior to bregma for anterior imaging). A
644 window for posterior imaging was constructed by bonding two 3.5 or 4.0 mm-diameter coverslips to each
645 other and to an outer 4.0 or 5.0-mm diameter coverslip (#1 thickness, Warner Instruments). A window for
646 anterior imaging was constructed by bonding two laser-cut 2.0 x 2.5 mm oval coverslips to each other and
647 to an outer 3.0 mm diameter coverslip (#1 thickness, Warner Instruments). Coverslips were bonded to
648 each other by UV-curable optical adhesive (Norland Optics NOA 65 or 68).

649

650 AAV2/1-synapsin-GCaMP6s-WPRE-SV40 virus (University of Pennsylvania Vector Core Facility, Catalog No.
651 AV-1-PV2824) was diluted to ~0.5–1.0 × 10¹³ gc/mL in phosphate-buffered saline. Injections were made
652 using a glass pipette and custom air-pressure injection system. At each site, ~50–70 nL was injected 250–
653 300 μm and 450–500 μm below the dura over 1–2 minutes. After each injection, the pipette was left in
place for an additional 1–2 minutes. For the posterior cranial window, a glass pipette was inserted at a 30°
angle relative to the brain surface, and virus was injected at three sites in V1 (2.2 mm lateral, 3.5 mm

654 posterior; 2.8 mm lateral, 3.5 mm posterior; 2.8 mm lateral, 3.0 mm posterior to bregma), two sites in
655 RSC (0.5 mm lateral, 2.15 mm posterior; 0.5 mm lateral, 2.85 mm posterior to bregma), and three sites
656 for PPC (1.2 mm lateral, 1.75 mm posterior; 1.8 mm lateral, 2.0 mm posterior; 2.5 mm lateral, 2.25 mm
657 posterior to bregma). For the anterior cranial window, a glass pipette was inserted perpendicular to the
658 brain surface, and virus was injected at ten sites across M1/M2 areas (nine sites in a 3 x 3 grid pattern
659 centered at 1.2 mm lateral, 1.2 mm anterior to bregma with 500 µm spacing, and one site near ALM at
660 1.2 mm lateral, 2.2 mm anterior to bregma). When the planned coordinates overlapped with blood
661 vessels, injections were shifted by 50-100 µm to avoid rupturing the vessels.

662
663 The window was sealed using dental cement (Radiopaque Metabond, Parkell) mixed with India ink (5%
664 vol/vol). To prevent light contamination and create a water bath for imaging, an aluminum ring was affixed
665 to the top of the headplate with dental cement mixed with India ink. Experiments started after ~2 weeks
666 from viral injection and typically continued for 6–8 weeks. Experiments were terminated when GCaMP6s
667 expression appeared high, with some neurons exhibiting GCaMP6s in the nucleus.

668
669 *Optogenetics surgery*
670 For optogenetics experiments, mice were implanted with a clear skull cap, following procedures described
671 previously^{47,54}. The cranial surface was exposed, and the headplate was affixed to the interparietal bone
672 (behind the lambda suture) by transparent dental cement (Clear Metabond, Parkell). The remaining
673 cranial surface was covered by a thin layer of cyanoacrylate (Insta-Cure, Bob Smith Industries) and
674 reinforced by ~1 mm layer of transparent dental acrylic (Ortho-Jet, Lang Dental) on top. After a mouse
675 was trained, the acrylic surface was polished with a polishing drill (Model 6100, Vogue Professional) using
676 denture polishing bits (HP0412, AZDENT) and coated by a thin layer of clear nail polish (Electron
677 Microscopy Sciences, 72180). For light shielding, an aluminum ring was affixed to the top of the headplate
678 by dental cement mixed with India ink or carbon (Sigma-Aldrich). Fiducial marks were made on the
679 aluminum ring to aid laser alignment.

680
681 **Behavior**
682 *Virtual reality system*
683 The virtual reality system was built based on previous designs^{33,34}. Virtual reality environments were
684 constructed and operated using MATLAB-based ViRMEn software (Virtual Reality Mouse Engine)¹⁰⁰. A
685 projector (PicoPro / PicoBit, Celluon Inc., Laser Beam Pro, KDC) was used to display the virtual
686 environment onto the back side of a 24-inch diameter half-cylindrical screen. The virtual environment was
687 updated in response to the mouse's locomotion on an open cell Styrofoam spherical treadmill (8-inch
688 diameter, ~135 g). Two optical sensors (ADNS-9800, Avago Technologies) positioned 45° below the
689 equator of the ball and separated by 90° in azimuth were connected to a Teensy-3.2 microcontroller
690 (PJRC.COM) to measure the 3-dimensional rotation velocity of the ball (roll, pitch, and yaw).

691
692 *Delayed match-to-sample task*
693 Mice performed the navigation-based delayed match-to-sample task in a virtual reality T-maze (Fig. 1a,
694 Supplementary Fig. 9d). The mouse traversed three segments: sample, delay, and test in the T-maze. In

695 each segment, the mouse spent a variable duration from trial to trial depending on the maze traversal
696 speed. In the sample segment, either black (B) or white (W) patterns on the wall provided the sample cue.
697 In the delay segment, the walls had a gray pattern in all trials. The test segment provided the test cue,
698 either white patterns on the left side and black patterns on the right side (WB) or vice versa (BW). The
699 test cue was not revealed (and not visible) until the mouse reached a defined spatial position (240 cm
700 away from the maze start). At the T-intersection, the mouse was required to make a right or left choice
701 by turning to the T-arms whose color matched the sample cue. When the mouse ran 20 cm into the T-
702 arm, the trial ended. The correct choice was rewarded by 4-5 µL of 10x diluted sweetened condensed milk
703 (Eagle Brand) or 30 mM acesulfame solution (Prescribed For Life). Incorrect choices were not rewarded,
704 and consecutive error trials were penalized by prolonged inter-trial intervals. After the intertrial interval
705 (at least 4 s), the next trial started with the mouse location reset to the beginning of the maze. The sample
706 and test cues were randomly selected on each trial and were thus independent of one another.

707
708 The length of the T-stem was 400 cm, of which the last 160 cm was allocated to the test segment. The
709 delay segment ranged from 20 to 100 cm in length and varied based on the behavioral performance (see
710 below). The remaining maze length was allocated to the sample segment (140 to 220 cm).

711
712 In order to control the visual scene, movement in the virtual environment was constrained. The mouse's
713 heading angle was fixed straight throughout a trial. In the T-stem, only forward/backward movements
714 were allowed in the T-stem, and lateral movements were not allowed; the pitch velocity of the spherical
715 treadmill was translated into forward/backward movement, and the roll and yaw velocities did not affect
716 movement in the virtual environment. Backward movement was not observed in any mice. In the T-arms,
717 only lateral movements were allowed; the roll velocity was translated into lateral movements, and the
718 pitch and yaw velocities did not affect the movement.

719
720 The black and white walls for the sample cue and test cue had dot patterns (white dots on a black wall
721 and black dots on a white wall). The gray wall for the delay segment had a striated pattern to create optic
722 flow.

723
724 *Behavioral training*
725 Starting five days before the first training session, mice were put on a water restriction schedule that
726 limited their total consumption to 1 mL per day. The weight of each mouse was monitored daily and
727 additional water was given if the mouse's weight fell below 80% of the pre-training weight. Mice were
728 trained daily for 45-60 minutes at approximately the same time each day. Mice learned the task through
729 the following four phases of training (Supplementary Fig. 9). Approximately 25-50% of mice learned to
730 perform the delayed match-to-sample task with high accuracy (greater than 80% correct). To increase the
731 statistical power for the analyses of error trials, we included more sessions with moderate accuracy
732 (~80%) to analyze the imaging experiments, compared to the optogenetic experiments.

733

734 *Phase 1: Linear track*

735 For the first phase, mice were trained to run straight on the spherical treadmill in a linear track. Mice
736 received a reward when they reached a gray tower presented at the end of the linear track. Pitch and roll
737 velocity were translated to the forward speed and rotation of heading angle, respectively. The heading
738 angle was not fixed at this stage, so that mice were required to correct their running trajectory to a straight
739 path; this appeared to help produce good control of the spherical treadmill. For initial trials, the track
740 length was short to increase the frequency of reinforcement. The track length was gradually extended if
741 mice reached a tower within 30 s. Typically, mice learned to run along a ~300 cm track within 3-5 days of
742 training.

743

744 *Phase 2: Single tower T-maze*

745 For the second phase, mice were trained to make visually guided turns to the right or left in a T-maze. The
746 length of the T-stem was set to 200 cm, and a single gray tower was presented either behind the right or
747 left T-arm throughout the trial. Mice received a reward when they reached the gray tower by turning
748 towards the tower at the T-intersection. To facilitate training for the following phases, the T-stem had
749 either a black or white wall pattern (later used as the sample cue) whereas T-arms had the black pattern
750 on one arm and white pattern on the other (later used as the test cue). The gray tower was located behind
751 the arm that matched the color to the initial cue. While mice could make turns based only on the gray
752 tower, the wall patterns acclimated mice for the next phase of training.

753

754 *Phase 3: Two tower T-maze*

755 For the third phase, mice learned associations between a combination of wall patterns and turning
756 directions (choices). The maze structure was the same as in the second phase, except now we interleaved
757 trials with a single tower (identical to Phase 2 trials) with trials with two towers, in which a tower was
758 located behind both T-arms. For two tower trials, mice were no longer able to rely on the tower location
759 to decide the turning direction and instead were required to use the wall patterns to make choices
760 following the delayed match-to-sample rule. The fraction of two-tower trials was dynamically adjusted
761 based on the performance criteria described below; the fraction was increased or decreased with a step
762 of 10%. When the fraction of two-tower trials reached 100% and the behavioral performance was
763 consistently above 90% accuracy, the mice were advanced to the final phase of training.

764

765 *Phase 4: Delayed match-to-sample task with variable delay*

766 For the final phase, mice learned to make a choice in a longer maze (400 cm) based on the combination
767 of the sample and test cues, except now with a delay segment added. With a delay segment, the sample
768 cue disappeared at the onset of the delay, and the test cue appeared instantaneously at the offset of the
769 delay. The test cue was not visible by looking down the T-stem; rather, we made the test cue appear at
770 an exact spatial location (240 cm away from the maze start). This was the first training phase with a delay
771 segment. We gradually lengthened the delay segment as the mouse's performance improved. We
772 lengthened the delay segment while simultaneously shortening the sample segment, thus keeping the
773 overall maze length constant. For our analyses, we included trials with a delay length of at least 20 cm.

774

775 Because this task was challenging for the mouse, we found it was helpful to include “crutch trials” that
776 were easy for the mouse. In randomly selected 10% of trials, we omitted the delay segment
777 (Supplementary Fig. 9e). These trials had a maze structure similar to the two tower T-maze in Phase 3.
778 Crutch trials were not analyzed in the imaging and optogenetics experiments.

779
780 *Adjustment of task difficulty*
781 The task difficulty was adjusted by the length of the delay segment (Phase 4) or the fraction of two-tower
782 trials (Phase 3). We adjusted the difficulty level based on the behavioral performance, statistically
783 evaluated by a sequential probability ratio test^{101,102}. When the test decided that the mouse’s
784 performance was at the chance level (50%), task difficulty was decreased, whereas when the test decided
785 that the mouse’s performance was greater than 80% correct, task difficulty was increased. We set the
786 highest and lowest levels of difficulty, so the level was adjusted within a set range. Performance was
787 evaluated using all trials from the last statistical decision up to a current trial in a session. For well-trained
788 mice, the task difficulty typically remained stationary throughout a session after initial increases at the
789 start of the session.

790
791 **Optogenetics experiments**
792 The photoinhibition system was built based on a previous design⁵⁴. A 470 nm laser (LRD-0470-PFR-00200,
793 Laserglow Technologies) was passed through galvanometric scan mirrors (6210H, Cambridge Technology)
794 and focused using an achromatic doublet lens ($f = 300$ or 400 mm, AC508-300-A-ML, AC508-400-A-ML,
795 Thorlabs). The laser (analog power modulation, off to 95% power rise time, 50 ms) and mirrors (< 5 ms
796 step time for steps up to 20 mm) allowed simultaneous inhibition of bilateral sites by rapidly alternating
797 the inhibition sites by moving the mirrors while the laser was turned off. The focused laser had a top-hat
798 profile with a diameter of approximately 200 μm .

799
800 In each hemisphere of VGAT-ChR2 mice, 28 inhibition target sites were arranged in a grid with 1 mm
801 spacing, covering from 0.5 to 3.5 mm in the medial-lateral direction and from -4 mm to +3 mm in the
802 anterior-posterior direction with respect to bregma (Fig. 1l). For three mice, inhibition was always applied
803 throughout a whole trial, and for four mice, inhibition was applied throughout a whole trial or during a
804 specific trial segment (sample, delay, or test segment). In a separate four mice, including one VGAT-IRES-
805 Cre/+; Ai32/+ mouse, inhibition was expanded to three bilateral pairs of sites in RSC (centered at -3.5, -
806 2.5, -1.5 AP; 0.5 ML) in all segments or in a specific trial segment (sample, delay, or test segment).

807
808 The inhibition was applied in randomly selected and interleaved 10–40% of trials. The fraction of inhibition
809 trials was adjusted to maintain behavioral performance above ~80% correct across all trials. In each
810 inhibition trial, the combination of bilateral inhibition sites and the inhibition segment were selected
811 randomly without replacement. When all combinations were selected, the process was reinitialized and
812 repeated.

813
814 The laser power at each inhibition site had a near-sinusoidal temporal profile at 40 Hz and time-averaged
815 power of 2–5 mW. For the expanded inhibition in RSC, the total laser power across the three sites on each

816 hemisphere was ~5–10 mW for three mice and ~5 mW for one VGAT-IRES-Cre/+; Ai32/+ mouse. To ensure
817 inhibition prior to the mouse seeing the sample cue, the laser was turned on 1 s before the trial onset for
818 the inhibition throughout the whole trial and for the sample segment inhibition. For a similar reason for
819 the test cue, the light was turned on 20 cm before the test segment for the test segment inhibition. The
820 light was turned off at the trial end (i.e., onset of the inter-trial interval).

821
822 **Electrophysiology**
823 To measure the spatial extent of optogenetic inhibition across cortical areas, extracellular recordings were
824 conducted in one VGAT-ChR2-YFP mouse (Supplementary Fig. 2). A small craniotomy (diameter of ~1 mm)
825 was created on the left side of the region of interest in the left hemisphere one day before the recording
826 sessions. A 32-channel silicon probe (A1x32-Poly2-5mm-50s-177, NeuroNexus) was angled at 55-60° from
827 the cortical surface at the entry point to avoid blocking the laser oriented perpendicularly to the cranial
828 surface. The tip of the probe was advanced down to 1 mm below the dura for PPC and RSC recordings,
829 and to 1.7 mm below the dura for M2/ACC recordings, based on manipulator readings. The signals were
830 recorded at 20 kHz by the Intan RHD2000 Evaluation System, and highpass-filtered at 250 Hz offline. Multi-
831 unit activity was measured offline by counting the number of spikes that crossed a threshold, which was
832 adjusted to include most of the local spikes in the absence of optogenetic inhibition.

833
834 The number of spikes were counted across recording sites during the first 5 s of a laser-on period, and
835 then normalized to the spike counts during 5 s of a laser-off period immediately before the laser onset.
836 Trials with less than 5 spike counts in the laser-off period were excluded. Recordings between 600 and
837 700 µm below the cortical surface were used for the evaluation of effects as a function of the horizontal
838 distance from the laser center (Supplementary Fig. 2d-f). Recordings within 500 µm from the laser center
839 were used for the evaluation across the cortical depth (Supplementary Fig. 2g-i).

840
841 **Widefield retinotopic mapping**
842 To locate the imaged areas with respect to visual areas, a retinotopic map was obtained from two of four
843 mice that were used for imaging of posterior cortical areas (V1, RSC, MM, and A). The details of the
844 procedure were described previously⁴¹.

845
846 Widefield images were collected by a custom-built epifluorescence macroscope¹⁰³. Excitation light was
847 provided by a blue LED (455 nm LED, Thorlabs; band-pass filtered at 469 nm with 35nm bandwidth,
848 Thorlabs), focused on and reflected by a small mirror (8 mm Diameter 45° Rod Mirror, Edmund Optics).
849 The reflected diverging light passed through a camera lens (NIKKOR AI-S FX 50mmf/1.2, Nikon) and
850 illuminated the cortical surface. Emission light was collimated through the same camera lens, band-pass
851 filtered (525 nm with 39 nm bandwidth, Thorlabs), and imaged by a second lens (SY85MAE-N 85 mm F1.4,
852 Samyang) onto a CMOS camera (ace acA1920-155um, Basler).

853
854 Mice with expression of GCaMP6s were lightly anesthetized by isoflurane on a platform with their head
855 angled at 30° with respect to a computer display (MG279Q, Asus), so that their right eye was positioned
856 in front of the display. The visual stimulus was designed based on a previous study¹⁰⁴. A spherically

857 corrected black and white checkered moving bar (5 or 7 deg in width) swept vertically and horizontally in
858 four directions across the display with the speed of 7 deg/s. Each sweep direction was repeated six times
859 during a block, and four or six blocks were presented in a session. Images were collected at 60 Hz,
860 synchronized with the presentation of the visual stimulus on the display. The retinotopy was inferred from
861 the spatial phase (location) of the stimulus that excited cells at the sweeping frequency¹⁰⁵. Images were
862 averaged across repeats for a given stimulus location (discretized in 2 deg bins) and smoothed by a
863 Gaussian filter (25 µm s.d.). For each pixel., the spatial phase of the fluorescence signal was computed by
864 Fourier transform, separately for the vertical and horizontal sweeps. The gradient of the spatial phase was
865 used to compute the field sign map¹⁰⁶. The retinotopic maps were overlaid on the maps of area boundaries
866 based on the Allen Mouse Brain Common Coordinate Framework⁵⁶, by aligning the border between V1,
867 PM, and AM (Fig. 2a)¹⁰⁷.

868
869 **Two-photon calcium imaging**
870 Imaging data were collected by a custom-built two-photon microscope. The microscope consisted of a
871 resonant scanning mirror and a galvanometric mirror, separated by a scan lens relay telescope. Excitation
872 light was delivered from Ti:sapphire laser (Coherent). The average laser power at the sample was ~50
873 mW. The emission light was separated into green and red channels by a dichroic mirror (580 nm long-
874 pass, Semrock) and bandpass filters (525/50 and 641/75 nm, Semrock), and collected by GaAsP
875 photomultiplier tubes (Hamamatsu). Signals were recorded only from the green channel for the analyses.
876 Fluorescence light collection optics were housed in an aluminum enclosure to avoid the interference of
877 visible light.

878
879 The behavioral setup (the mouse, spherical treadmill, head fixation system, and reward delivery system)
880 was mounted on a 12" x 12" breadboard (Thorlabs) on a XYZ translation stage (Dover Motion).

881
882 A Nikon 16x, 0.8 NA objective lens was used to collect images from a ~700 µm x ~700 µm plane. Scanimage
883 (Vidrio Technologies) was used to acquire 512 x 512 pixel images at 30 Hz. The imaging location and depth
884 was varied daily to sample data from a wide range of areas and depths. The image plane was chosen
885 between 100 µm and 400 µm below the dura, with the majority of planes between 100 µm and 200 µm
886 (50/56 planes). 100,000 frames were recorded in each imaging session over ~1 hour. To align timestamps
887 between the image acquisition and the virtual reality software, clock pulses were output from ScanImage
888 at each frame and from ViRMEn at each refresh of the virtual environment, and saved together in a
889 separate computer.

890
891 **Image and signal processing**
892 Acquired images were motion corrected in hierarchical steps⁴¹. First, “line-shift correction” was applied
893 to align line-by-line alternating offsets in images caused by bidirectional scanning. Then, “sample
894 movement correction” was applied to eliminate between-frame movement artifacts (rigid
895 transformation) by FFT-based 2d cross-correlation¹⁰⁸, and to mitigate within-frame movement artifacts
896 (non-rigid transformation) by Lucas-Kanade method¹⁰⁹. Finally, “sample deformation correction” was
897 applied to compensate the image deformation (non-rigid transformation) induced by expansion or

898 contraction of the brain tissue over long timescales (over minutes to an hour). This was achieved by
899 adjusting the mean image of each imaging block (1,000 frames) to the global reference image (mean
900 image of the middle block of a session), by sequential rigid, affine, and non-rigid transformations, in this
901 order. All of these transformations were combined into one nonlinear displacement field using cubic
902 interpolation and applied to the imaging data in a single step to minimize interpolation artifacts.
903

904 After the motion correction, potential fluorescence from sources and neuropils were extracted by
905 Suite2P¹¹⁰. These sources were manually curated to remove sources not corresponding to cells and those
906 with artifacts (e.g., drifting fluorescence baseline) or low signal-to-noise ratio. For the calculation of dF/F₀,
907 F₀ was estimated as the running median of the raw fluorescence signal from each source. dF was
908 estimated by subtracting neuropil fluorescence from the source fluorescence to extract the fluorescence
909 from a cell, F_{cell}, and then subtracting the baseline of F_{cell} (estimated by its running median).
910

911 dF/F was deconvolved by OASIS AR1¹¹¹, which models each fluorescence transient as a spike of an
912 instantaneous increase followed by an exponential decay, whose decay constant was fitted to each cell.
913 The deconvolved signal was sparse in time and varied in magnitude in units of dF/F. For each imaging
914 frame (35 ms bin), the deconvolved signal was binarized into a spike if the signal magnitude was greater
915 than zero, or no spike otherwise.
916

917 Researcher Degrees of Freedom

918 Before data collection, we pre-specified locations of optogenetics inhibition and the groupings of locations
919 into areas for pooled analysis based on the Allen Mouse CCF. Because our study was exploratory, we did
920 not pre-specify hypotheses to be tested, location of imaging, data analysis methods, statistical tests,
921 indexes, or metrics. We did not pre-specify the number of mice or cells to be collected, but the collected
922 data size was comparable to or larger than previous studies from our lab. For the optogenetics
923 experiments, data collection typically continued as long as the mice maintained accurate performance on
924 control trials (greater than ~90%). For the two-photon calcium imaging experiments, data collection
925 typically continued while GCaMP6s was expressed at an optimal level (~2-10 weeks after viral injection)
926 and terminated with its overexpression, which was detected by GCaMP6s expression in the nucleus of
927 several cells in fields-of-view. We excluded mice from the experiments if they did not progress to the final
928 stage of the training to perform the delayed match-to-sample task with reasonable accuracy (greater than
929 ~80% correct). We excluded imaging sessions from the analyses if the imaged area was outside of the
930 areas of interest or if the mouse performed with low accuracy (less than ~70% correct). We excluded cells
931 from the GLM-based analyses if the model fit did not converge (typically due to temporally sparse activity).
932 1–16% of cells were excluded in V1, RSC, MM, and A. The number and fraction of cells included for each
933 analysis are reported in the figure legends.
934

935 Statistical Analysis

936 Bootstrap methods were used to compute standard errors and to perform statistical tests unless noted
937 otherwise. The bootstrap methods were performed by resampling the pooled data with replacement 10⁴

938 times. For statistical tests on behavioral performance in the optogenetics experiments (Fig. 1g-m), $n_{a,i}$
939 trials were pooled across sessions for each photostimulated area (a) (or control) and for each mouse (i)
940 and bootstrapped to compute the weighted average performance P_a . For statistical tests on the activity
941 of individual cells (Figs. 3-4), cells were pooled across sessions and mice for the same imaged area and
942 bootstrapped, unless noted otherwise. For statistical tests on the activity of simultaneously imaged
943 populations (Fig. 5), cells were pooled on each session and bootstrapped.

944
945 We computed p-values for the difference across conditions as in two-tailed tests because the variable of
946 interest could be larger or smaller across conditions (e.g., areas). Specifically, we computed the fraction
947 of resampling that generated the statistic above (p_+) or below ($1-p_+$) the null hypothesis (zero difference).
948 Then the smaller of the two fractions was multiplied by two to yield the p-value. The threshold for
949 statistical significance was set at $\alpha = 0.05$. The significance threshold was adjusted for multiple
950 comparisons by Bonferroni correction, unless noted otherwise. The sample size (n), p-values, and
951 statistical significance are reported in the Figure legends.

952
953 **Choice Biases**
954 Choice biases were measured for color (i.e., turns toward a black or white T-arm) and direction (i.e., turns
955 toward a right or left T-arm) (Supplementary Fig. 1h). For each session, let $P_{X/Y}$ denote the task
956 performance (% correct) on a trial type with X sample cue and Y test cue. Then, biases were measured by
957 the following indices:

958
959 Color bias index:
960

$$\frac{|(P_{B/WB} + P_{B/WB}) - (P_{W/BW} + P_{W/WB})|}{(P_{B/WB} + P_{B/WB}) + (P_{W/BW} + P_{W/WB})} \quad (\text{Eq. 1})$$

961 Direction bias index:
962

$$\frac{|(P_{B/WB} + P_{W/BW}) - (P_{B/BW} + P_{W/WB})|}{(P_{B/WB} + P_{W/BW}) + (P_{B/BW} + P_{W/WB})} \quad (\text{Eq. 2})$$

963 Each index can range from 0 to 1, where 0 indicates no bias and 1 indicates that all choices were made for
964 a particular color or direction. Because the mice in some sessions showed running direction biases based
965 on the identity of the sample cue (Fig. 1d-e, Supplementary Fig. 1k) prior to the test cue onset, the mice
966 could show different direction biases for different sample cues (e.g., turning more to the right on black
967 sample cue trials and more to the left on white sample cue trials). To measure such a bias, we calculated
968 the direction bias index conditioned on the sample cue (Supplementary Fig. 1h), which can also range
969 from 0 to 1, as follows:

971 Direction bias index conditioned on the same sample cue:

$$\frac{1}{2} \left(\left| \frac{P_{B/WB} - P_{B/BW}}{P_{B/WB} + P_{B/BW}} \right| + \left| \frac{P_{W/BW} - P_{W/WB}}{P_{W/BW} + P_{W/WB}} \right| \right) \quad (\text{Eq. 3})$$

972

973

974 Behavioral effects of optogenetics inhibition

975 Task performance (% correct) in Fig. 1g-m was computed by pooling behavioral results from all mice ($n =$
976 4 or 7 mice for inhibition throughout a trial or inhibition in specific segments, respectively). For given
977 inhibition areas a (either a bilateral pair or area), we computed the task performance for each mouse, $P_{a,i}$,
978 where i is an index for mice. Because the number of inhibition trials for give areas, $n_{a,i}$, was different across
979 mice, the average performance across m mice was weighted based on the number of trials as follows :

980 $P_a = \sum_i^m w_{a,i} \cdot P_{a,i}$, where the weight for the i -th mouse was given by $w_{a,i} = n_{a,i} / \sum_k^m n_{a,k}$. Similarly, the

981 change in the task performance associated with the inhibition was computed by

982 $\Delta P_a = \sum_i^m w_{a,i} \cdot (P_{a,i} - P_{control,i})$, where $P_{a,i}$ and $P_{control,i}$ are the task performance during inhibition and

983 control trials for the i -th mouse, respectively.

984

985 Decoding task variables from running patterns

986 Task variables were decoded from running patterns of mice to assess whether and when they varied with
987 task variables. The running velocity was measured around the three rotation axes and z-scored. For
988 decoding of the sample cue in the delay segment, the sample cue identity (black or white) was decoded
989 from the mean z-scored velocity during the last 10 frames (~350 ms) in the delay segment (Fig. 1e,
990 Supplementary Fig. 1k). For decoding of choice in the test segment (Supplementary Fig. 1i-j), because the
991 running patterns could depend on the sample cue identity prior to the test segment (Fig. 1e,
992 Supplementary Fig. 1k), the choice (right or left) was decoded separately from trials with each identity of
993 the sample cue. The choice for a given timepoint in the test segment was decoded from the mean z-scored
994 velocity in the previous 10 frames (~350 ms), including frames from the delay segment.

995

996 Decoding was performed by first fitting a model using trials in a training set (80% of trials), and then
997 predicting the task variable from the running patterns in trials in a test set (20% of trials), cycling through
998 5 splits of test/training sets. Because both the sample cue and choice were binary variables (A or B), the
999 logit, $\log[P(A)/P(B)]$, was fitted by a weighted sum of the mean z-scored velocity by a logistic regression.
1000 Regularization and cross validation were used for fitting, following a similar procedure for fitting neural
1001 activity (see below). The identity of task variables was predicted for trials in the test set such that A was
1002 predicted if $\log[P(A)/P(B)] > 0$, and B was predicted otherwise. The decoding accuracy was the fraction of
1003 trials in which the predicted identity matched the observed identity in the experiment.

1004

1005 **Predicting choice from task variables and running patterns**

1006 The explanatory power of the task variable and running patterns on the mouse' choices was evaluated by
1007 a logistic regression. For Figure 1e, the probability of turning to choose the white side of the test cue,
1008 P_{white} , was fitted by the presented sample cue's identity, S , and decoded sample cue's identity, \hat{S} , based
1009 on the mouse's running patterns at the end of the delay segment as follows:
1010

$$\log \frac{P_{white}}{1-P_{white}} = \beta_0 + \beta_1 S + \beta_2 \hat{S} \quad (\text{Eq. 4})$$

1011
1012 We sampled an equal number of white-chosen and black-chosen trials and used L2-regularization with
1013 10-fold cross validation. If the mouse showed similar running patterns between trials with the black- and
1014 white-sample cues, β_1 would be larger than β_2 . In contrast, if the mouse showed variable but distinct
1015 running patterns that predicted the choices, as in the case of relying on the running mnemonic, β_2 would
1016 be larger than β_1 .
1017

1018 **Calculation of the mean and normalized activity across cells**

1019 Deconvolved neural activity was first smoothed by a moving average of 10 frames (350 ms) and then
1020 aligned to the start and end of the sample segment, start and end of the delay segment, start of the test
1021 segment, and T-intersection. In each segment, neural activity was plotted for the first and last parts of the
1022 segment (sample segment: first 1.2 s and last 1.2 s, delay segment: first 0.3 s and last 0.3 s, test segment:
1023 first 2 s and last 1.5 s prior to T-intersection, T-arm: 1.5 s after the T-intersection). For each cell, neural
1024 activity was averaged across all trials, and then the mean activities for individual cells imaged in a specific
1025 area (across sessions and mice) were averaged to compute the mean activity for the area (Fig. 2c). For a
1026 plot of sequential activity across cells (Fig. 2d), on each cell, activity was averaged across trials and the
1027 average activity at each time point was divided by the peak average activity across analysis time windows.
1028 Cells were then sorted in the order of peak time. The sequence of activity was cross-validated by plotting
1029 activity on even-numbered trials sorted by peak time on odd-numbered trials. For the average activity of
1030 example cells (Fig. 2e-j, Supplementary Fig. 3), the activity was smoothed by running window of 350ms
1031 (10 imaging frames), aligned to the start and end of each segment, and averaged for each trial type
1032 separately for correct and error trials.
1033

1034 **Generalized Linear Model**

1035 We used a generalized linear model (GLM) to model the time-dependent effects of experimentally
1036 measured variables, including those related to the task and the mouse's behavior, on the single trial
1037 activity of each neuron^{35,58,112,113}. Figure 2k illustrates our GLM in a schematic diagram. We used a Poisson
1038 GLM, whose output predicts a distribution of single neuron spike counts at each moment in trials.
1039

1040 The objective of our GLM is to fit the model output about the distribution of spike counts to the observed
1041 distribution of a single cell activity. The mean spike count of the Poisson GLM, μ , was related to the
1042 weighted sum of predictors ($X\beta$) by an exponential link function $\mu = \exp(X\beta)$. We will describe below (i)

1043 the design of predictors (X), (ii) regularized fitting procedure to determine the weights (β coefficients),
1044 and (iii) evaluation of model performance based on the explanatory power.

1045

1046 *Predictors*

1047 The predictors were divided into the task variable set (124 or 248 predictors) and the running variable set
1048 (39 predictors).

1049

1050 The task variable set consisted of 8 subsets: offset (O), sample cue (S), test cue (T), choice (c), and the
1051 interactions between S, T, and C ($S*T$, $T*C$, $S*C$, $S*T*C$). S, T, and C were binary variables: +1 (or -1) was
1052 assigned to white (or black) for the sample cue, BW (or WB) for the test cue, and right turn (or left turn)
1053 for the choice (Fig. 2k). Note that the interaction $S*T$ represents XOR on the sample cue identity and test
1054 cue identity and is equivalent to choice identity (C) on correct trials. Only the first 4 subsets (O, S, T, C)
1055 were used to fit correct trials in 4 trial types (4 conditions) in Figure 3. All 8 subsets were used to fit both
1056 correct and error trials in 4 trial types (2 x 4 = 8 conditions) in Figure 4. Because each cell tended to have
1057 activity in a specific part of the maze (Fig. 2d), each subset comprised 31 spatially tuned predictors that
1058 collectively covered the entire maze length, yielding $31 \times 4 = 124$ or $31 \times 8 = 248$ predictors for the task
1059 variable set. Similarly to a previous study³⁵, the spatial tuning of each cell was expanded using raised
1060 cosine basis functions with a width of 40 cm,

1061

$$f(x) = \begin{cases} V \cdot \frac{1}{2} \left[1 + \cos(2\pi \cdot \frac{(x - x_c)}{40}) \right], & \text{if } x_c - 20 < x < x_c + 20 \\ 0, & \text{otherwise} \end{cases} \quad (\text{Eq. 5})$$

1062

1063 and its center peak was either positive (+1) or negative (-1) based on the identity of a binary task variable
1064 (V), which denotes either the sample cue, test cue, choice, or their interactions. The center peaks x_c were
1065 spaced with a 20 cm interval to tile the maze with a half-width overlap.

1066

1067 The running variable set consisted of 3 subsets corresponding to the roll, pitch, and yaw velocity. For each
1068 component of velocity, the velocity was z-scored and bounded from -3 to 3. We assumed that the
1069 movement selectivity was invariant across maze position, so that movement predictors are functions of
1070 the z-scored velocity (z), but not on the maze position. The shape of velocity tuning followed one cycle of
1071 a raised cosine function with a width of 1 in z-scored velocity,

1072

$$g(z) = \begin{cases} \frac{1}{2} \left[1 + \cos(2\pi \cdot (z - z_c)) \right], & \text{if } z_c - 0.5 < z < z_c + 0.5 \\ 0, & \text{otherwise} \end{cases} \quad (\text{Eq. 6})$$

1073

1074 We included 13 predictors for each velocity component whose centers spanned from -3 to 3 with a spacing
1075 of 0.5 along z-scored velocity, yielding $13 \times 3 = 39$ predictors for the running variable set.

1076

1077 *Regularized fitting procedure*

1078 For each imaging session, the GLM was fitted to the neural activity in 80% of the trials in the training set,
1079 whereas the data in the rest of the 20% of the trials were used to evaluate the fit quality and encoded
1080 information in individual cells (see below). Trials were divided into five subsets with the same number of
1081 trials per condition (defined by the combination of the sample cue, test cue, and choice; $2 \times 2 \times 2 = 8$
1082 conditions). Four subsets were used as the training set and the remaining one subset was used as the test
1083 set. We cycled through 5 splits of test/training set to evaluate all appropriate trials in the session.

1084

1085 Given the model output of the expected spike counts, $\mu = \exp(X\beta)$, the likelihood of observing spike
1086 counts, r , follows a Poisson distribution: $P(r|\mu) = \mu^r \exp(-\mu)/r!$. The weights $\beta = [\beta_0 \dots \beta_M]$ were fitted to
1087 the data by minimizing the following objective function with glmnet package in R with elastic-net
1088 regularization¹¹⁴:

1089

$$-\frac{1}{N} \sum_{i=1}^N [r_i(\beta_0 + \beta^T \cdot x_i) - \exp(\beta_0 + \beta^T \cdot x_i)] + \lambda \left[\alpha \sum_{j=1}^M |\beta_j| + (1-\alpha) \sum_{j=1}^M \frac{\beta_j^2}{2} \right] \quad (\text{Eq. 7})$$

1090

1091 Here i is an index for the imaging frame, N is the total number of frames in the training data, j is an index
1092 for beta coefficients, and M is a total number of beta coefficients without β_0 ($M = 124$ or 248 for full
1093 model). r_i is the neural activity in the i -th frame calculated by the sum of estimated spike counts in
1094 neighboring 10 frames ($[i-5 \dots i+4]$ th frames spanning ~ 350 ms). x_i is a set of values (i.e., a vector) of M
1095 predictors for the i -th frame, β is a vector of M beta coefficients for the cell. We used L1-like regularization
1096 with $\alpha=0.95$, which tends to explain responses with a smaller number of large beta coefficients (as
1097 opposed to a large number of small beta coefficients for L2 regularization with $\alpha \approx 0$).

1098

1099 The regularization parameter, λ , sets the tradeoff between the fitting error (the first term in Eq 7) and the
1100 model complexity (the second term in Eq 7). The value of λ was chosen from a set of λ values by 10 fold
1101 cross validation, where each fold had an equal number of trials per condition (as in the training/test splits
1102 described above). For each value of λ , we computed 10 instances of the fitting error (deviance) from the
1103 cross validation and computed their mean, μ_λ , and standard deviation, σ_λ (i.e., standard error of the
1104 deviance). We found the λ_{\min} that produced the minimum deviance $\mu_{\lambda_{\min}}$, and $\lambda_{1\text{se}}$ that produced the most
1105 regularized model whose mean deviance was within one standard error from the minimum deviance,
1106 $\arg \max_{\lambda \in [\lambda_{\min}, \infty]} (\mu_\lambda < \mu_{\lambda_{\min}} + \sigma_{\lambda_{\min}})$. We used $\lambda_{1\text{se}}$ to fit the model to all trials in the training set, and obtained
1107

1108 fitted beta coefficients, $\beta_{1\text{se}}$, which were used to predict responses for trials in the test set and to evaluate
1109 information for task variables (Figs. 3-4, see below).

1110

1111 Because the number of correct trials was greater than error trials, the imbalance in the number of trials
1112 could bias the fitting procedure to depend more on correct trials than on error trials. To compensate for
1113 this imbalance, we adjusted the weight of each trial during the fit. Specifically, on each trial with a specific

1113 trial type and trial outcome (correct or error), the fitting error of that trial was multiplied by the inverse
1114 of the total number of trials with the same trial type and outcome during the session. Results were
1115 qualitatively consistent with and without this balancing for differences in trial numbers.

1116

1117 *Evaluation of model performance*

1118 The model performance was evaluated by the fraction of the deviance explained (FDE) on the test data
1119 set (Fig. 2l-m). FDE quantifies the performance of the fitted GLM on the test data with respect to the *null*
1120 and *saturated (sat)* models. For each time point in the test data, the null model predicts the same
1121 expected activity, which is given by the activity of a cell averaged across all time points in the training
1122 data. In contrast, the saturated model predicts the expected activity that exactly matches the observed
1123 activity at each time point in the test data. Let L_{GLM} , L_{null} , and L_{sat} be the likelihood of observing the test
1124 data given the GLM, null, and saturated model, respectively. Then, the deviance (D) and the FDE are
1125 defined as follows.

1126

$$\begin{cases} D_{null} = 2(L_{sat} - L_{null}) \\ D_{GLM} = 2(L_{sat} - L_{GLM}) \end{cases} \quad (\text{Eq. 8})$$

1127

$$\begin{aligned} FDE &= \frac{D_{null} - D_{GLM}}{D_{null}} \\ &= \frac{L_{GLM} - L_{null}}{L_{sat} - L_{null}} \end{aligned} \quad (\text{Eq. 9})$$

1128

1129 Thus, FDE = 1 indicates that the model prediction was as good as the saturated model, whereas FDE = 0
1130 indicates that the model prediction was as poor as the null model.

1131

1132 **Single cell information**

1133 We used the GLM fitted to the training data to compute the single-trial information for each cell about
1134 each task variable in each trial in the test data. We first describe the derivation of sample cue information
1135 below, and this derivation extends easily to test cue information and XOR information. Given that the
1136 activity of a cell at time t in a given trial had a value of $r(t)$, we used the Poisson GLM to compute the
1137 likelihood that the observed activity was generated either in the presence of a white sample cue ($S = +1$)
1138 or a black sample cue ($S = -1$). Then, the single-trial information was computed as the log likelihood ratio
1139 ($\log LR$)^{61,62,115}:

1140

$$\log \frac{P(r(t) | S = 1)}{P(r(t) | S = -1)} \quad (\text{Eq. 10})$$

1141

1142 The $\log LR$ monotonically varies with the likelihood ratio, its sign indicates whether white (positive) or black
1143 (negative) was more likely, and its magnitude (absolute value) quantifies its informativeness. Because the

running patterns of the mice can covary with the task variable identities (Fig. 1e, Supplementary Fig. 1k) and influence the neural activity^{18,59,116}, we controlled for running variability to derive “genuine” sample cue information by computing the log likelihood also conditioned on the running velocity as follows.

$$\log \frac{P(r(t) | S = 1, V(t))}{P(r(t) | S = -1, V(t))} \quad (\text{Eq. 11})$$

To compute the likelihood of the given sample cue, we marginalized over all possible combinations of the remaining task variables (i.e., test cue and choice in this case).

$$\begin{aligned} P(r(t) | S = 1, V(t)) &= \sum_{T \in \{-1, 1\}} \sum_{C \in \{-1, 1\}} P(r(t) | S = 1, T, C, V(t)) \cdot P(T, C | S = 1, V(t)) \\ &= \sum_{T \in \{-1, 1\}} \sum_{C \in \{-1, 1\}} P(r(t) | S = 1, T, C, V(t)) \cdot P(T, C | S = 1) \\ &= P(r | S = 1, T = -1, C = -1) \cdot P_c / 2 + P(r | S = 1, T = -1, C = 1) \cdot P_e / 2 + P(r | S = 1, T = 1, C = -1) \cdot P_e / 2 + P(r | S = 1, T = 1, C = 1) \cdot P_c / 2 \end{aligned} \quad (\text{Eq. 12})$$

Note that $P(T, C | S=1)$ was approximated by $P_c/2$ or $P_e/2$, where the P_c and P_e denote the proportion of correct trials and that of error trials, respectively.

In a similar fashion, test cue information was computed as:

$$\log \frac{P(r(t) | T = 1, V(t))}{P(r(t) | T = -1, V(t))} = \log \frac{\sum_S \sum_C P(r(t) | S, T = 1, C, V(t)) \cdot P(S, C | T = 1, V(t))}{\sum_S \sum_C P(r(t) | S, T = -1, C, V(t)) \cdot P(S, C | T = -1, V(t))} \quad (\text{Eq. 13})$$

For logLR of XOR, the likelihood was marginalized over the combinations of the sample cue and test cue that were associated with the same direction of reward assignment (e.g., XOR = 1 consists of $[S=1, T=1]$ and $[S=-1, T=-1]$). Thus, its logLR was calculated as follows.

$$\begin{aligned} \log \frac{P(r(t) | XOR = 1, V(t))}{P(r(t) | XOR = -1, V(t))} &= \log \frac{\sum_{\{S, T\} \in \{[1, 1], [-1, -1]\}} \sum_C P(r(t) | S, T, C, V(t)) \cdot P(C | S, T, V(t))}{\sum_{\{S, T\} \in \{[1, 1], [-1, -1]\}} \sum_C P(r(t) | S, T, C, V(t)) \cdot P(C | S, T, V(t))} \\ &= \log \frac{\sum_{\{S, T\} \in \{[1, 1], [-1, -1]\}} \sum_C P(r(t) | S, T, C, V(t)) \cdot P(C | S, T)}{\sum_{\{S, T\} \in \{[1, 1], [-1, -1]\}} \sum_C P(r(t) | S, T, C, V(t)) \cdot P(C | S, T)} \\ &= \log \frac{P(r(t) | S = 1, T = 1, C = 1, V(t)) \cdot P_c / 2 + P(r(t) | S = 1, T = 1, C = -1, V(t)) \cdot P_e / 2 + P(r(t) | S = -1, T = -1, C = 1, V(t)) \cdot P_c / 2 + P(r(t) | S = -1, T = -1, C = -1, V(t)) \cdot P_e / 2}{P(r(t) | S = 1, T = -1, C = 1, V(t)) \cdot P_c / 2 + P(r(t) | S = 1, T = -1, C = -1, V(t)) \cdot P_e / 2 + P(r(t) | S = -1, T = 1, C = 1, V(t)) \cdot P_c / 2 + P(r(t) | S = -1, T = 1, C = -1, V(t)) \cdot P_e / 2} \end{aligned} \quad (\text{Eq. 14})$$

Note that the logLR is a signed value, where its sign indicates whether the activity supports one identity of the task variables or the other. For example, cells with the sample cue selectivity tend to show positive logLR for trials with $S = +1$ (white sample cue) and negative logLR for trials with $S = -1$ (black sample cue). As a result, if we simply average the logLR across all trials, they would cancel out and fail to detect the sample cue information. Therefore, we adjusted the sign of logLR, so that a positive logLR indicated that

1171 the neural activity correctly encoded the task variable identity observed in the trial. In contrast, a negative
 1172 logLR indicated incorrect encoding of the task variable identity. Specifically, when the observed task
 1173 variable identity was -1 in Equations 11-14, we multiplied the logLR by -1. In the results, we used the sign-
 1174 adjusted logLR (Figs. 3-5, Supplementary Figs. 4-6).

1175

1176 Population information and decoding

1177 Population information was derived similarly to single cell information, except that a single cell activity
 1178 $r(t)$ was replaced by a vector of population activity, $\mathbf{r}(t)$, which was imaged simultaneously on each session
 1179 within a given field-of-view ($\sim 0.5 \text{ mm}^2$ area). Under the assumption of conditionally independent noise
 1180 across cells, the likelihood of observing a population activity $\mathbf{r}(t)$ was calculated as follows:

1181

$$P(\mathbf{r}(t) | S, T, C, V(t)) = \prod_{i=1}^n P(r_i(t) | S, T, C, V(t)) \quad (\text{Eq. 15})$$

1182

1183 where i is an index for a cell in a population of n cells. Combining Equations 14 and 15 yields population
 1184 XOR information as follows:

1185

$$\begin{aligned} & \log \frac{P(\mathbf{r}(t) | \text{XOR} = 1, V(t))}{P(\mathbf{r}(t) | \text{XOR} = -1, V(t))} \\ &= \log \frac{\sum_{\substack{(S,T,C) \in \{1,-1\}^3 \\ (S,T) \in \{1,-1\}^2}} \sum_C P(\mathbf{r}(t) | S, T, C, V(t)) \cdot P(C | S, T, V(t))}{\sum_{\substack{(S,T,C) \in \{1,-1\}^3 \\ (S,T) \in \{1,-1\}^2}} \sum_C P(\mathbf{r}(t) | S, T, C, V(t)) \cdot P(C | S, T, V(t))} \\ &= \log \frac{\sum_{\substack{(S,T,C) \in \{1,-1\}^3 \\ (S,T) \in \{1,-1\}^2}} \sum_C P(\mathbf{r}(t) | S, T, C, V(t)) \cdot P(C | S, T)}{\sum_{\substack{(S,T,C) \in \{1,-1\}^3 \\ (S,T) \in \{1,-1\}^2}} \sum_C P(\mathbf{r}(t) | S, T, C, V(t)) \cdot P(C | S, T)} \quad (\text{Eq. 16}) \\ &= \log \frac{P(\mathbf{r}(t) | S = 1, T = 1, C = 1, V(t)) \cdot Pe / 2 + P(\mathbf{r}(t) | S = 1, T = 1, C = -1, V(t)) \cdot Pe / 2 + P(\mathbf{r}(t) | S = -1, T = -1, C = 1, V(t)) \cdot Pc / 2 + P(\mathbf{r}(t) | S = -1, T = -1, C = -1, V(t)) \cdot Pe / 2}{P(\mathbf{r}(t) | S = 1, T = -1, C = -1, V(t)) \cdot Pc / 2 + P(\mathbf{r}(t) | S = 1, T = -1, C = 1, V(t)) \cdot Pe / 2 + P(\mathbf{r}(t) | S = -1, T = 1, C = -1, V(t)) \cdot Pe / 2 + P(\mathbf{r}(t) | S = -1, T = 1, C = 1, V(t)) \cdot Pe / 2} \\ &= \log \frac{\prod_{j=1}^n P(r_j(t) | S = 1, T = 1, C = 1, V(t)) \cdot Pe / 2 + \prod_{j=1}^n P(r_j(t) | S = 1, T = 1, C = -1, V(t)) \cdot Pe / 2 + \prod_{j=1}^n P(r_j(t) | S = -1, T = -1, C = 1, V(t)) \cdot Pc / 2 + \prod_{j=1}^n P(r_j(t) | S = -1, T = -1, C = -1, V(t)) \cdot Pe / 2}{\prod_{j=1}^n P(r_j(t) | S = 1, T = -1, C = -1, V(t)) \cdot Pc / 2 + \prod_{j=1}^n P(r_j(t) | S = 1, T = -1, C = 1, V(t)) \cdot Pe / 2 + \prod_{j=1}^n P(r_j(t) | S = -1, T = 1, C = -1, V(t)) \cdot Pe / 2 + \prod_{j=1}^n P(r_j(t) | S = -1, T = 1, C = 1, V(t)) \cdot Pe / 2} \end{aligned}$$

1186

1187

1188

1189 The population information was derived using all cells in each imaging sessions (Fig. 5), or a subpopulation
 1190 with the same number of cells ($n = 100$ cells, randomly sampled from the population, Supplementary Fig.
 1191 5).

1192

1193 The identity of the task variable was decoded from population activity based on the sign of population
 1194 information (logLR). When logLR was zero, the decoded identity was randomly assigned. On each session,
 1195 the accuracy of the population coding was evaluated by mutual information between the true and
 1196 decoded identity of the task variable. The weighted average of mutual information was reported by
 1197 averaging across sessions with weights proportional to the number of trials on the sessions (Fig. 5b,d,
 1198 Supplementary Figs. 5a,c, 6d).

1199

1200 Signal and noise correlation

1201 For each pair of cells recorded simultaneously, the signal correlation was quantified by Pearson's
1202 correlation on their mean neural activity across four trial types. To compute the noise correlation for each
1203 pair, the *residual* neural activity was derived for each cell on each trial type, by subtracting the mean
1204 activity on each trial type from the observed activity on that trial type. The noise correlation was
1205 quantified by Pearson's correlation on the residual activity of the pair of neurons combined across all trials
1206 in all trial types. To evaluate the effect of noise correlation on the accuracy of the population code, the
1207 noise correlation was disrupted by shuffling the trial identity within each trial type separately for correct
1208 and error trials. Trial shuffling was repeated 10,000 times to estimate the standard error of decoding
1209 accuracy.

1210

1211 **Simulation of population activity**

1212 To compare the efficiency and accuracy of encoded information between a population of mixed selectivity
1213 cells and a population of pure selectivity cells, we generated population activity by Monte-Carlo
1214 simulation and analyzed the simulated data similarly to the real imaging data. The number of spikes
1215 generated by each cell follows a Poisson distribution with the mean λ . Each cell responds to a preferred
1216 cue (or a preferred combination of cues) with the mean of λ_{pref} and to an unpreferred cue with the mean
1217 of λ_{unpref} , where λ_{pref} is greater than λ_{unpref} by design. The minimum unit population size was a set of four
1218 cells, each of which preferentially responds to a specific trial type in the mixed selectivity population, or
1219 to a specific sample cue or test cue identity in the pure selectivity population (Supplementary Fig. 7a). In
1220 our simulation, we varied the population size by adding N sets of the unit population and varied the level
1221 of noise correlations across cells. Because the noise correlations were mostly observed for cells with a
1222 higher signal correlation (Supplementary Fig. 6a-c), the simulation included positive noise correlation only
1223 between cells that shared the same selectivity. To introduce noise correlations across n cells, our
1224 simulation first generated a set of n Gaussian-distributed random variables with an n-by-n correlation
1225 matrix using *compularnd.m* in MATLAB (MathWorks), and then correlated Poisson-distributed random
1226 variables were generated by the inverse CDF sampling technique¹¹⁷ using *poissinv.m* in MATLAB
1227 (MathWorks). Population decoding was performed by following the decoding method for the real imaging
1228 data as described above. The total of 10,000 trials were simulated 10,000 times for each set of free
1229 parameters to estimate the mean and standard error of the decoding accuracy.

1230

1231 **Analyses conditioned on the cue information**

1232 To evaluate the ratio of information for the sample cue vs. test cue across individual cells, the two types
1233 of information represented in the cartesian coordinates (Figs. 3g, 4h) were converted to polar coordinates
1234 (Figs. 3h-l, 4i-j). For the analyses that are conditioned on the polar angle (Figs. 3h-l, 4i-j, 5, Supplementary
1235 Figs. 4-6), cells with zero or noise-level information ($|\log LR| < \varepsilon$) were excluded from the analyses because
1236 their angle could not be reliably estimated. The noise level ε was set to 0.01. The skewness of the angle
1237 distribution of cells was calculated without cells with extreme angles (the highest and lowest 1% of cells)
1238 because the skewness is sensitive to outliers. To show the angle distribution of cells, histograms were
1239 created by discretizing the angles into 7 bins (Figs. 3i, 4i). Bins for cells with only sample cue information
1240 or test cue information ($\theta = 0^\circ$ and $\theta = 90^\circ$) included cells within a chance-level deviation from the two
1241 axes. The chance-level deviation was logLR of 0.017 for V1, 0.007 for RSC, and 0.005 for MM, inferred for

1242 each cortical area by one standard deviation of the test cue information averaged across the last 1 s (30
1243 frames) in the sample segment (i.e., prior to the appearance of the test cue). For the evaluation of
1244 population information (Fig. 5, Supplementary Fig. 5-6), cells in the bins for $\theta = 0^\circ$ and $\theta = 90^\circ$ with less
1245 than the chance-level magnitude of XOR information (Fig. 4i, correct trials) were defined to have pure
1246 selectivity to the sample cue and test cue, respectively, whereas cells with $15 < \theta < 75$ (Fig. 4h, correct
1247 trials) were defined to have mixed selectivity. Similarly, pure XOR selective cells were defined to have XOR
1248 information greater than logLR of 0.01 and less than the chance-level magnitude of the sample and test
1249 cue information (Supplementary Fig. 4i-j).

1250

1251 **Comparison of XOR information for correct vs. error trials**

1252 We tested whether XOR information between correct and error trials was different conditioned on the
1253 same amount of preexisting sample cue information (Fig. 4k). Trials were binned according to their sample
1254 cue information at the end of the delay segment (bin size = 0.01 logLR). The mean XOR information for

1255 correct and error trials was calculated by averaging over trials within a bin, $\bar{I}_{\{\text{XOR},\text{cor}\}} = \frac{1}{Nc} \sum_i^{Nc} I_{i,\{\text{XOR},\text{cor}\}}$

1256 and $\bar{I}_{\{\text{XOR},\text{err}\}} = \frac{1}{Ne} \sum_j^{Ne} I_{j,\{\text{XOR},\text{err}\}}$, where Nc and Ne are the number of correct and error trials within the

1257 bin (combined across sessions), respectively; $I_{i,\{\text{XOR},\text{cor}\}}$ and $I_{j,\{\text{XOR},\text{err}\}}$ are the mean XOR information
1258 across all cells in a session for the i -th correct and j -th error trials within the bin, respectively. $\bar{I}_{\{\text{XOR},\text{cor}\}}$
1259 and $\bar{I}_{\{\text{XOR},\text{err}\}}$ were computed 10^4 times by bootstrapping on trials, and the statistical significance of their
1260 difference was tested against a null hypothesis $\bar{I}_{\{\text{XOR},\text{cor}\}} = \bar{I}_{\{\text{XOR},\text{err}\}}$. For comparison of two areas (A and
1261 B), we tested whether area A showed a larger difference in XOR information between correct vs. error
1262 trials than area B. $\Delta\bar{I}_{\{\text{XOR}\}} = \bar{I}_{\{\text{XOR},\text{err}\}} - \bar{I}_{\{\text{XOR},\text{cor}\}}$ was computed for the two areas A and B, denoted as
1263 $\Delta\bar{I}_{A,\{\text{XOR}\}}$ and $\Delta\bar{I}_{B,\{\text{XOR}\}}$. The statistical significance of their difference was tested against a null
1264 hypothesis $\Delta\bar{I}_{A,\{\text{XOR}\}} = \Delta\bar{I}_{B,\{\text{XOR}\}}$ by bootstrapping on trials.

1265

1266 **Sparsity index**

1267 For a model-free evaluation of the neural selectivity to a specific trial type, the sparsity index was
1268 calculated for individual cells (Fig. 3k, Supplementary Fig. 4g). Let $\mathbf{r} = [r_1 \dots r_4]$ denote the estimated spike
1269 counts averaged across trials within each of the 4 trial types. Then, \mathbf{r} was multiplied by a normalization

1270 factor, $k = 4 / \sum_{i=1}^4 r_i$, so that the average of $[kr_1 \dots kr_4]$ was 1 (and the sum was 4). The sparsity index was

1271 defined as the maximum of the normalized activity:

1272

$$1273 \text{SI} = \max([kr_1, kr_2, kr_3, kr_4]) \quad (\text{Eq 17})$$

1274

1275 The index ranged from 1 to 4 as shown for example activity patterns in Figure 3m. The minimum index of
1276 1 was assigned to cells that showed the same average activity across the four trial types (i.e., no trial type
1277 selectivity). The maximum index of 4 was assigned to cells that showed activity only for a single trial type.
1278 To compute the sparsity index for the test segment, the neural activity r_i was calculated from the mean
1279 estimated spike counts during the first 1 s (30 imaging frames) in the test segment on correct trials.
1280

1281 Nonlinearity index

1282 For evaluation of nonlinear mixing of information (or nonlinear mixed selectivity), the nonlinearity index
1283 was calculated for individual cells (Fig. 3l, Supplementary Fig. 4h). Let $r_{X/Y}$ denote the neural activity for
1284 the trial type with X sample cue and Y test cue. If a cell has linear mixed selectivity to sample cue and test
1285 cue, the activity differences associated with the different test cues are the same regardless of the sample
1286 cue ($r_{B/BW} - r_{B/WB} = r_{W/BW} - r_{W/WB}$). In contrast, if a cell has nonlinear mixed selectivity, these differences are
1287 not equal. To quantify the degree of nonlinearity, the nonlinearity index (NI) was defined as:

1288

$$1289 NI = |(kr_{B/BW} - kr_{B/WB}) - (kr_{W/BW} - kr_{W/WB})| \quad (\text{Eq 18})$$

1290

1291 where k is the normalization factor used for the sparsity index (see above). The index ranged from 0 to 4
1292 as shown for example activity patterns in Figure 3m. The minimum index of 0 was assigned to cells that
1293 showed no trial type selectivity, pure selectivity, or linear mixed selectivity (top three panels in Fig. 3m).
1294 The maximum index of 4 was assigned to cells that showed no activity for left-choice trials ($r_{B/BW} = 0$ and
1295 $r_{W/WB} = 0$) or no activity for right-choice trials ($r_{B/WB} = 0$ and $r_{W/BW} = 0$), including cells that showed activity
1296 only on a single trial type. To compute the nonlinearity index for the test segment, the neural activity, $r_{X/Y}$,
1297 was calculated from the mean estimated spike counts during the first 1 s (30 imaging frames) in the test
1298 segment on correct trials.

1299

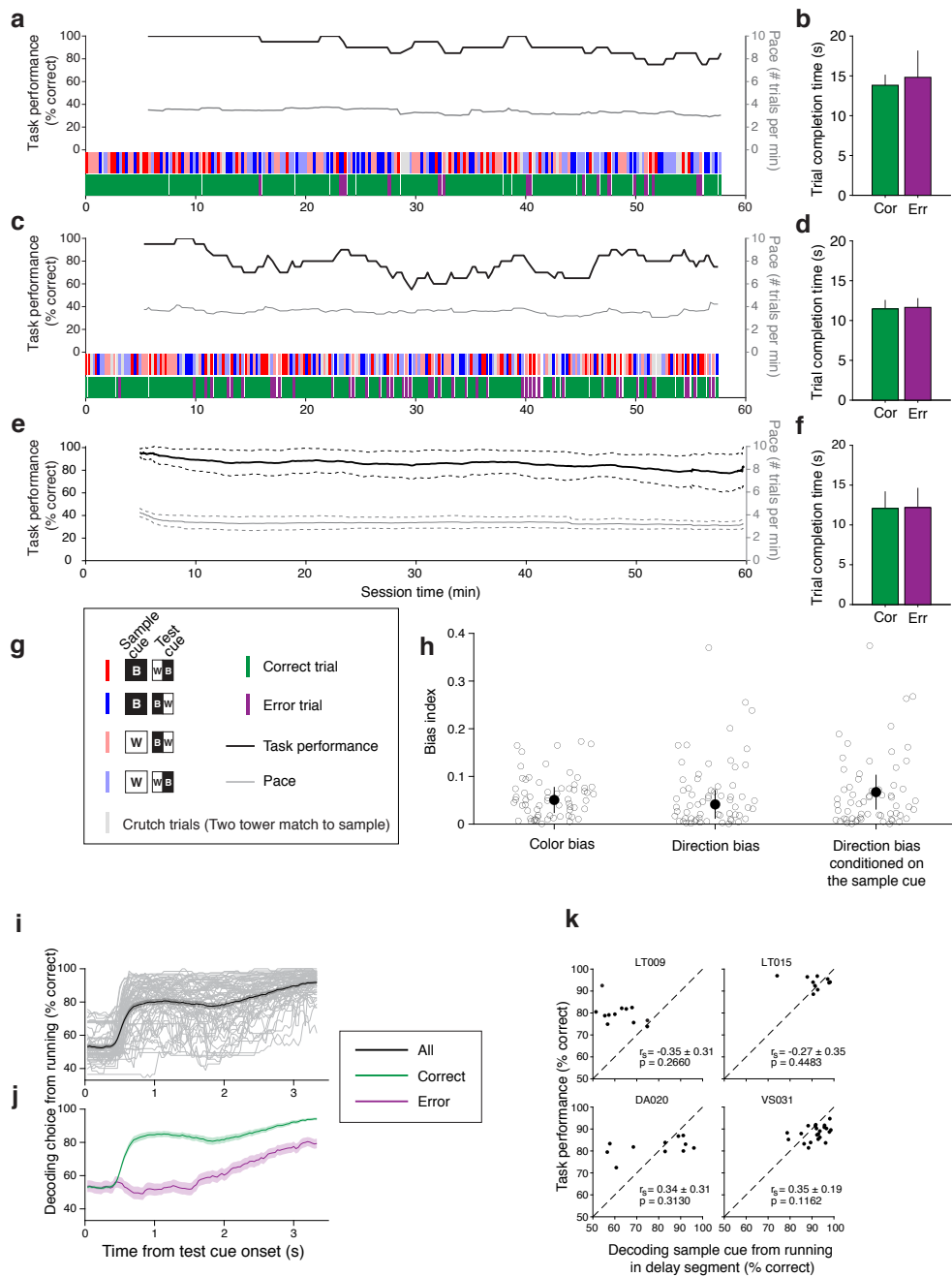
References

1. Cisek, P. Resynthesizing behavior through phylogenetic refinement. *Atten Percept Psychophys* **81**, 2265-2287 (2019).
2. Ramus, S.J. & Eichenbaum, H. Neural correlates of olfactory recognition memory in the rat orbitofrontal cortex. *J Neurosci* **20**, 8199-8208 (2000).
3. Wu, Z., et al. Context-Dependent Decision Making in a Premotor Circuit. *Neuron* **106**, 316-328 (2020).
4. Condylis, C., et al. Context-Dependent Sensory Processing across Primary and Secondary Somatosensory Cortex. *Neuron* **106**, 515-525 (2020).
5. Freedman, D.J. & Assad, J.A. Experience-dependent representation of visual categories in parietal cortex. *Nature* **443**, 85-88 (2006).
6. Miller, E.K. & Desimone, R. Parallel neuronal mechanisms for short-term memory. *Science* **263**, 520-522 (1994).
7. Bennur, S. & Gold, J.I. Distinct representations of a perceptual decision and the associated oculomotor plan in the monkey lateral intraparietal area. *J Neurosci* **31**, 913-921 (2011).
8. Pagan, M., Urban, L.S., Wohl, M.P. & Rust, N.C. Signals in inferotemporal and perirhinal cortex suggest an untangling of visual target information. *Nat. Neurosci.* **16**, 1132-1139 (2013).
9. Rossi-Pool, R., et al. Decoding a Decision Process in the Neuronal Population of Dorsal Premotor Cortex. *Neuron* **96**, 1432-1446 (2017).
10. Mante, V., Sussillo, D., Shenoy, K.V. & Newsome, W.T. Context-dependent computation by recurrent dynamics in prefrontal cortex. *Nature* **503**, 78-84 (2013).
11. Wimmer, R.D., et al. Thalamic control of sensory selection in divided attention. *Nature* **526**, 705-709 (2015).
12. Banerjee, A., et al. Value-guided remapping of sensory cortex by lateral orbitofrontal cortex. *Nature* **585**, 245-250 (2020).
13. Reinert, S., Hubener, M., Bonhoeffer, T. & Goltstein, P.M. Mouse prefrontal cortex represents learned rules for categorization. *Nature* **593**, 411-417 (2021).
14. Duan, C.A., Erlich, J.C. & Brody, C.D. Requirement of Prefrontal and Midbrain Regions for Rapid Executive Control of Behavior in the Rat. *Neuron* **86**, 1491-1503 (2015).
15. Duan, C.A., et al. Collicular circuits for flexible sensorimotor routing. *Nat. Neurosci.* (2021).
16. Moser, E.I., Kropff, E. & Moser, M.B. Place cells, grid cells, and the brain's spatial representation system. *Annu. Rev. Neurosci.* **31**, 69-89 (2008).
17. Bicanski, A. & Burgess, N. Neuronal vector coding in spatial cognition. *Nat. Rev. Neurosci.* **21**, 453-470 (2020).
18. Whitlock, J.R., Pfuhl, G., Dagslott, N., Moser, M.B. & Moser, E.I. Functional split between parietal and entorhinal cortices in the rat. *Neuron* **73**, 789-802 (2012).
19. Nitz, D.A. Tracking route progression in the posterior parietal cortex. *Neuron* **49**, 747-756 (2006).
20. Clark, B.J., Simmons, C.M., Berkowitz, L.E. & Wilber, A.A. The retrosplenial-parietal network and reference frame coordination for spatial navigation. *Behav. Neurosci.* **132**, 416-429 (2018).
21. Nitz, D.A. Spaces within spaces: rat parietal cortex neurons register position across three reference frames. *Nat. Neurosci.* **15**, 1365-1367 (2012).
22. Krumin, M., Lee, J.J., Harris, K.D. & Carandini, M. Decision and navigation in mouse parietal cortex. *eLife* **7** (2018).
23. Chen, L.L., Lin, L.H., Green, E.J., Barnes, C.A. & McNaughton, B.L. Head-direction cells in the rat posterior cortex. I. Anatomical distribution and behavioral modulation. *Exp. Brain Res.* **101**, 8-23 (1994).
24. Alexander, A.S. & Nitz, D.A. Retrosplenial cortex maps the conjunction of internal and external spaces. *Nat. Neurosci.* **18**, 1143-1151 (2015).
25. Alexander, A.S. & Nitz, D.A. Spatially Periodic Activation Patterns of Retrosplenial Cortex Encode Route Sub-spaces and Distance Traveled. *Curr. Biol.* **27**, 1551-1560 (2017).
26. McNaughton, B.L., et al. Cortical representation of motion during unrestrained spatial navigation in the rat. *Cereb. Cortex* **4**, 27-39 (1994).
27. Cho, J. & Sharp, P.E. Head direction, place, and movement correlates for cells in the rat retrosplenial cortex. *Behav. Neurosci.* **115**, 3-25 (2001).
28. Wilber, A.A., Clark, B.J., Forster, T.C., Tatsuno, M. & McNaughton, B.L. Interaction of egocentric and world-centered reference frames in the rat posterior parietal cortex. *J Neurosci* **34**, 5431-5446 (2014).
29. Alexander, A.S., et al. Egocentric boundary vector tuning of the retrosplenial cortex. *Sci Adv* **6**, eaaz2322 (2020).
30. Keshavarzi, S., et al. Multisensory coding of angular head velocity in the retrosplenial cortex. *Neuron* (2021).

31. Saleem, A.B., Diamanti, E.M., Fournier, J., Harris, K.D. & Carandini, M. Coherent encoding of subjective spatial position in visual cortex and hippocampus. *Nature* **562**, 124-127 (2018).
32. Diamanti, E.M., et al. Spatial modulation of visual signals arises in cortex with active navigation. *bioRxiv* (2020).
33. Harvey, C.D., Coen, P. & Tank, D.W. Choice-specific sequences in parietal cortex during a virtual-navigation decision task. *Nature* **484**, 62-68 (2012).
34. Morcos, A.S. & Harvey, C.D. History-dependent variability in population dynamics during evidence accumulation in cortex. *Nat. Neurosci.* **19**, 1672-1681 (2016).
35. Runyan, C.A., Piasini, E., Panzeri, S. & Harvey, C.D. Distinct timescales of population coding across cortex. *Nature* **548**, 92-96 (2017).
36. Koay, S.A., Thibierge, S., Brody, C.D. & Tank, D.W. Amplitude modulations of cortical sensory responses in pulsatile evidence accumulation. *eLife* **9** (2020).
37. Koay, S.A., Charles, A.S., Thibierge, S.Y., Brody, C.D. & Tank, D.W. Sequential and efficient neural-population coding of complex task information. *Neuron* (2021).
38. Franco, L.M. & Goard, M.J. A distributed circuit for associating environmental context with motor choice in retrosplenial cortex. *Sci Adv* **7** (2021).
39. Pinto, L., et al. Task-Dependent Changes in the Large-Scale Dynamics and Necessity of Cortical Regions. *Neuron* **104**, 810-824 (2019).
40. Pinto, L., et al. An Accumulation-of-Evidence Task Using Visual Pulses for Mice Navigating in Virtual Reality. *Front. Behav. Neurosci.* **12**, 36 (2018).
41. Driscoll, L.N., Pettit, N.L., Minderer, M., Chettih, S.N. & Harvey, C.D. Dynamic Reorganization of Neuronal Activity Patterns in Parietal Cortex. *Cell* **170**, 986-999 e916 (2017).
42. Cowansage, K.K., et al. Direct reactivation of a coherent neocortical memory of context. *Neuron* **84**, 432-441 (2014).
43. Keene, C.S. & Bucci, D.J. Contributions of the retrosplenial and posterior parietal cortices to cue-specific and contextual fear conditioning. *Behav. Neurosci.* **122**, 89-97 (2008).
44. Keene, C.S. & Bucci, D.J. Neurotoxic lesions of retrosplenial cortex disrupt signaled and unsignaled contextual fear conditioning. *Behav. Neurosci.* **122**, 1070-1077 (2008).
45. Freedman, D.J., Riesenhuber, M., Poggio, T. & Miller, E.K. Categorical representation of visual stimuli in the primate prefrontal cortex. *Science* **291**, 312-316 (2001).
46. Daniel, T.A., Katz, J.S. & Robinson, J.L. Delayed match-to-sample in working memory: A BrainMap meta-analysis. *Biol. Psychol.* **120**, 10-20 (2016).
47. Guo, Z.V., et al. Flow of cortical activity underlying a tactile decision in mice. *Neuron* **81**, 179-194 (2014).
48. Li, N., et al. Spatiotemporal constraints on optogenetic inactivation in cortical circuits. *eLife* **8** (2019).
49. Masse, N.Y., Rosen, M.C. & Freedman, D.J. Reevaluating the Role of Persistent Neural Activity in Short-Term Memory. *Trends in cognitive sciences* **24**, 242-258 (2020).
50. Mongillo, G., Barak, O. & Tsodyks, M. Synaptic theory of working memory. *Science* **319**, 1543-1546 (2008).
51. Masse, N.Y., Yang, G.R., Song, H.F., Wang, X.J. & Freedman, D.J. Circuit mechanisms for the maintenance and manipulation of information in working memory. *Nat. Neurosci.* **22**, 1159-1167 (2019).
52. Vann, S.D. & Aggleton, J.P. Extensive cytotoxic lesions of the rat retrosplenial cortex reveal consistent deficits on tasks that tax allocentric spatial memory. *Behav. Neurosci.* **116**, 85-94 (2002).
53. Vann, S.D. & Aggleton, J.P. Testing the importance of the retrosplenial guidance system: effects of different sized retrosplenial cortex lesions on heading direction and spatial working memory. *Behav. Brain Res.* **155**, 97-108 (2004).
54. Minderer, M., Brown, K.D. & Harvey, C.D. The Spatial Structure of Neural Encoding in Mouse Posterior Cortex during Navigation. *Neuron* **102**, 232-248 (2019).
55. Gamanut, R., et al. The Mouse Cortical Connectome, Characterized by an Ultra-Dense Cortical Graph, Maintains Specificity by Distinct Connectivity Profiles. *Neuron* **97**, 698-715 (2018).
56. Wang, Q., et al. The Allen Mouse Brain Common Coordinate Framework: A 3D Reference Atlas. *Cell* **181**, 936-953 (2020).
57. Wang, Q. & Burkhalter, A. Area map of mouse visual cortex. *J. Comp. Neurol.* **502**, 339-357 (2007).
58. Park, I.M., Meister, M.L., Huk, A.C. & Pillow, J.W. Encoding and decoding in parietal cortex during sensorimotor decision-making. *Nat. Neurosci.* **17**, 1395-1403 (2014).
59. Musall, S., Kaufman, M.T., Juavinett, A.L., Gluf, S. & Churchland, A.K. Single-trial neural dynamics are dominated by richly varied movements. *Nat. Neurosci.* **22**, 1677-1686 (2019).

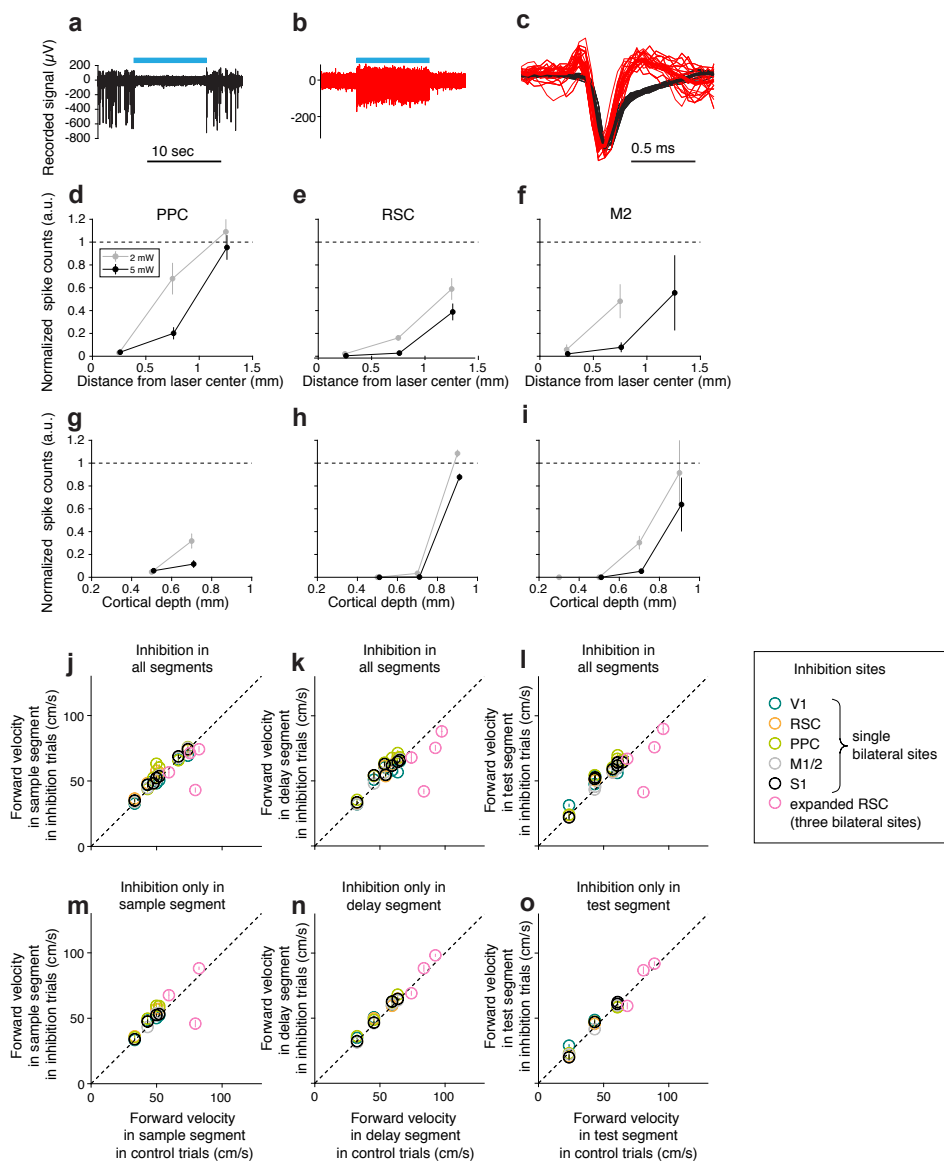
60. Stringer, C., et al. Spontaneous behaviors drive multidimensional, brainwide activity. *Science* **364**, 255 (2019).
61. Gold, J.I. & Shadlen, M.N. Neural computations that underlie decisions about sensory stimuli. *Trends in cognitive sciences* **5**, 10-16 (2001).
62. Gold, J.I. & Shadlen, M.N. The neural basis of decision making. *Annu. Rev. Neurosci.* **30**, 535-574 (2007).
63. Rigotti, M., Ben Dayan Rubin, D., Wang, X.J. & Fusi, S. Internal representation of task rules by recurrent dynamics: the importance of the diversity of neural responses. *Front. Comput. Neurosci.* **4**, 24 (2010).
64. Rigotti, M., et al. The importance of mixed selectivity in complex cognitive tasks. *Nature* **497**, 585-590 (2013).
65. Panzeri, S., Harvey, C.D., Piasini, E., Latham, P.E. & Fellin, T. Cracking the Neural Code for Sensory Perception by Combining Statistics, Intervention, and Behavior. *Neuron* **93**, 491-507 (2017).
66. Britten, K.H., Newsome, W.T., Shadlen, M.N., Celebrini, S. & Movshon, J.A. A relationship between behavioral choice and the visual responses of neurons in macaque MT. *Vis. Neurosci.* **13**, 87-100 (1996).
67. Gidon, A., et al. Dendritic action potentials and computation in human layer 2/3 cortical neurons. *Science* **367**, 83-87 (2020).
68. London, M. & Häusser, M. Dendritic computation. *Annu. Rev. Neurosci.* **28**, 503-532 (2005).
69. Shannon, C.E. A Mathematical Theory of Communication. *Bell System Technical Journal* **27**, 379-423 (1948).
70. Hanks, T.D., et al. Distinct relationships of parietal and prefrontal cortices to evidence accumulation. *Nature* **520**, 220-223 (2015).
71. Raposo, D., Kaufman, M.T. & Churchland, A.K. A category-free neural population supports evolving demands during decision-making. *Nat. Neurosci.* **17**, 1784-1792 (2014).
72. Zhou, Y. & Freedman, D.J. Posterior parietal cortex plays a causal role in perceptual and categorical decisions. *Science* **365**, 180-185 (2019).
73. Goard, M.J., Pho, G.N., Woodson, J. & Sur, M. Distinct roles of visual, parietal, and frontal motor cortices in memory-guided sensorimotor decisions. *eLife* **5** (2016).
74. Scott, B.B., et al. Fronto-parietal Cortical Circuits Encode Accumulated Evidence with a Diversity of Timescales. *Neuron* **95**, 385-398 (2017).
75. Akrami, A., Kopec, C.D., Diamond, M.E. & Brody, C.D. Posterior parietal cortex represents sensory history and mediates its effects on behaviour. *Nature* **554**, 368-372 (2018).
76. Chen, L.L., Lin, L.H., Barnes, C.A. & McNaughton, B.L. Head-direction cells in the rat posterior cortex. II. Contributions of visual and ideothetic information to the directional firing. *Exp. Brain Res.* **101**, 24-34 (1994).
77. Jacob, P.Y., et al. An independent, landmark-dominated head-direction signal in dysgranular retrosplenial cortex. *Nat. Neurosci.* **20**, 173-175 (2017).
78. Lozano, Y.R., et al. Retrosplenial and postsubiculum head direction cells compared during visual landmark discrimination. *Brain Neurosci Adv* **1**, 2398212817721859 (2017).
79. Todd, T.P., Meyer, H.C. & Bucci, D.J. Contribution of the retrosplenial cortex to temporal discrimination learning. *Hippocampus* **25**, 137-141 (2015).
80. Powell, A.L., et al. The retrosplenial cortex and object recency memory in the rat. *Eur. J. Neurosci.* **45**, 1451-1464 (2017).
81. Hattori, R., Danskin, B., Babic, Z., Mlynaryk, N. & Komiyama, T. Area-Specificity and Plasticity of History-Dependent Value Coding During Learning. *Cell* **177**, 1858-1872 (2019).
82. Hattori, R. & Komiyama, T. Context-dependent persistency as a coding mechanism for robust and widely distributed value coding. *Neuron* (2021).
83. Vogt, B.A. & Miller, M.W. Cortical connections between rat cingulate cortex and visual, motor, and postsubiculum cortices. *J. Comp. Neurol.* **216**, 192-210 (1983).
84. Van Groen, T. & Wyss, J.M. Connections of the retrosplenial granular b cortex in the rat. *J. Comp. Neurol.* **463**, 249-263 (2003).
85. van Groen, T. & Wyss, J.M. Connections of the retrosplenial granular a cortex in the rat. *J. Comp. Neurol.* **300**, 593-606 (1990).
86. Zingg, B., et al. Neural networks of the mouse neocortex. *Cell* **156**, 1096-1111 (2014).
87. Deshmukh, S.S. & Knierim, J.J. Influence of local objects on hippocampal representations: Landmark vectors and memory. *Hippocampus* **23**, 253-267 (2013).
88. Niell, C.M. & Stryker, M.P. Modulation of visual responses by behavioral state in mouse visual cortex. *Neuron* **65**, 472-479 (2010).
89. Velez-Fort, M., et al. A Circuit for Integration of Head- and Visual-Motion Signals in Layer 6 of Mouse Primary Visual Cortex. *Neuron* **98**, 179-191 e176 (2018).

90. Poort, J., et al. Learning Enhances Sensory and Multiple Non-sensory Representations in Primary Visual Cortex. *Neuron* **86**, 1478-1490 (2015).
91. Johnston, W.J., Palmer, S.E. & Freedman, D.J. Nonlinear mixed selectivity supports reliable neural computation. *PLoS Comput. Biol.* **16**, e1007544 (2020).
92. Asaad, W.F., Rainer, G. & Miller, E.K. Neural activity in the primate prefrontal cortex during associative learning. *Neuron* **21**, 1399-1407 (1998).
93. Ranganathan, G.N., et al. Active dendritic integration and mixed neocortical network representations during an adaptive sensing behavior. *Nat. Neurosci.* **21**, 1583-1590 (2018).
94. Peron, S., et al. Recurrent interactions in local cortical circuits. *Nature* **579**, 256-259 (2020).
95. Mardinly, A.R., et al. Precise multimodal optical control of neural ensemble activity. *Nat. Neurosci.* **21**, 881-893 (2018).
96. Marshel, J.H., et al. Cortical layer-specific critical dynamics triggering perception. *Science* **365** (2019).
97. Carrillo-Reid, L., Han, S., Yang, W., Akrouh, A. & Yuste, R. Controlling Visually Guided Behavior by Holographic Recalling of Cortical Ensembles. *Cell* **178**, 447-457 (2019).
98. Zhang, Z., Russell, L.E., Packer, A.M., Gauld, O.M. & Hausser, M. Closed-loop all-optical interrogation of neural circuits in vivo. *Nat Methods* **15**, 1037-1040 (2018).
99. Daie, K., Svoboda, K. & Druckmann, S. Targeted photostimulation uncovers circuit motifs supporting short-term memory. *Nat. Neurosci.* **24**, 259-265 (2021).
100. Aronov, D. & Tank, D.W. Engagement of neural circuits underlying 2D spatial navigation in a rodent virtual reality system. *Neuron* **84**, 442-456 (2014).
101. Wald, A. *Sequential Analysis* (Wiley, 1947).
102. Wald, A. & Wolfowitz, J. Optimum Character of the Sequential Probability Ratio Test. *The Annals of Mathematical Statistics* **19**, 326-339 (1948).
103. Ratzlaff, E.H. & Grinvald, A. A tandem-lens epifluorescence macroscope: hundred-fold brightness advantage for wide-field imaging. *J. Neurosci. Methods* **36**, 127-137 (1991).
104. Marshel, J.H., Garrett, M.E., Nauhaus, I. & Callaway, E.M. Functional specialization of seven mouse visual cortical areas. *Neuron* **72**, 1040-1054 (2011).
105. Kalatsky, V.A. & Stryker, M.P. New paradigm for optical imaging: temporally encoded maps of intrinsic signal. *Neuron* **38**, 529-545 (2003).
106. Sereno, M.I., McDonald, C.T. & Allman, J.M. Analysis of retinotopic maps in extrastriate cortex. *Cereb. Cortex* **4**, 601-620 (1994).
107. Zhuang, J., et al. An extended retinotopic map of mouse cortex. *eLife* **6** (2017).
108. Guizar-Sicairos, M., Thurman, S.T. & Fienup, J.R. Efficient subpixel image registration algorithms. *Opt Lett* **33**, 156-158 (2008).
109. Greenberg, D.S. & Kerr, J.N. Automated correction of fast motion artifacts for two-photon imaging of awake animals. *J. Neurosci. Methods* **176**, 1-15 (2009).
110. Pachitariu, M., et al. Suite2p: beyond 10,000 neurons with standard two-photon microscopy. *bioRxiv*, 061507 (2017).
111. Friedrich, J., Zhou, P. & Paninski, L. Fast online deconvolution of calcium imaging data. *PLoS Comput. Biol.* **13**, e1005423 (2017).
112. Pillow, J.W., et al. Spatio-temporal correlations and visual signalling in a complete neuronal population. *Nature* **454**, 995-999 (2008).
113. Truccolo, W., Eden, U.T., Fellows, M.R., Donoghue, J.P. & Brown, E.N. A point process framework for relating neural spiking activity to spiking history, neural ensemble, and extrinsic covariate effects. *J. Neurophysiol.* **93**, 1074-1089 (2005).
114. Friedman, J., Hastie, T. & Tibshirani, R. Regularization Paths for Generalized Linear Models via Coordinate Descent. *J Stat Softw* **33**, 1-22 (2010).
115. Gold, J.I. & Shadlen, M.N. Banburismus and the brain: decoding the relationship between sensory stimuli, decisions, and reward. *Neuron* **36**, 299-308 (2002).
116. Wilber, A.A., Skelin, I., Wu, W. & McNaughton, B.L. Laminar Organization of Encoding and Memory Reactivation in the Parietal Cortex. *Neuron* **95**, 1406-1419 (2017).
117. Devroye, L. *Non-Uniform Random Variate Generation* (Springer New York, 2013).



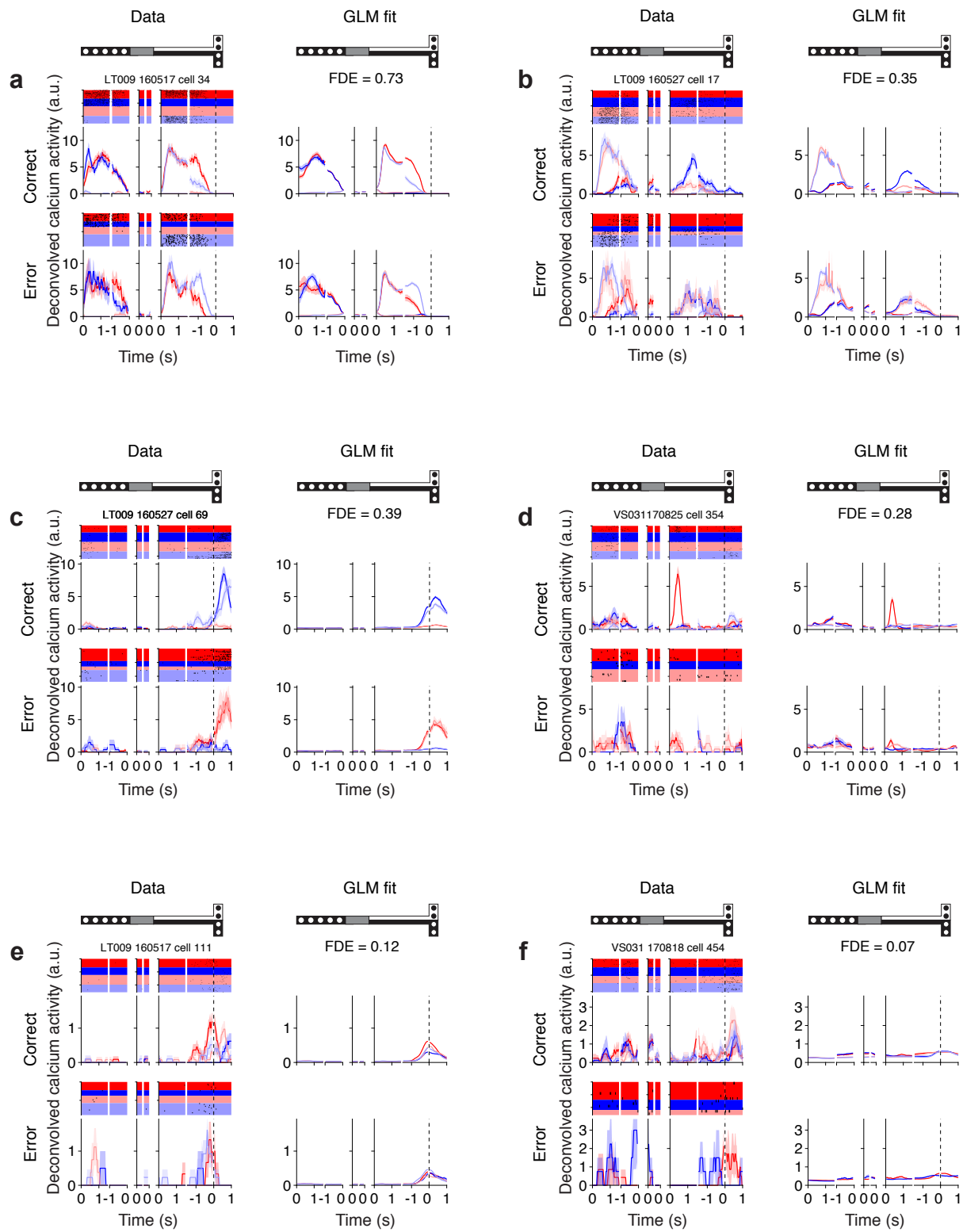
Supplementary Fig. 1 | Behavioral performance of mice used for calcium imaging experiments

- An example session with high task performance. The raster plot shows trial types (first row) and the correctness of choice (second row). The width of rectangles and gaps between them indicate the length of trials and the inter-trial intervals, respectively. The running mean of task performance and pace were calculated in the preceding 20 trials, excluding crutch trials (see Methods). See marker legend in panel (g).
- Mean trial completion time for correct and error trials during the session in (a). Error bars indicate mean \pm s.d. across trials. n = 179 correct / 16 error trials.
- Similar to panel (a), except for an example session with moderate task performance.
- Similar to panel (b), except for the session in (c). n = 163 correct / 44 error trials.
- Task performance and pace averaged across sessions. The solid and dashed lines indicate mean \pm s.d. n = 63 sessions from 6 mice.
- Mean trial completion time for correct and error trials averaged across all sessions. Error bars indicate mean \pm s.d. across sessions.
- Marker legend for panels (a-f).
- Choice bias for the color (choosing black vs white), direction (choosing right or left), and direction conditioned on the same sample cue (see Eq. 1-3 in Methods). Open circles show bias in individual sessions. Filled circles with error bars indicate median \pm median absolute deviation. Filled triangles and diamonds indicate biases in the example sessions in panels (a-b) and (c-d), respectively. n = 63 sessions from 6 mice.
- Choice (final turn direction) decoded from the mouse's running velocity in the test segment. Thin gray lines indicate individual sessions. Thick black line and shading indicates mean \pm s.e.m. n = 63 sessions from 6 mice.
- Similar to (i), plotted separately for correct and error trials. Shading indicates mean \pm s.e.m.
- Task performance across sessions (dots) and mice (panels) compared to the decoding of the sample cue from the mouse's running velocity at the end of the delay segment. Two mice were excluded due to small numbers of sessions (less than five sessions). r_s indicates the Spearman rank correlation coefficient.



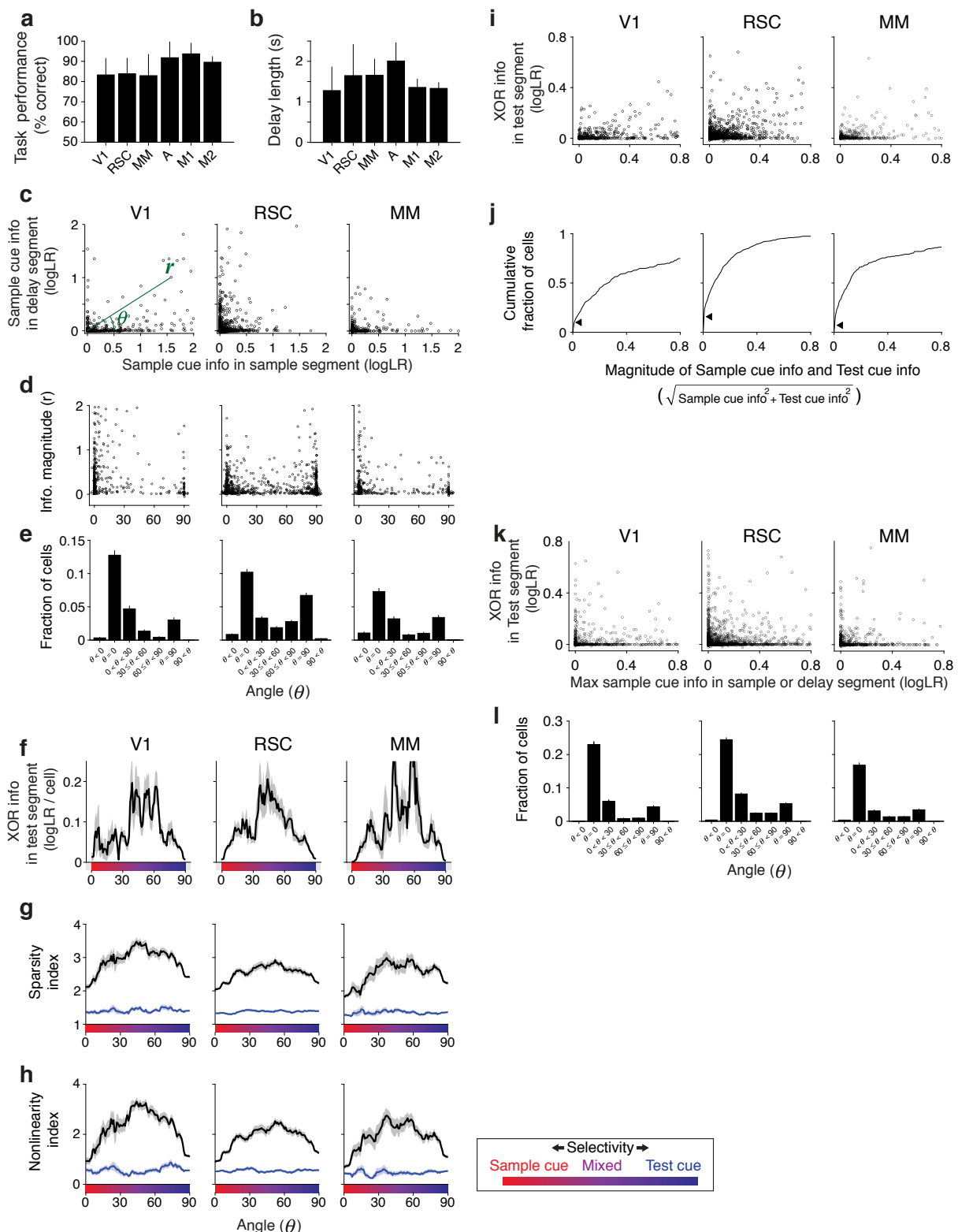
Supplementary Fig. 2 | Photo-inhibition effects on spiking activity and the mouse's running

- Electrophysiology trace from a putative excitatory cell in PPC of a VGAT-ChR2 mouse. Blue line indicates the photoinhibition (laser on).
- Similar to panel (a), except for a putative inhibitory cell.
- Spike waveforms for the example units shown in panels (a-b). The amplitudes were normalized to compare the spike width of a putative excitatory cell (black) and inhibitory cell (red). Thin lines indicate individual spikes. Thick lines indicate mean waveforms.
- Normalized spike counts (first five seconds from laser onset) as a function of horizontal distance from the laser center during photoinhibition in PPC. Spike counts were normalized to the period just before laser onset. Error bars indicate mean \pm s.e.m. across trials. $n = 11.8 \pm 6.2$ trials (mean \pm s.d.) per data point from one mouse.
- Similar to panel (d) except for RSC.
- Similar to panel (d) except for M2.
- Normalized spike counts as a function of cortical depth in PPC. Spikes were recorded within 500 μm horizontal distance from the laser center. $n = 13.6 \pm 11.2$ trials (mean \pm s.d.) per data point from one mouse.
- Similar to panel (g) except for RSC.
- Similar to panel (g) except for M2.
- Comparison of the mouse's forward running velocity in the sample segment on control trials and trials with inhibition in all segments. Each open circle indicates the average forward velocity of a single mouse on trials with a bilateral pair of inhibition sites (or three bilateral pairs of inhibition sites for the RSC expanded inhibition) and the average forward velocity on control trials. Data from each mouse are plotted vertically at the control-trial velocity unique to that mouse. Inhibition sites are grouped for different areas as shown in Figure 1l. Error bars within open circles indicate mean \pm s.e.m. across trials. $n = 39$ inhibition groups from 11 mice for panels (j-l)
- Similar to panel (j) except for the forward velocity in the delay segment.
- Similar to panel (j) except for the forward velocity in the test segment.
- Similar to panel (j) except for the forward velocity in trials with inhibition only in the sample segment. $n = 23$ inhibition groups from 7 mice for panels (m-o).
- Similar to panel (k) except for the forward velocity in trials with inhibition only in the delay segment.
- Similar to panel (k) except for the forward velocity in trials with inhibition only in the test segment.



Supplementary Fig. 3 | GLM with various levels of explanatory power for example cells

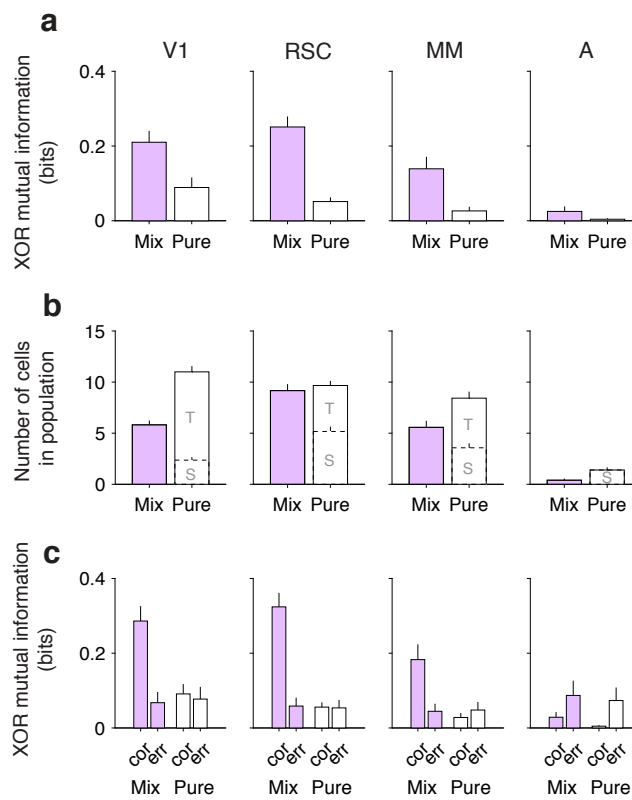
- (a) Observed neural activity and GLM fit for an example V1 cell. Left panels: observed neural activity plotted similarly to Figure 2e-j. Right panels: regularized GLM fits to the training data. Shading indicates mean \pm s.e.m. The predictive power of the model was quantified by the fraction of deviance explained (FDE) indicated at the top.
- (b) Similar to panel (a) for an example MM cell.
- (c) Similar to panel (a) for an example MM cell in Figure 2g.
- (d) Similar to panel (a) for an example RSC cell in Figure 2i.
- (e) Similar to panel (a) for an example V1 cell with low activity and selectivity.
- (f) Similar to panel (a) for an example RSC cell with low activity and selectivity.



Supplementary Fig. 4 | Task-related information and its mixing in V1, RSC and MM

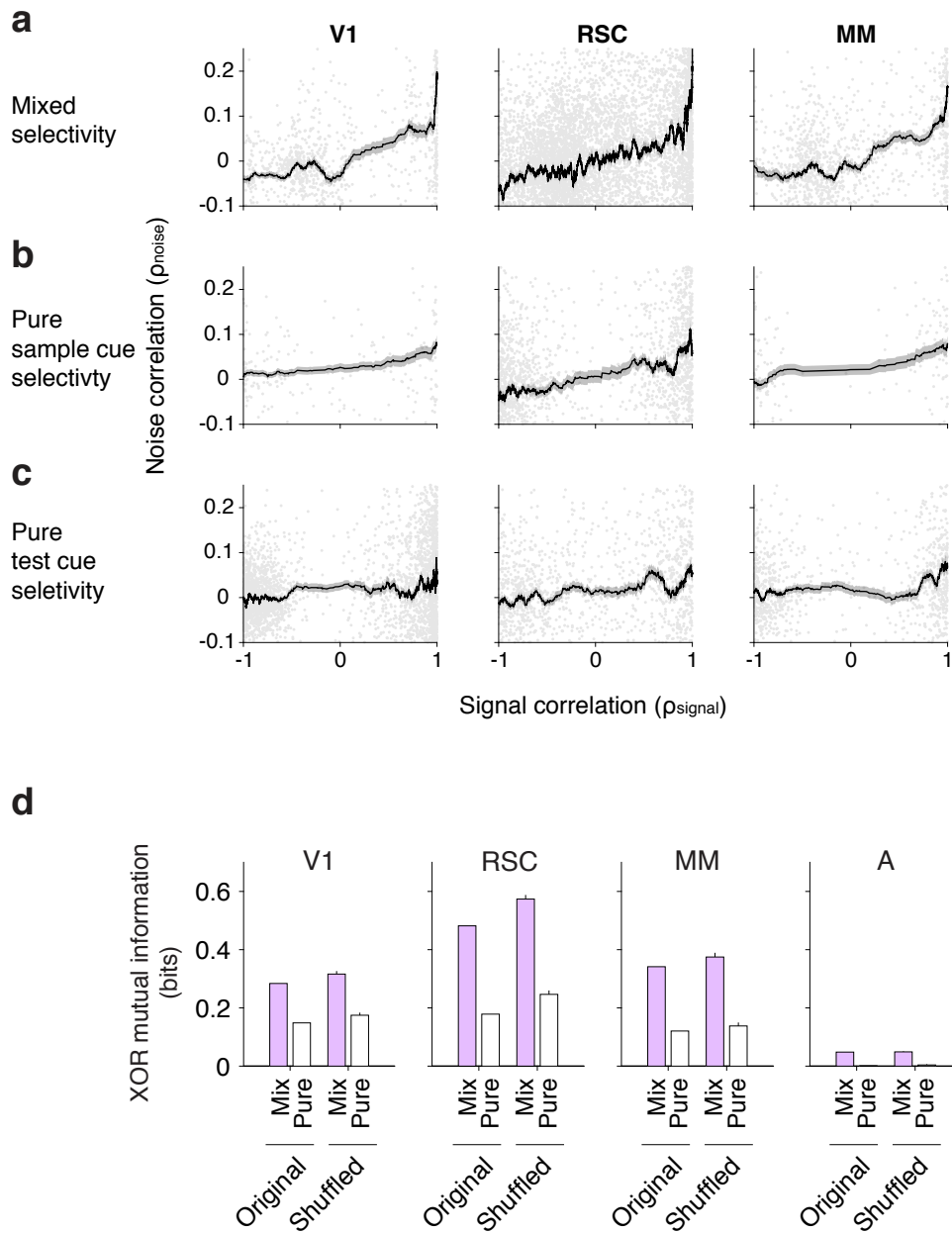
- (a) Task performance averaged across imaging sessions for each area. Error bars indicate mean \pm s.d. V1: n = 11 sessions, RSC: n = 12 sessions, MM: n = 7 sessions, A: n = 5 sessions, M1: n = 3 sessions, M2: n = 9 sessions were included in panels (a-b). Average task performance was not significantly different between two areas except for M1 and V1 ($p = 0.0018$) and M1 and RSC ($p = 0.0011$). The significance threshold was adjusted by Bonferroni correction with $\alpha = 0.05$ to account for 15 between-area comparisons for panels (a-b).
- (b) Delay length averaged across imaging sessions for each area. Error bars indicate mean \pm s.d. Average task performance was not significantly different between two areas except for A and V1 ($p = 0.0010$), A and M1 ($p = 0.0001$), and A and M2 ($p < 10^{-4}$).
- (c) Sample cue information in the sample segment and delay segment for individual cells (dots). Cells along the horizontal axis (0 degrees) had sample cue information only in the sample segment, and cells along the vertical axis (90 degrees) had sample cue information only in the delay segment.
- (d) Data from panel (c) replotted in polar coordinates as the magnitude (r) and angle (θ). The absence of many cells around 45 degrees indicates that few cells had sample cue information in both the sample and delay segments. Rather, different populations of neurons, especially in RSC, appeared to contain sample cue information in the different segments.

- (e) Distribution of cells from panel (d). Bins for $\theta = 0$ and $\theta = 90$ include cells with chance-level deviation from the axes (Methods). Error bars indicate mean \pm s.e.m. The fractions of cells with noise-level information (magnitude $r < 0.01$) are not shown.
- (f) XOR information for cells across angles (running average, window of 50 cells), shown separately for V1, RSC, and MM. Shading indicates mean \pm s.e.m.
- (g) Sparsity index for cells across angles (running average, window of 50 cells), shown separately for V1, RSC, and MM as black traces. Blue traces show chance sparsity index values computed with shuffled trial identities. Shading indicates mean \pm s.e.m.
- (h) Similar to panel (g), except for the nonlinearity index.
- (i) XOR information versus the magnitude of the sample cue and test cue information in the first one second of the test segment for individual cells (circles). Only correct trials were included in the analysis. Cells with pure XOR selectivity have high XOR information but zero sample cue information and zero test cue information. For correct trials, a pure XOR selective cell or a pure choice selective cells might be active on both W/WB and B/BW trial types. Such a cell is thus active on trials with both sample cues and both test cues and thus lacks sample cue and test cue information.
- (j) Cumulative fraction of cells as a function of the magnitude of a cell's sample cue and test cue information. Pure XOR selective cells were defined to have XOR information greater than logLR of 0.01 and the magnitude of sample cue and test cue information less than the chance level (logLR of 0.017 in V1, 0.007 in RSC, 0.005 in MM, see Methods). Cells were excluded from the analysis if they had XOR information less than logLR of 0.01. The fraction of pure XOR selective cells was $7.7 \pm 1.6\%$ in V1, $16.0 \pm 1.1\%$ in RSC, and $13.2 \pm 1.8\%$ in MM (mean \pm s.e.m.).
- (k) Similar to panel (c), except for XOR information in the first one second of the test segment versus the maximum sample cue information in the sample or test segment. Cells in the first quadrant ($0^\circ < \theta < 90^\circ$) or on the vertical axis (90°) had XOR information in the test segment with or without having sample cue information in the sample or delay segment.
- (l) Similar to panel (e), except for summarizing the data in panel (k).



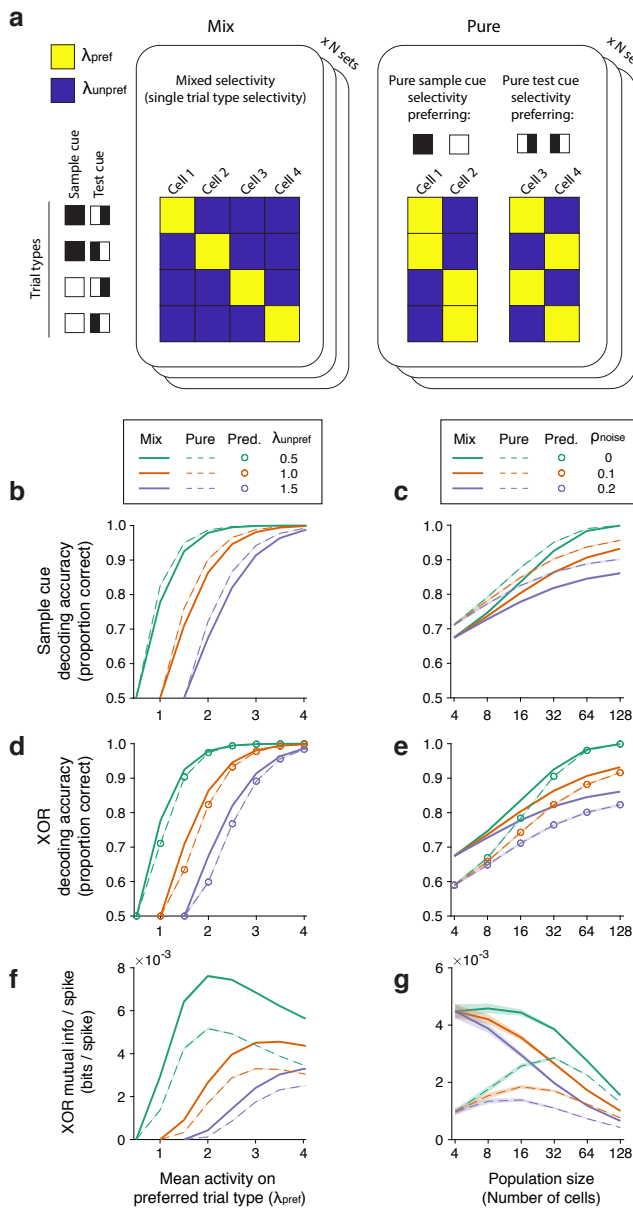
Supplementary Fig. 5 | XOR information in populations of mixed selectivity or pure selectivity cells, controlling for the population size

- Similar to Fig. 5b, except for a population size of 100 cells. Mutual information between true and decoded XOR in populations of mixed selectivity cells ($15^\circ < \theta < 75^\circ$ in Fig. 4h, correct trials) and pure selectivity cells ($\theta = 0^\circ$ and $\theta = 90^\circ$ in Fig. 4i, correct trials) is shown. From the entire population imaged during each session, 100 cells were randomly sampled without replacement. The analyses included sessions with more than 100 detected cells. V1: n = 8 sessions (1783 trials), RSC: n = 12 sessions (1685 trials), MM: n = 7 sessions (1230 trials), A: n = 5 sessions (822 trials). Error bars indicate mean \pm s.e.m. across trials. Mutual information in mixed selectivity cells was significantly greater than that in pure selectivity cells in V1 ($p=0.0022$), RSC ($p < 10^{-4}$), MM ($p=0.0002$), but not in A ($p = 0.10$).
- Similar to Fig. 5c, except for a population size of 100 cells. Number of cells classified as mixed selective or pure selective (T = test cue selective; S = sample cue selective) per session is shown. Error bars indicate mean \pm s.e.m. The number of cells was significantly larger for pure selective cells than for mixed selective cells across areas in V1 ($p < 10^{-4}$), MM ($p = 0.023$), and A ($p = 0.027$), but not in RSC ($p = 0.93$).
- Similar to Fig. 5d, except for a population of 100 cells. Mutual information between true and decoded XOR on correct and error trials is shown. Error bars indicate mean \pm s.e.m. V1: n = 1062 correct / 272 error trials, RSC: n = 1420 correct / 265 error trials, MM: n = 1009 correct / 221 error trials, A: n = 753 correct / 69 error trials. For mixed selectivity cell population, the difference between correct and error was significantly different from zero in all four areas (V1: $p < 10^{-4}$, RSC: $p < 10^{-4}$, MM: $p = 0.0008$, A = 0.028). For pure selectivity cell population, the difference between correct and error was significantly different from zero in A ($p = 0.028$), but not in V1 ($p = 0.60$), RSC ($p = 0.87$), and MM ($p = 0.35$). The difference between correct and error in mixed selective cells was significantly larger than that for pure selective cells in V1 ($p < 10^{-4}$), RSC ($p < 10^{-4}$), and MM ($p=0.0010$), but not in A ($p = 0.82$). The difference between correct and error in mixed selective cells was significantly larger in RSC than in MM ($p = 0.021$) or A ($p < 10^{-4}$), but the difference was not significant between RSC and V1 ($p = 0.22$).



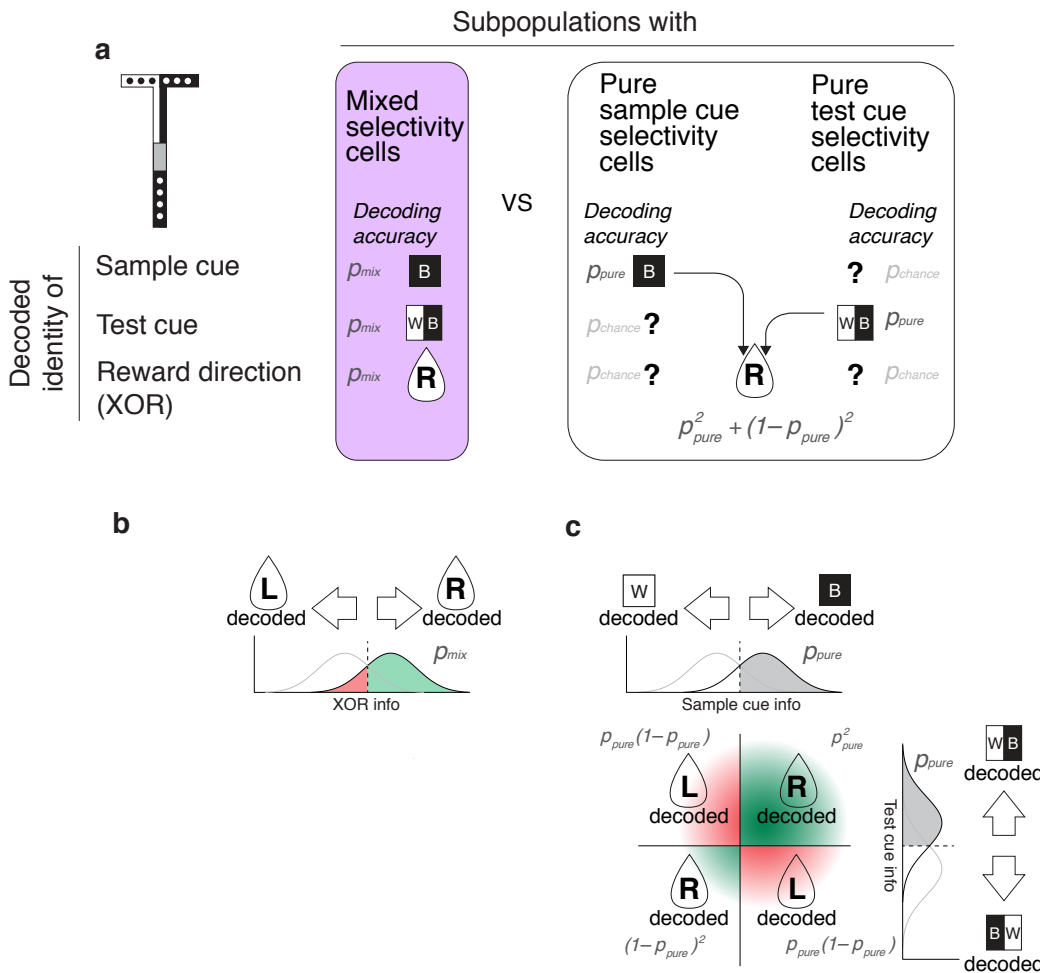
Supplementary Fig. 6 | Noise correlations in populations of mixed selectivity or pure selectivity cells

- (a) Signal and noise correlations in neural activity of mixed selectivity cells ($15^\circ < \theta < 75^\circ$ in Fig. 4h, correct trials) at the beginning of the test segment (first 1 s). Gray dots show Pearson's correlation coefficients for signal (mean activity for each of four trial type) and noise (residual activity around the mean). Black traces show the running mean \pm s.e.m. (window size = 100 pairs). n = 1020 pairs in V1, 6807 pairs in RSC, 1177 pairs in MM.
- (b) Similar to panel (a), except with pure sample cue selective cells ($\theta = 0^\circ$ in Fig. 4i, correct trials). n = 202 pairs in V1, 1797 pairs in RSC, 182 pairs in MM.
- (c) Similar to panel (a), except with pure test cue selective cells ($\theta = 90^\circ$ in Fig. 4i, correct trials). n = 3362 pairs in V1, 1334 pairs in RSC, 958 pairs in MM.
- (d) Decoding accuracy of XOR in the original data and data shuffled to disrupt noise correlations. Noise correlations were disrupted by shuffling trial identity within each trial type for each cell. Error bars indicate mean \pm s.e.m. The difference in decoding accuracy between the mixed selectivity and pure selectivity population was not significantly different between the original data and trial-shuffled data in all four areas (V1: p = 0.66, RSC: p = 0.22, MM: p = 0.40, A: p = 0.43).



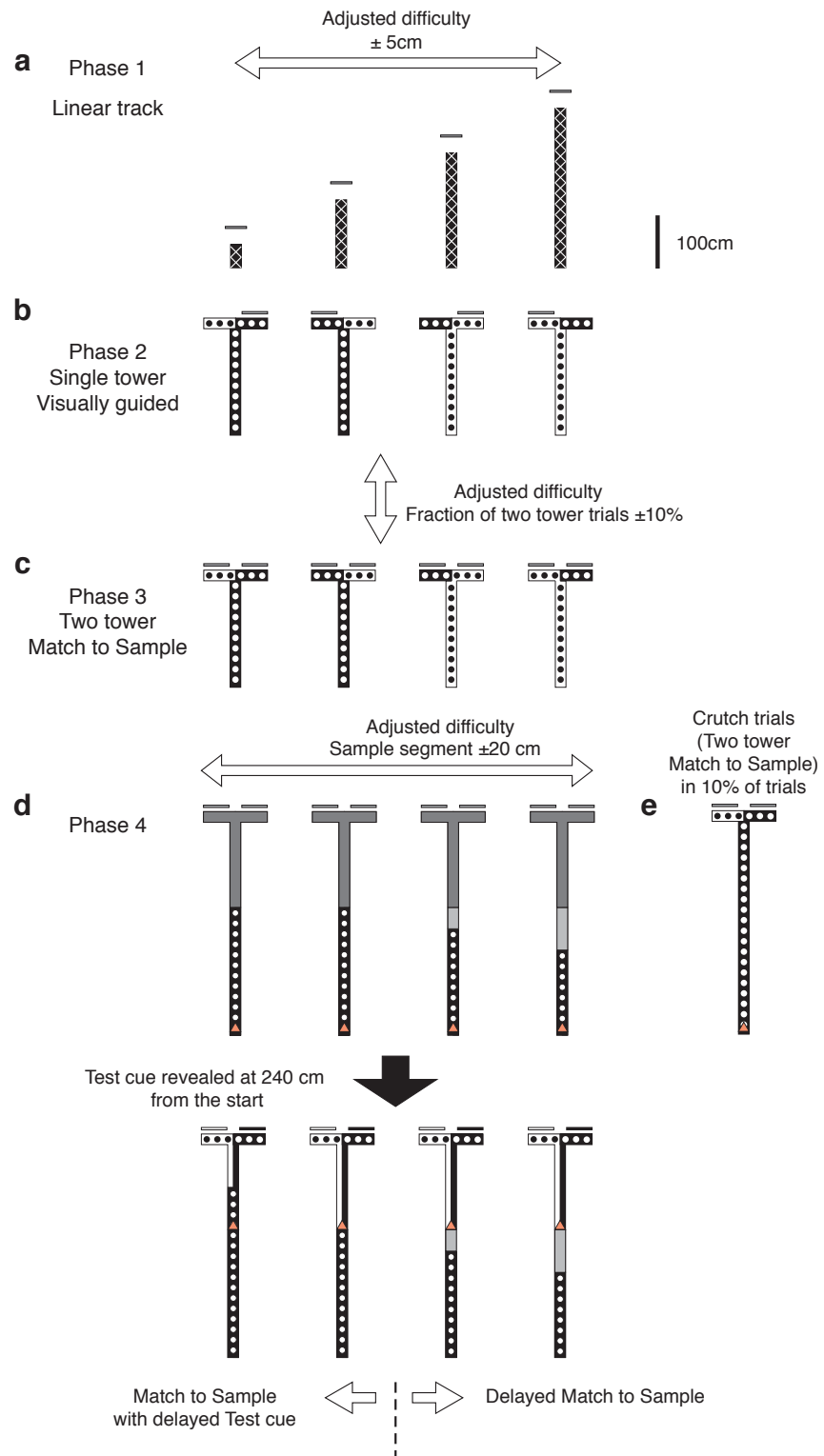
Supplementary Fig. 7 | Decoding accuracy from simulated mixed and pure selectivity populations

- (a) Schematic of simulated population. The number of spikes generated by each cell follows a Poisson distribution with the mean λ . Each cell responds to a preferred cue (or a preferred combination of cues) with the mean of λ_{pref} and to an unpreferred cue with the mean of λ_{unpref} . The minimum unit population size is a set of four cells, each of which preferentially responds to a specific trial type in the mixed selectivity population, or to a specific sample cue or test cue identity in the pure selectivity population. The population size increases by including N sets of the unit population with the same selectivity pattern.
- (b) Decoding accuracy for the sample cue (or test cue) in simulated population activity under a various combination of the mean activity (λ_{pref} and λ_{unpref}). The SNR in the population increases with higher λ_{pref} and lower λ_{unpref} under Poisson noise. The population activity was simulated on 10,000 trials and repeated 10,000 times, separately in mixed selectivity population (solid lines) and pure selectivity population (dashed lines). Shading indicates mean \pm s.e.m. and is equal or smaller than the line widths.
- (c) Similar to panel (b), but under various combinations of the population size and noise correlation magnitudes. The SNR in the population increases with a larger population size and lower noise correlation.
- (d) Similar to panel (b), but with the decoding accuracy for the reward direction (XOR). For a pure selectivity population, the decoding accuracy of XOR (p_{XOR} , dashed line in panels d, e) can be predicted by decoding accuracy for the sample cue (or test cue) (p , dashed line in panels b, c). Open circles show \hat{p}_{XOR} predicted by $p^2 + (1-p)^2$: the sum of probabilities that both sample and test cues decoded correctly (p^2) or incorrectly ($(1-p)^2$). See Supplementary Fig. 8 for reasoning.
- (e) Similar to panel (c), but with the decoding accuracy for the reward direction (XOR).
- (f) Similar to panel (b), but with XOR mutual information divided by the total number of expected spikes in a population.
- (g) Similar to panel (c), but with XOR mutual information divided by the total number of expected spikes in a population.



Supplementary Fig. 8 | Mathematical interpretation of the decoding accuracy from simulated mixed and pure selectivity populations

- Decoding accuracy for each task-related variable in mixed vs pure selectivity populations, shown similarly to Figure 5a.
- For a population of mixed selectivity cells, XOR can be linearly decoded by a single decision. The decoding accuracy is equal for each task-related variable (p_{mix}) because each cell is equally informative for the sample cue, test cue, and reward direction (Supplementary Fig. 7a).
- For a population of pure selective cells, XOR can be decoded by dual decisions about the sample cue and test cue, as illustrated by the two decision boundaries for the sample cue and test cue (dashed lines). When the sample cue information and test cue information are plotted together in a 2D space, these two boundaries form nonlinear decision boundaries that separate right vs left (green vs red) decoding for the reward direction (XOR). When the decoding accuracy is equal for the sample cue or the test cue (p_{pure}), the decoding accuracy of XOR is given by $p_{pure}^2 + (1-p_{pure})^2$, the sum of probability that both cues are decoded correctly, p_{pure} , or incorrectly, $(1-p_{pure})^2$ (due to the task design). The decoding accuracy for XOR is thus lower than that for the sample cue or test cue. See also Supplementary Figure 7.



Supplementary Fig. 9 | Virtual reality maze for behavioral training

- Linear track in Phase 1. The maze was lengthened based on the behavioral performance (Methods).
- Single-tower maze in Phase 2. The T-stem was either black or white and T-arms were BW or WB, resembling the sample cue and test cue, respectively. The rewarded turn direction was determined by the combination of the T-stem color and T-arm color, but also indicated by the location of a single tower.
- Two-tower maze in Phase 3. The rewarded turn direction was determined by the combination of the T-stem color and T-arm color. Two-tower trials were interleaved with single-tower trials. The fraction of single-tower trials varied based on the behavioral performance (Methods).
- Delayed match-to-sample maze. Red triangle indicates the mouse position in the maze. The test cue configuration, BW or WB, was revealed when the mouse reached a point 240 cm away from the maze start.
- Two-tower maze used in “crutch trials”, which are randomly selected 10% of trials in Phase 4 to aid the performance of mice. The maze structure was similar to (c), except for the longer T-stem.